P-13-44

Äspö Task Force on modelling of groundwater flow and transport of solutes

Task 7 – Reduction of performance assessment uncertainty through modelling of hydraulic tests at Olkiluoto

René Therrien, Daniela Blessent

Department of Geology and Geological Engineering,
Université Laval

January 2017

Svensk Kärnbränslehantering AB
Swedish Nuclear Fuel
and Waste Management Co

Box 250, SE-101 24 Stockholm
Phone +46 8 459 84 00

ISSN 1651-4416
SKB P-13-44
ID 1413232

January 2017

Äspö Task Force on modelling of groundwater flow and transport of solutes

Task 7 – Reduction of performance assessment uncertainty through modelling of hydraulic tests at Olkiluoto

René Therrien, Daniela Blessent

Department of Geology and Geological Engineering,

Université Laval

This report concerns a study which was conducted for Svensk Kärnbränslehantering AB (SKB). The conclusions and viewpoints presented in the report are those of the authors. SKB may draw modified conclusions, based on additional literature sources and/or expert opinions.

Data in SKB's database can be changed for different reasons. Minor changes in SKB's database will not necessarily result in a revised report. Data revisions may also be presented as supplements, available at www.skb.se.

Abstract

This report presents results from numerical simulations related to the Task 7 on reduction of performance assessment uncertainty through modelling of hydraulic tests at Olkiluoto, Finland. Simulation were conducted by a modelling team from Universite Laval within the framework of the Äspö Task Force. Task 7 was divided in three separate subtasks, 7A, 7B and 7C, which addressed different spatial scales for hydraulic testing at Olkiluoto.

A 3D discrete fracture network model was developed within subtask 7A to simulate a long-term pumping test at Olkiluoto. The model was developed at the scale of the Olkiluoto Island and the main hydraulic zones were represented as two-dimensional features. The hydraulic conductivity of the main hydraulic zones was modified to reproduce observed drawdown but not flow measurements made with the Posiva Flow Log (PFL). A series of simulations show that long open boreholes connect hydraulic zones, which increases the bulk hydraulic conductivity of the rock mass and decreases hydraulic head gradients in the system.

Subtask 7B focused on hydraulic tests in a block of crystalline bedrock of about 0.03 km^3 that contains low-transmissivity fractures. Fracture density, orientation, and fracture transmissivity are estimated from Posiva Flow Log (PFL) measurements in boreholes drilled in the rock block. On the basis of those data, a geostatistical approach relying on a transitional probability and Markov chain models is used to define a conceptual model based on stochastic fractured rock facies. Four facies are defined, from sparsely fractured bedrock to highly fractured bedrock. Using this conceptual model, three-dimensional groundwater flow is then simulated to reproduce interference pumping tests in either open or packed-off boreholes. Hydraulic conductivities of the fracture facies are estimated through automatic calibration using either hydraulic heads or both hydraulic heads and PFL flow rates as targets for calibration. The latter option produces a narrower confidence interval for the calibrated hydraulic conductivities, therefore reducing the associated uncertainty and demonstrating the usefulness of the measured PFL flow rates.

Subtask 7C focused on groundwater flow in low-transmissivity fractures identified during construction of the three ventilation shafts of the ONKALO underground research laboratory. The goal of subtask 7C was to develop a near-field single-fracture scale model incorporating micro-structural information. A 3D discrete fracture model was developed to represent a single fracture that intersected the three shafts. Contrary to the previous subtasks, a spatially-variable aperture was generated for the fracture. The measured flow into and out of the fracture could not all be reproduced equally well by the model. Simulations show that local apertures greatly influence flow velocity and direction in the fracture.

Sammanfattning

Denna rapport presenterar resultat från numeriska simuleringar i samband med Task 7 som rör minskning av osäkerheter vid bedömning av förvarsfunktioner genom modellering av hydrauliska tester i Olkiluoto, Finland. Simuleringarna utfördes av ett forskningsteam från Université Laval inom ramen för Äspö Task Force. Modelleringsuppgift 7 delades i tre separata deluppgifter, 7A, 7B och 7C, som inriktar sig på olika rumsliga skalor för de hydrauliska testerna som utfördes på Olkiluoto.

En 3D diskret spricknätverksmodell har utvecklats inom deluppgift 7A för att simulera ett långsiktigt pumptestet på Olkiluoto. Modellen omfattar hela ön Olkiluoto och inkluderar de viktigaste hydrauliska zonerna som representeras av tvådimensionella strukturer. Den hydrauliska konduktiviteten för de viktigaste hydrauliska zonerna modifierades för att kunna reproducera observerade avsänkningar. Kalibreringen gjordes inte med avseende på flödesmätningar som gjorts med Posiva Flow Log (PFL). En serie simuleringar visar att långa öppna borrhål kan koppla ihop hydrauliska zoner, vilket ökar bulkvärdet för den hydrauliska konduktiviteten av bergmassan samt minskar hydrauliska huvudgradienter i systemet.

Deluppgift 7B fokuserade på hydrauliska tester i ett block av urberg på cirka 0,03 km^3 som innehåller lågtransmissiva sprickor. Sprickdensitet, orientering, och spricktransmissivitet beräknades från mätningar med Posiva Flow Log (PFL) i borrhål i bergblocket. På grundval av dessa uppgifter, togs ett geostatistisk tillvägagångssätt fram, som baseras på en övergångssannolikhet samt en Markovkedja. Metoden används för att definiera en konceptuell modell baserad på stokastiska sprickiga ”bergfacies”. Fyra ”facies” definierades, från glest sprucket berggrund till mycket uppsprucken berggrund. Med hjälp av denna begreppsmodell, simulerades sedan tredimensionellt grundvattenflöde för att kunna återge störningar pumptester i antingen öppna eller avpackade borrhål. Hydrauliska konduktiviteter av ”sprick-facies” uppskattades genom automatisk kalibrering med antingen hydrauliskt tryck eller både hydrauliskt tryck och PFL-flöden som mål för kalibreringen. Det senare alternativet ger ett smalare konfidensintervall för de kalibrerade hydrauliska konduktiviteterna, vilket minskar osäkerheten i analysen samt demonstrera nyttan av de uppmätta PFL-flödeshastigheter.

Deluppgift 7C fokuserade på grundvattenflöden i lågtransmissiva sprickor som identifierats under byggandet av tre ventilationsschakt i ONKALO (underjordiskt forskningslaboratorium). Målet i deluppgift 7C var att utveckla en närfältsmodell, i en skala relevant för en enskild spricka, som innefattar mikrostrukturinformation. En 3D diskret sprickmodell har utvecklats för att representera en enskild spricka som skär de tre axlarna. I motsats till de tidigare deluppgifterna genereras en spatialt varierande apertur för sprickan. De uppmätta flödena in i och ut ur sprickan kunde inte alla reproduceras lika väl av modellen. Simuleringarna visar att de lokala aperturerna påverkar i hög grad hastighet och riktning på vattenflödet i sprickan.

Contents

1 Introduction and objectives

The Äspö Modelling Task Force has been established to foster international collaboration and share expertise for numerical modelling of fluid flow and solute transport in the context of disposal of used nuclear fuel in geological formations. Six modelling tasks (Tasks 1 to 6) have already been completed. The Swedish company SKB (Svensk Kärnbränslehantering AB) is hosting the secretariat for the Task Force and agencies and companies from several countries have participated in the various modelling tasks to date. The agencies all have delegates to represent them at Task Force meetings, as well as modelling teams that work on the various tasks. The Nuclear Waste Management Organization (NWMO) is a member of the Task Force and has sponsored the work presented here, which has been conducted by its modelling team at the Department of Geology and Geological Engineering of Laval University, Quebec, Canada.

In 2005, the Task Force initiated Task 7 (T7) that focused on the underground research facility ONKALO at the Olkiluoto site in Finland. The site contains several open boreholes that are used for very detailed flow logging with the Posiva Flow Logging system (PFL). Task 7 initially focused on a long-term pumping test carried out in the spring of 2004 in borehole KR24, which was the planned location of the facility's ventilation shaft. The initial objective of Task 7 was to simulate the KR24 pumping test to determine how site characterisation (SC) and performance assessment (PA) can be linked, in particular by considering long-term pumping tests and measurements from borehole flow logging. Another initial objective of Task 7 was to better understand the effects of open boreholes on the groundwater system and to define how flow data from open boreholes could help site characterisation and performance assessment.

Task 7 was expanded from its initial definition into subtasks 7A, 7B and 7C (Vidstrand et al. 2015). Task 7A corresponds to the initial task definition and concerned the large-scale pumping test conducted at KR24. Task 7B focused on smaller-scale groundwater flow, at the rock block scale, by considering a series of hydraulic tests performed in a cluster of boreholes (KR14 to KR18 boreholes). Task 7C focused on fluid flow at the scale of a single fracture, which was identified during construction of 3 different shafts at the ONKALO.

This report describes the work done within Task 7. The report is divided into separate chapters that cover Tasks 7A, 7B and 7C separately. A discussion of the main findings and conclusions related to each task is presented at the end of those chapters. The final chapter summarize the main conclusions of the 3 tasks and also provide general comments on the overall Task 7 work.

In addition to this report, work related to Task 7 has also been presented in the following reports and journal papers :

Blessent D, Therrien R, Lemieux J-M, 2011. Inverse modeling of hydraulic tests in fractured crystalline rock based on a transition probability geostatistical approach. Water Resourrces Research 47, W12530. doi:10.1029/2011WR011037

Blessent D, Therrien R, Gable C W, 2011. Large-scale numerical simulation of groundwater flow and solute transport in discretely-fractured crystalline bedrock. Advances in Water Resources 34, 1539–1552.

Blessent D, Therrien R, MacQuarrie K, 2009. Coupling geological and numerical models to simulate groundwater flow and mass transport in fractured media. Computers & Geosciences 35, 1897–1906.

Graf T, Therrien R, 2008. A method to discretize non-planar fractures for 3D subsurface flow and transport simulations. International Journal for Numerical Methods in Fluids 56, 2069–2090.

Therrien R, 2008. Äspö Modelling Task Force – Modelling the KR24 pumping test at Onkalo Task 7A. SKB ITD-09-07, Svensk Kärnbränslehantering AB.

1.1 Background

Olkiluoto is an island covering about 10 km^2, located on the coast of the Baltic Sea and separated from the mainland by a narrow strait. A repository for spent fuel is planned for in the central part of the island (Figure 1-1). The island has a continental climate but temperatures are affected by the sea. For example, spring temperatures are significantly lower on the island than on the mainland. In the fall, the warmer sea reduces the temperature fluctuations between day and night such that frosts are rare. Winters are usually temperate. The mean temperature at Olkiluoto in the period of 1992 to 2001 was 5.8°C. The snow thickness is usually less than 20 cm and the water equivalent of snow is below 40 mm. The amount of snow varies during winter, when temperatures fluctuate around 0°C.

The main geological formation at the Olkiluoto site is a composite gneiss that contains fracture zones with an observed fracture frequency of 1−3 fractures/m. Site investigation suggests that subhorizontal fracture zones are the most hydraulically-conductive features at the site. These fracture zones can be connected through some open boreholes that have been drilled during site investigation for the purpose of flow logging. The impact of these open boreholes on fluid flow in these fracture zones is however unknown. Borehole KR24, visible within the circled area in Figure 1-1, was used for a long-term pumping test.

The site investigations will culminate in the construction of the ONKALO underground rock characterization facility. This construction work started in July 2004. The investigations in the ONKALO are an essential support for the application of the construction license for the repository.

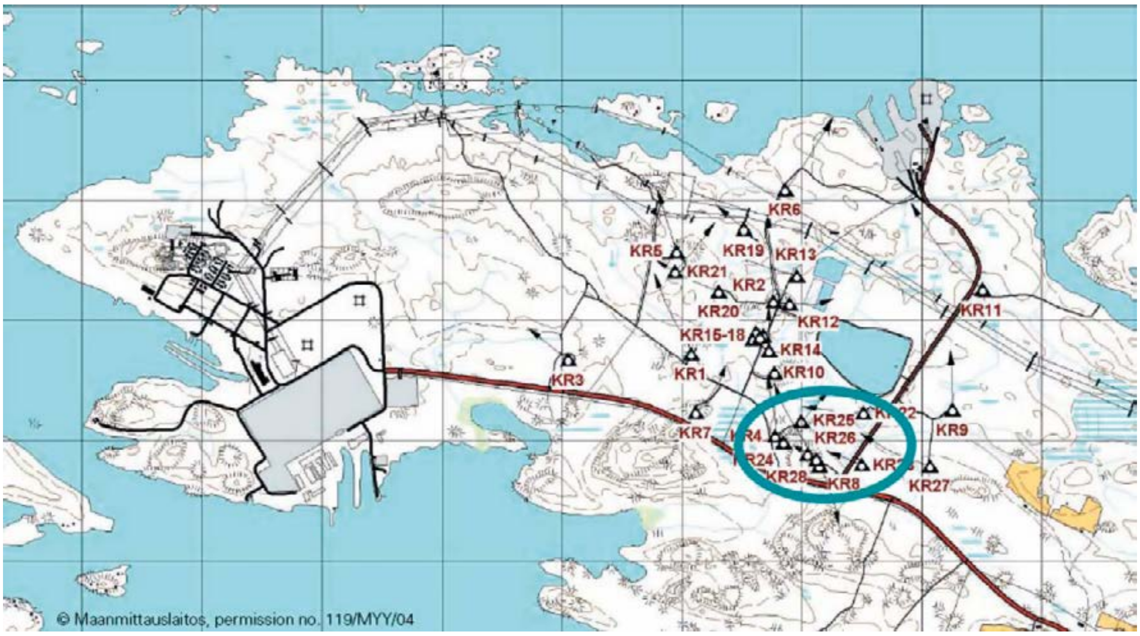

Figure 1-1. Plan view of Olkiluoto Island, with a grid size of 500 m, where the location of the Onkalo Underground Research Facility is circled (Figure taken from Vidstrand et al. 2015).

2 Task 7A

The overall objective of Task 7A were to (Vidstrand et al. 2015):

- understand the major features of the groundwater system,
- understand the consequences of the tests and measurement systems used, such as the open boreholes,
- understand how to model open boreholes within site characterisation studies and for the provision of parameters for PA,
- understand how PFL measurements could reduce uncertainty in models as compared to models calibrated with only head measurements,
- increase understanding of compartmentalisation and connectivity at the Olkiluoto site and more generally in fractured crystalline rock,
- evaluate how uncertainty in PA can be reduced based on the analysis of the Olkiluoto dataset.

To reach these objectives, Task 7A was split into the following subtasks (Vidstrand et al. 2015):

- (7A1) : Hydrostructural model implementation.
- (7A2) : Pathway Simulation within fracture zones.
- (7A3) : Ideas for calculation of PA relevant parameters from open borehole information.
- (7A4) : Calibration for possible compartmentalisation or natural trends from open borehole information.
- (7A5): Quantification of transport resistance distributions along pathways.

The work presented in this section primarily focused on subtasks 7A1 and 7A2, which required forward and inverse modelling. Subtasks 7A4 and 7A5 were closely related and somewhat overlapped 7A1 and 7A2, because they also required inverse modelling, to improve the model and address issues of such as compartmentalisation. Some inverse modelling was done within subtasks 7A1, but not sufficiently to obtain a calibrated model that could then be used to address the objectives of 7A4 and 7A5. These two latter subtasks are therefore not discussed separately from 7A1 and 7A2 in the report. Finally, subtask 7A3 was not addressed during the work because it focused on specific PA measures that are not of immediate concern to the delegates of the NWMO.

2.1 Site Description

Task 7A considers an area of about 10 km^2 around KR24 and focuses on the long-term pumping test undertaken between March 25, 2004 and June 2, 2004 in the 550-m deep KR24 borehole. This borehole is located at the planned ventilation shaft of the ONKALO underground rock characterization facility. The intent of the long-term pumping test was to support the large-scale (100 m to 1 km) characterization of properties of hydraulically conductive zones and other bedrock properties around the planned ventilation shaft.

2.1.1 Borehole KR24 pumping test

During the pumping test, pressure responses were recorded in open, shallow and deep boreholes, in multilevel piezometers, and in packed-off shallow and deep boreholes. Altogether, 139 measuring sections in 68 observation boreholes and 2 measuring sections in pumped borehole KR24 were included in the monitoring program to detect pressure responses. A unique aspect of the KR24 pumping test was that flow responses were logged along the length of 12 open boreholes (Vaittinen and Ahokas 2005).

Drawdown measured in 8 open boreholes during the pumping test is shown in Figure 2-1. For most boreholes, there is an initial sharp increase in drawdown, occurring in the first few days after the start of the test. The rate of increase then slows down after a few days but the drawdown continues to increase until the end of pumping at 69 days. At least part of the drawdown observed after the initial sharp increase has been attributed to a seasonal trend in declining heads, which has been observed in several other observation wells and boreholes on the island (Vidstrand et al. 2015). Drawdown sharply decreases immediately after pumping stops after 69 days, but it does not go back to the initial value of zero at the end of the measurement period for the test.

The drawdown curves shown in Figure 2-1 all have similar shape. Some curves are also almost identical during the pumping period and three groups of boreholes can be identified according to the similarity in measured drawdown. The first group, with the largest drawdown, contains boreholes KR8, KR10, KR22 and KR28. The second group contains KR4, KR7 and KR14 and show very similar drawdown, especially between about 30 days and the end of pumping at 69 days. The last group contains only KR27, which show a smaller drawdown than the other boreholes. Interestingly, this similarity in response within a group does not remain once pumping has stopped and water levels recover.

2.1.2 Data for the Task

There is a very large amount of information and data available for the Olkiluoto Island and the Task Secretariat was responsible for identifying relevant data. That data was posted a series of Data Deliveries on the Task Force web site. Table 2-1 lists the data and data files that were directly used to set up the model for Task 7A, either to define the geometry of the 3D mesh, hydraulic zones and borehole, or to define boundary conditions.

Table 2-1. Identification of data and data files used to set up the model for Task 7A.

Type of data and filename	Data Delivery and filename	Purpose
Pressure response during pumping test	6 – Open_KR_all_KRB.xls	Calculate drawdown at the end of the test, and plot transient drawdown response
Coordinates of boreholes	8 – *.pth files	To represent borehole as 1D elements in the model
Geometry of the zones	8 – largefaces4.txt	To represent hydraulic zones as 2D fracture elements in the model
Surface topography	9 – topo2.dat	To specify the top elevation of the 3D model, from interpolation of data in topo2.dat
Groundwater table elevation	12 – GW-table.txt	To specify the prescribed head boundary condition for all nodes at the top of the 3D model, from interpolation of data in GW-table.txt

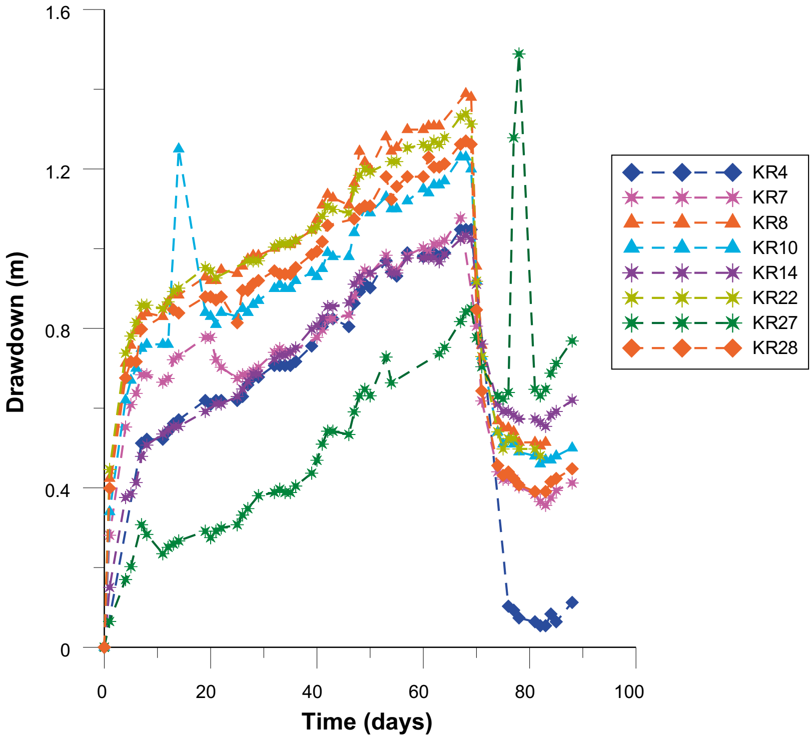

***Figure 2-1.** Observed drawdown in some open boreholes during the KR24 pumping test. The time equal to zero is at the start of pumping on March 25, 2004.*

2.2 Numerical model

The Task 7A simulations have been done with HydroGeoSphere, which is a control volume finite element model based on a FRAC3DVS formulation. FRAC3DVS is a 3D variable-density saturated-unsaturated numerical groundwater flow and multi-component solute transport model (Therrien and Sudicky 1996, Therrien et al. 2003, Graf and Therrien 2005). The model solves for fluid flow and solute transport in a 3D porous matrix that can contain 2D fractures and 1D wells. The model is still undergoing development, mainly at Université Laval and at the University of Waterloo. For example, a recent version, FRAC3DVS_OPG (Therrien et al. 2007), has been developed in cooperation with Ontario Power Generation under quality assurance and quality control constraints. HydroGeoSphere is an extended version of FRAC3DVS with capabilities to simulate coupled surface and subsurface fluid flow and solute transport (Therrien et al. 2009). HydroGeoSphere uses the same FORTRAN subroutines as FRAC3DVS and FRAC3DVS_OPG for solving subsurface flow and transport. Since the surface water flow capabilities are not used here, the HydroGeoSphere simulations presented here produce results that would be similar to those produced by either FRAC3DVS or FRAC3DVS_OPG.

2.2.1 Governing equations for flow

HydroGeoSphere considers that the porous matrix, the fractures and the wells (boreholes) all form separate continua. The governing flow equations in all continua are derived from the continuum approach, assuming local mass conservation and Darcian flow. HydroGeoSphere describes groundwater flow in the 3D porous matrix by

$$-\nabla \cdot q + \sum \Gamma_{ex} \pm Q = S_s \frac{\partial h}{\partial t} \qquad (2\text{-}1)$$

where ∇ is the 3D Nabla operator [L^{-1}], q is the fluid flux [$L\ T^{-1}$], Γ_{ex} represents fluid exchange with other domains such as fractures and wells [T^{-1}], Q is a volumetric source or sink [T^{-1}], S_s is the specific storage coefficient [L^{-1}], h is hydraulic head [L] and t is time [T]. The fluid flux is calculated using Darcy's law

$$q = -K \cdot \nabla h \qquad (2\text{-}2)$$

where K is the hydraulic conductivity tensor of the porous medium [$L\ T^{-1}$].

In 2D discrete fractures, groundwater flow is described by

$$-\overline{\overline{\nabla}} \cdot \left[(2b) q_f\right] - (2b)\Gamma_f = (2b) S_{sf} \frac{\partial h_f}{\partial t} \qquad (2\text{-}3)$$

where subscript f denotes refers to fractures, $\overline{\overline{\nabla}}$ is the 2D Nabla operator [L^{-1}], ($2b$) is the fracture aperture [L], q_f is fluid flux in the fracture [$L\ T^{-1}$], Γ_f is fluid exchange with other domains [T^{-1}], and S_{sf} and h_f are the specific storage coefficient [L^{-1}] and hydraulic head [L] for the fractures, respectively. The fluid flux in a fracture is given by

$$q_f = -K_f \cdot \overline{\overline{\nabla}} h_f \qquad (2\text{-}4)$$

where K_f [$L\ T^{-1}$] is the hydraulic conductivity of the fracture given by

$$K_f = \frac{(2b)^2 \rho g}{12 \mu} \qquad (2\text{-}5)$$

where g is the acceleration due to gravity [$L\ T^{-2}$] and μ and ρ are the water viscosity [$M\ L^{-1}\ T^{-1}$] and density [$M\ L^{-3}$], respectively.

The following equation describes groundwater flow for 1D wells

$$-\overline{\nabla} \cdot \left(\pi r_s^2 q_w\right) \pm Q_w \delta(l - l') - \pi r_s^2 \Gamma_w = \pi \left[\left(\frac{r_c^2}{L_s} + r_s^2 S_{sw}\right) h_w\right] \qquad (2\text{-}6)$$

where $\overline{\nabla}$ is the 1D Nabla operator [L^{-1}], r_s and r_c are the radii of the well screen and casing [L], respectively, q_w is Darcy flux in the well [$L\ T^{-1}$], Q_w is the pumping rate per length unit [$L^2\ T^{-1}$], l' is the location of the pump [L], Γ_w represents fluid exchange with other domains [T^{-1}], L_s is the length of the screen [L], S_{sw} is the specific storage coefficient in the well [L^{-1}] and h_w is the hydraulic head [L] in the well. The fluid flux in the well is calculated with

$$q_w = -K_w \cdot \overline{\nabla} h_w \tag{2-7}$$

where K_w [L T^{-1}] is the hydraulic conductivity of the well given by

$$K_f = \frac{r_c^2 \rho g}{8\mu} \tag{2-8}$$

2.2.2 Element types

To solve the governing flow equations, the model uses a control volume finite element formulation, which will be described in more detail in Section 2.2.3. The porous matrix is represented by three-dimensional finite element blocks or prisms (Figure 2-2). Fractures are represented by two-dimensional rectangular or triangular elements and one-dimensional elements are used to represent wells. The 2D fracture elements can correspond to 2D faces of the 3D matrix elements, while the 1D well elements generally correspond to 1D segments, or edges, of 3D elements.

Fractures and wells are incorporated into the 3D mesh by superimposing 2D faces and 1D segments onto 3D matrix elements. One example of such superposition for rectangular fracture faces is shown in Figure 2-3. Segments, faces and blocks share common nodes to fully couple groundwater flow. Thus, nodes at well and fracture locations receive contributions from both the porous matrix elements and from well segments and fracture faces. Hydraulic heads at these mutual nodes are assumed to be equal for the matrix, fractures and wells. The discretized equations arising from superposition of domains are presented in Section 2.2.3.

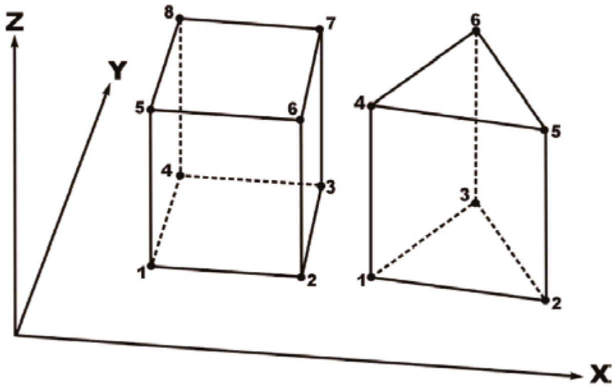

Figure 2-2. Matrix element types and local node numbering convention. An eight-node rectangular prism is shown to the left and a six-node triangular prism is shown to the right.

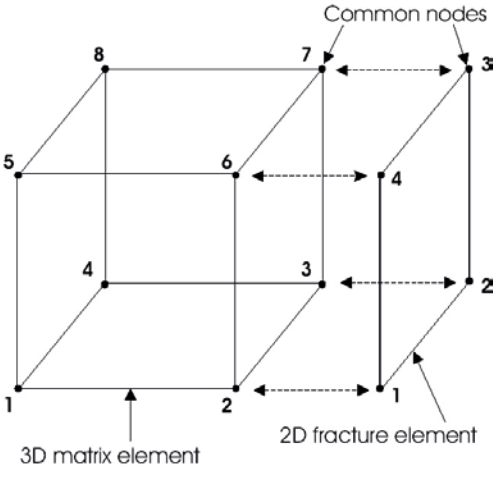

Figure 2-3. Example of superposition of 2D fracture faces onto 3D matrix blocks. For example, fracture node 1 and matrix node 2 have the same spatial coordinates.

Previous versions of the model were limited to mutually-orthogonal fracture representations and fracture elements had to correspond to a 3D element face. Figure 2-3 illustrates such representation. As part of Task 7A, and for the purpose of simulating the KR24 pumping test, Graf and Therrien (2008) have modified the model such that fracture faces are no longer restricted to 3D element faces. The methodology is based on a geometrically simple representation of the 3D domain with regular 3D rectangular prism elements, such as that shown in Figure 2-2, but fractures can be either triangle or rectangle with the constraint that they share nodes with the 3D elements. Examples of spatial relationships between fractures and matrix blocks developed by Graf and Therrien (2008) are shown in Figure 2-4. This modification has been very useful here to discretize the hydraulic zones.

2.2.3 Numerical formulation

A control volume finite element (CVFE) method is used to spatially discretize the flow equation, ensuring mass conservation at the local and global levels. The CVFE method formulates a mass balance for volumes associated to each node *i*. A nodal control volume is obtained by connecting the centroids of elements that contain node *i* with the midpoints of segments that join node *i* with its neighbouring nodes, such as node *j* in Figure 2-5.

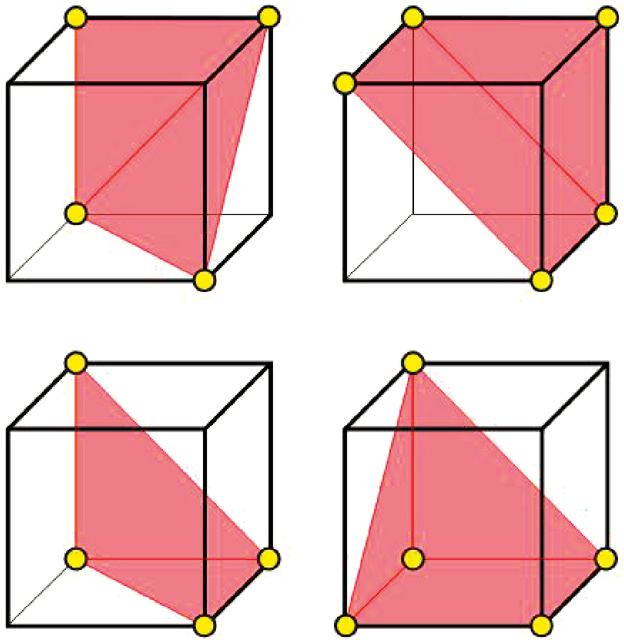

Figure 2-4. *Examples of locations of 2D fracture elements within a 3D hexahedral element (from Graf and Therrien 2008).*

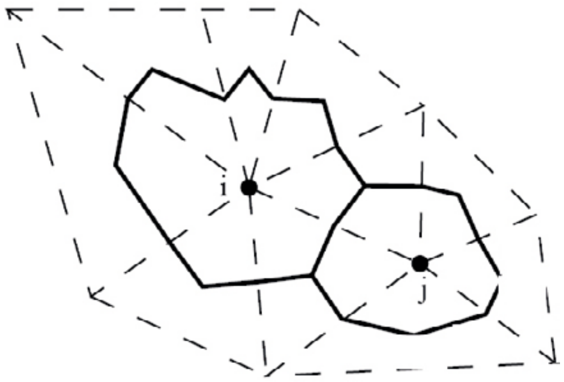

Figure 2-5. *Nodal control volumes associated with nodes i and j.*

Using the control volume finite element method, with fully implicit time weighting, the following discretized porous medium flow equation is obtained for node *i*:

$$\sum_{j\in\eta_i}\gamma_{ij}\left(h_j^{L+1}-h_i^{L+1}\right)-\left(\sum\Gamma_{ex}\right)v_i \pm Q_i^{L+1}=S_s v_i\frac{\left(h_i^{L+1}-h_i^{L}\right)}{\Delta t} \tag{2-9}$$

where η_i is the set of neighbour nodes that belong to the same elements as node *I* and where

$$\gamma_{ij}=\int_v \nabla N_i\cdot K\cdot\nabla N_j dv \tag{2-10}$$

for interpolation functions *N* defined for the 3D porous medium elements and where the 3D volume v_i associated with a given node is:

$$v_i=\int_v N_i dv \tag{2-11}$$

Using the same approach, the discretized 2D equation for flow in fractures is

$$\sum_{j\in\eta_{f_i}}\gamma'_{ij}\left(h_{fj}^{L+1}-h_{fi}^{L+1}\right)+(2b)\Gamma_f^{L+1}a_i=(2b)S_{sf}a_i\frac{\left(h_{fi}^{L+1}-h_{fi}^{L}\right)}{\Delta t} \tag{2-12}$$

where η_{fi} is the set of fracture nodes that belong to the same fracture elements as node *i* and where

$$\gamma'_{ij}=\int_a \nabla N'_i\cdot(2b)K_f\cdot\nabla N'_j\, da \tag{2-13}$$

for interpolation functions *N'* defined for the 2D fracture medium elements. The 2D area a_i associated with a given fracture node is

$$a_i=\int_a N'_i da \tag{2-14}$$

Finally, the discretized 1D equation for flow along the axis of a well can be obtained in a similar manner and is

$$\sum_{j\in\eta_{wi}}\gamma''_{ij}\left(h_{wj}^{L+1}-h_{wi}^{L+1}\right)+\pi r_s^2\Gamma_w^{L+1}l_i+Q_{wi}^{L+1}=\pi l_i\left(\frac{r_c^2}{L_s}+r_s^2S_{sw}\right)\frac{\left(h_{wi}^{L+1}-h_{wi}^{L}\right)}{\Delta t} \tag{2-15}$$

where η_{wi} is the set of well nodes that belong to the same well elements as node *i* and where

$$\gamma''_{ij}=\int_l K_w\nabla N''_i\cdot\nabla N''_j\, dl \tag{2-16}$$

for interpolation functions *N"* defined for the 1D well medium elements and where the 1D length l_i associated with a given well node is

$$l_i=\int_l N''_i dl \tag{2-17}$$

Coupling of the mass balance equations between different media is done by replacing the coupling term Γ in Equation (2-9) by its representation in either the discretized fracture or well equation. For example, the coupling term Γ_f for fractures obtained from Equation (2-12) is

$$(2b)\Gamma_f^{L+1}a_i=(2b)S_{sf}a_i\frac{\left(h_{fi}^{L+1}-h_{fi}^{L}\right)}{\Delta t}-\sum_{j\in\eta_{f_i}}\gamma'_{ij}\left(h_{fj}^{L+1}-h_{fi}^{L+1}\right) \tag{2-18}$$

Upon replacing the above expression (2-18) for Γ_f into Equation (2-9), the following discretized equation is obtained for node *i* that belong to both 3D porous medium elements and 2D fracture elements

$$\sum_{j\in\eta_i}\gamma_{ij}\left(h_j^{L+1}-h_i^{L+1}\right)+\sum_{j\in\eta_{f_i}}\gamma'_{ij}\left(h_{fj}^{L+1}-h_{fi}^{L+1}\right)\pm Q_i^{L+1}=$$

$$S_s v_i\frac{\left(h_i^{L+1}-h_i^{L}\right)}{\Delta t}+(2b)S_{sf}a_i\frac{\left(h_{fi}^{L+1}-h_{fi}^{L}\right)}{\Delta t} \tag{2-19}$$

In Equation (2-19), we assume that $h_i = h_{fi}$ for a node that are common to the porous medium and fracture domains, which ensures continuity of hydraulic head. The exact value of the fluid exchange between the domains, Γ_f, is therefore not computed explicitly prior to solution, but it can be back-calculated during post-processing of results by evaluating Equation (2-18) at the desired nodes. Similarly to the approach shown here for superposition of the 2 domains, the model allows superposition of the well domain by adding the relevant discretized equations and assuming continuity of head. Back calculation of the well exchange term, Γ_f, has used in Task 7A to calculate the inflow into and out of boreholes.

The global system of equations is obtained by element-wise assembly of the discretized flow equation over each control volume. The global system of equations has the following matrix form

$$[A]\{h\} = \{b\} \tag{2-20}$$

where A is the global matrix, h is the vector of unknown hydraulic heads (h_i) and b is the known boundary flux vector. HydroGeoSphere solves Equation (2-20) with an efficient ILU-preconditioned iterative sparse-matrix solver (Therrien et al. 2009).

Variable time-stepping is used to reduce computational times, with time step size Δt^{L+1} computed from previous time step Δt^L according to

$$\Delta t^{L+1} = \left(\frac{h_{\max}}{\max\left| h_i^{L+1} - h_i^L \right|} \right) \Delta t^L \tag{2-21}$$

where h_{max} is the maximum change of hydraulic head [L] allowed during a time step and L is the time level.

2.2.4 Particle tracking and solute transport

Particle tracking was needed for subtask 7A2, but HydroGeoSphere does not have a built-in particle tracking module. Instead, HydroGeoSphere writes to a file the computed elemental velocities in the x-, y-, and z-directions for the 3D matrix elements and the 2D fracture elements. These velocities are then read by the Tecplot software, which is used for particle tracking. There is no clear description of the particle tracking algorithm in the Tecplot and the particle tracking option is therefore used with caution here, since it is difficult to assess its precision.

Advective-dispersive transport simulations were not explicitly required for Task 7A, unless salinity was accounted for, which was not done here. The advective-dispersive transport capabilities of HydroGeoSphere were, however, used to calculate life expectancy and provide some answers to subtask 7A2. The advective-dispersive transport capabilities of the model, as well as a brief description of life expectancy are given below.

HydroGeoSphere can simulate groundwater age and life expectancy based on reservoir theory (Therrien et al. 2009, Cornaton et al. 2008). For a given groundwater reservoir (Figure 2-6), the groundwater age at a given location is the time of travel of groundwater from an inlet boundary to the location, while the groundwater life expectancy is the time of travel from the location to an exit boundary. The computation of groundwater age and life expectancy are based on a forward and backward solution of the advective-dispersive transport equations, respectively. For groundwater age calculations, a prescribed age equal to zero is imposed at inflow boundaries and an additional source term is used to continuously generate age during a simulation. The groundwater life expectancy is computed by solving the adjoint equation for transport, which is the backward-in-time solution with a reversed flow field, and by specifying appropriate boundary conditions (Therrien et al. 2009). Both groundwater age and life expectancy can be considered as spatially random variables and the model computes the statistical characteristics of life expectancy at any given point, such as the mean value, the probability density function and the cumulative density function. Therrien et al. (2009) provide a more detailed description of these capabilities for HydroGeoSphere and Cornaton et al. (2008) present examples for a discrete fracture model.

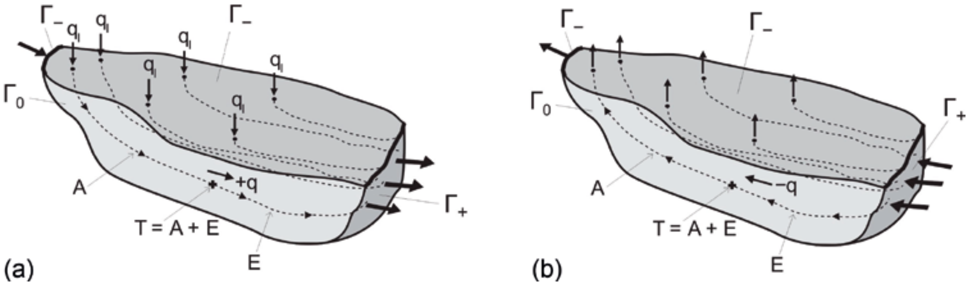

Figure 2-6. *Schematic illustration of a groundwater reservoir Γ_0 with inlet (Γ_-) and outlet (Γ_+) boundaries and showing (a) the normal flow field used to solve for groundwater age problem and (b) the reverse flow field used to solve for life expectancy. For a given location in the reservoir, the total transit time T is the sum of the age A and life expectancy E, where T, A, and E are random variables.*

Since simulations of groundwater age and life expectancy require the solution of the advection-dispersion equation, that equation is presented here for the 3D porous medium, although HydroGeoSphere also solves for advective-dispersive solute transport in fractures and boreholes. For the 3D porous medium, the advective-dispersive equations is

$$-\nabla\cdot\left(qc-\theta_s D\nabla C\right)+\sum\Omega_{ex}\pm Q_C=\theta_s R\frac{\partial C}{\partial t}+\theta_s R\lambda C \tag{2-22}$$

where C is the solute concentration [M L^{-3}], D is the hydrodynamic dispersion tensor [L^2 T^{-1}], θ_s is the saturated porosity, R is a dimensionless retardation factor and λ is a first-order decay constant [L^{-1}]. Solute exchange with the outside of the simulation domain, as specified from boundary conditions, is represented by Q_c [M L^{-3} T^{-1}] which represents a source (positive) or a sink (negative) to the porous medium system. In Equation (2-22), Ω_{ex} represents the mass exchange rate of solutes per unit volume [M L^{-3} T^{-1}] between the subsurface domain and all other types of domains supported by the model, such as fractures and wells.

Equations similar to (2-22) can be written for the 2D fracture elements and the 1D wells and the discretization, and coupling of the different domains, is similar to that already described for fluid flow and assumes continuity of concentration at common nodes.

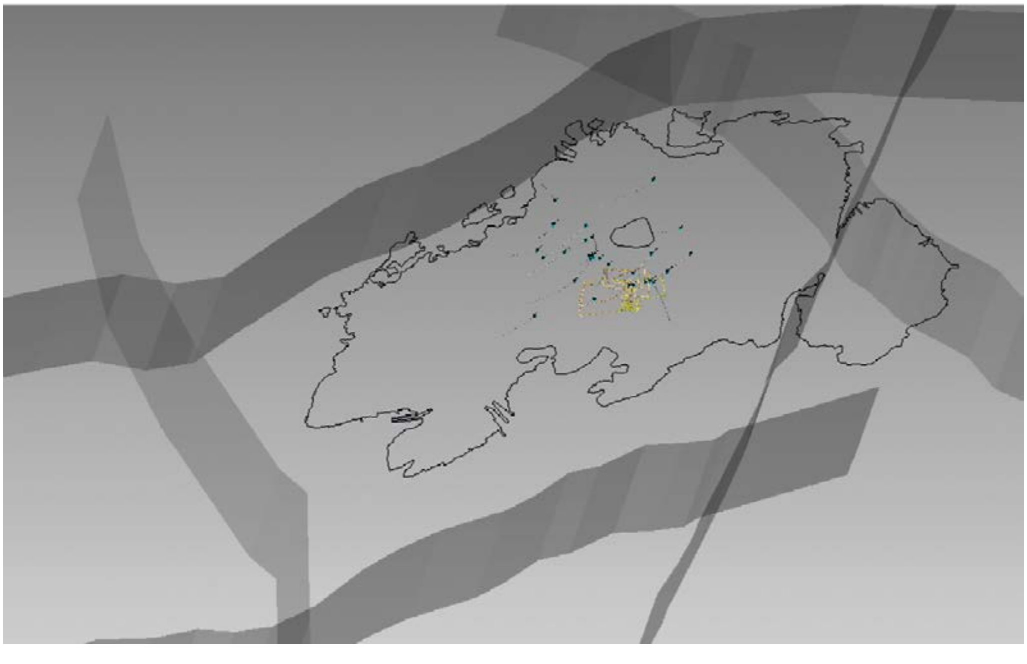

Figure 2-7. *Perspective view of Olkiluto Island, where the shaded areas are the traces of large-scale lineaments (figure taken from Vidstrand et al. 2015).*

2.3 Site model

The task description (Vidstrand et al. 2015) provided instructions on the design of the site model, including the geometry and hydraulic properties. The lateral extent of the simulation domain is approximately 6.5 km along the east-west direction and 4.5 km along the north-south direction (Figure 2-7). The shaded areas shown in Figure 2-7 are large-scale lineaments that form the lateral boundaries of the site model.

To represent the simulation domain, a three-dimensional finite element mesh has been generated with hexahedral (8-node) elements (Figure 2-8). The 3D mesh is created by first generating a 2D horizontal mesh to represent the lateral extent of the domain shown in Figure 2-7. The horizontal mesh spacing is 100 m in both x- and y-directions and it is gradually refined to 2 m near the KR24 borehole. The 2D mesh contains 9036 rectangular elements and 9242 nodes. This 2D mesh is then stacked in the third dimension to generate the 3D mesh for the whole domain. A total of 44 layers of nodes (and 43 layers of 3D elements) is generated for the 3D mesh, which contains 406 648 nodes and 388 548 elements. Nodes located at the bottom of the mesh are assigned a constant elevation equal to −1000 m. The elevation of the nodes at the top of the mesh is variable and has been interpolated from the surface topography. The nodal distribution of the 42 layers of nodes between the top and bottom layers is not constant. The layer of nodes directly below the top layer is at an elevation of −25 m and the vertical thickness of the first layer of 3D elements is therefore variable. The vertical nodal spacing is 17.5 m between elevations of −25 m and −200 m, it is 20 m between elevations of −200 m and −600 m and it increases to 50 m between elevations of −800 m and −1000 m.

A total of 13 hydraulic zones, listed in Table 2-2, are represented with two-dimensional elements in the model. The geometry of the discretized zones is shown in Figure 2-9 and they have been generated using the methodology of Graf and Therrien (2008) and the triangulated representation of the zones provided in the data delivery. Vidstrand et al. (2015) provide the geometric mean transmissivity for each zone. That transmissivity must be translated into an aperture in the model by using Equation (2-5) and, based on the cubic law, assuming that fracture transmissivity is the product of fracture hydraulic conductivity and aperture. The resulting apertures corresponding to these mean transmissivities are shown in Table 2-2. It is assumed that water compressibility is the only contribution to fluid storage in the hydraulic zones and the specific storage coefficient for all hydraulic zone elements is assumed equal to $3.52 \cdot 10^{-6}$ m^{-1}.

The background rock is discretized with 3D hexahedral elements. Two different sets of hydraulic properties are used (Table 2-3). The upper section of the rock mass, above an elevation of −70 m, is assigned a higher hydraulic conductivity than the lower section, which is assumed to have a very low hydraulic conductivity.

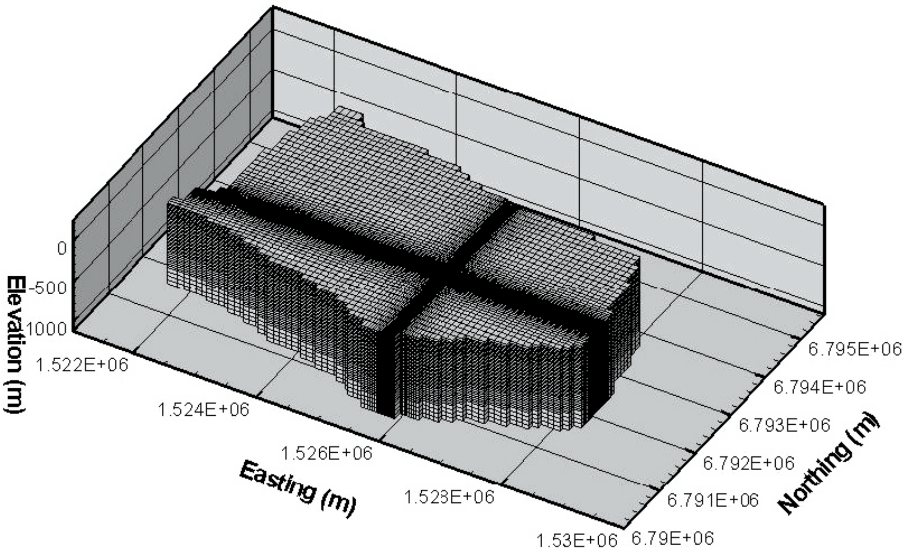

Figure 2-8. Extent of the site model and 3D mesh.

Table 2-2. Mean transmissivity and corresponding aperture of the hydraulic zones included in the site model.

Zone	Geometric mean transmissivity (m^2/s)	Aperture (m)	Number of 2D elements in mesh
HZ001	−7.9	$2.59 \cdot 10^{-5}$	1 400
HZ002	−6.0	$1.11 \cdot 10^{-4}$	205
HZ003	−6.2	$9.54 \cdot 10^{-5}$	148
HZ004	−6.8	$6.02 \cdot 10^{-5}$	5 921
HZ19A	−5.8	$1.30 \cdot 10^{-4}$	6 865
HZ008	−5.0	$2.40 \cdot 10^{-4}$	4 512
HZ19C	−5.5	$1.63 \cdot 10^{-4}$	7 183
HZ20A	−5.1	$2.22 \cdot 10^{-4}$	8 433
HZ20AE	−6.0	$1.11 \cdot 10^{-4}$	342
HZ20B_ALT	−5.5	$1.63 \cdot 10^{-4}$	8 790
HZ21	−7.8	$2.79 \cdot 10^{-5}$	10 710
HZ21B	−6.1	$1.03 \cdot 10^{-4}$	9 268
BFZ099	−7.8	$2.79 \cdot 10^{-5}$	9 966

Table 2-3. Hydraulic properties of the background rock.

Zone	Elevation	Hydraulic conductivity (m/s)	Specific storage (m^{-1})
Top	$z > -70$ m	$1 \cdot 10^{-7}$	$4.4 \cdot 10^{-6}$
Bottom	$z < -70$ m	$1 \cdot 10^{-12}$	$4.4 \cdot 10^{-6}$

A total of 9 open boreholes and 9 packed-off intervals are represented in the model with 1D line elements. The open boreholes are KR04, KR06, KR07, KR08, KR10, KR14, KR22, KR27, and KR28. Three packed-off are included for KR09, at the intersections with zones HZ19B, HZ19A, and HZ20BALT, respectively. One packed-off section is represented for both KR12 and KR23, at the intersections with HZ19C and HZ19A, respectively. Four packed-off sections are included for KR25 at the intersections with HZ19A, HZ19C, HZ20A, and HZ20B_ALT.

In addition to the open boreholes and packed-off sections, the upper and lower sections of KR24 are represented in the model. The two sections are discretized with a series of 1D line elements and the mesh is designed such that there is no direct connection between both sections. For all simulations with pumping at KR24, constant flow rates are imposed, with values equal to 12.5 L/min and 5 L/min for the upper and lower sections, respectively.

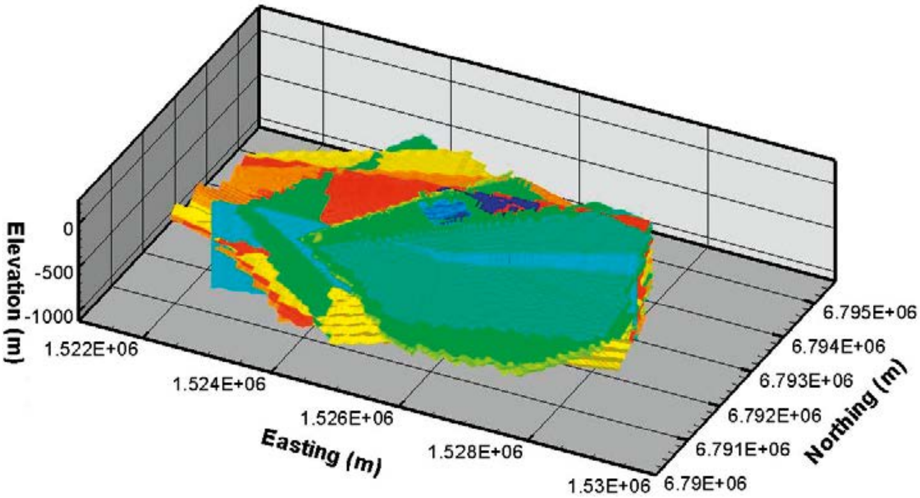

Figure 2-9. Representation of the hydraulic zones in the finite element model.

All 1D line elements in the model are assigned a radius equal to 0.01 m, which corresponds to a value of hydraulic conductivity equal to 9.4×10^7 m/day according to Equation (2-8). The hydraulic conductivity of the well elements is therefore several orders of magnitude larger than that of the hydraulic zones and the background rock. The radius of 0.01 m is smaller than the radius of all boreholes at the site but preliminary simulations showed that increasing the radius of the well elements did not change results compared to simulations with a radius of 0.01. The reason is that the contrasts in hydraulic conductivity between the wells and the hydraulic zones remained extremely large. On the other hand, computational times increased significantly when using the real borehole radius and, as a result, a radius equal to 0.01 m was kept for all simulations.`

The flow boundary conditions are imposed hydraulic heads for the nodes located at the top of the mesh and on the lateral boundaries. The imposed heads at the top of the mesh are interpolated from the ground water table elevation, and the heads on the lateral boundaries are all equal to sea level elevation (equal to 0.0 m). The bottom of the mesh is assumed impermeable and a second-type boundary condition, with no-flow, is imposed.

2.4 Simulations

Table 2-4 lists the simulations that have been either completed or attempted for Tasks 7A1 and 7A2. All forward simulations have been completed and inverse simulations have been attempted but without obtaining a calibrated model. Results shown here are therefore restricted to the forward simulations, with the input parameters specified in Section 2.3.

2.4.1 Steady-state flow without pumping (SS01 and SS02)

Simulations SS01 and SS02a are for steady-state flow under natural conditions, without pumping, without open borehole (SS01) and with open boreholes (SS02). Figure 2-10 shows the simulated hydraulic heads for SS01 on the edges of the domain, for the boundary conditions specified in Section 2.3. Since the hydraulic heads are imposed everywhere on the visible edges, Figure 2-10 really shows the interpolated hydraulic heads at the top of the domain, which represent the groundwater table elevation, as well as the imposed hydraulic head on the lateral sides, which is equal to the sea elevation (head = 0 m).

The influence of the highly-transmissive fracture zones on the simulated hydraulic heads is shown in Figure 2-11. The high-transmissivity fracture zones offer little resistance to groundwater flow such that the hydraulic gradient in the zones is very small. The hydraulic head distribution in the fracture zones therefore tend to reflect that at ground surface, where the head is imposed.

Table 2-4. List of simulations for Task 7A1 and Task 7A2. Simulations are in forward mode, except for those shaded in grey, which are in inverse mode.

Name	KR24 Pumping	Boreholes included	Status (Completed)	Performance measure file (Excel)
SS01	No	None	Yes	PM_SS01_MG_NWMO_20071019
SS02a	No	Open boreholes	Yes	PM_SS02a_MG_NWMO_20071019
SS02b	No	Open boreholes	No (but attempted)	
SS02c	No	None	No	
SS03	Yes	KR24 only	Yes	PM_SS03_MG_NWMO_20071019_20080122
SS04a	Yes	KR24 + monitoring	Yes	PM_SS04a_MG_NWMO_20071019_20080122
SS04b	Yes	KR24 + monitoring	No (but attempted)	
TR01	Yes	KR24 only	Yes	
TR02a	Yes	KR24 + monitoring	Yes	
TR02b	Yes	KR24 + monitoring	No	
PA01	No	None	Yes	Yes

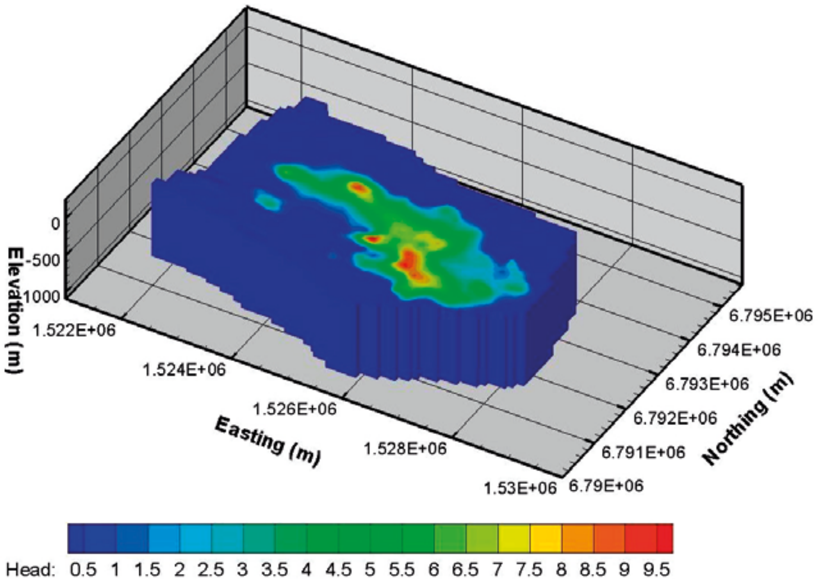

Figure 2-10. *Simulated hydraulic heads at the top and the edges of the domain for SS01.*

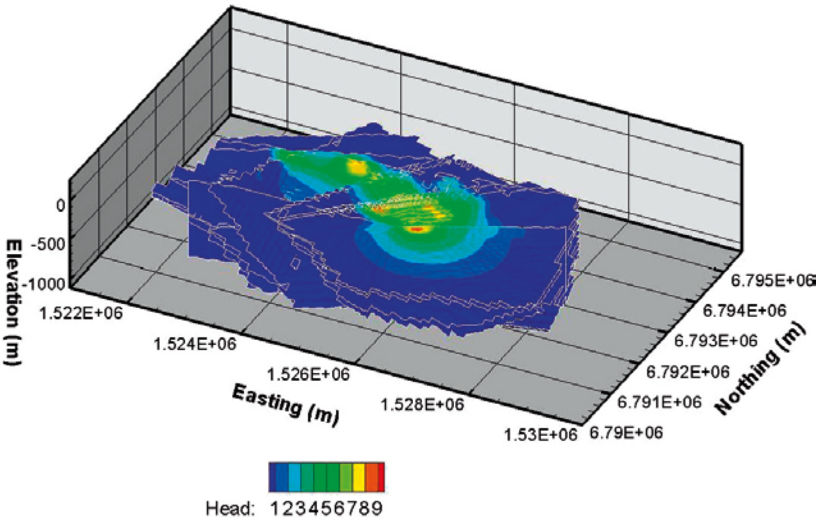

Figure 2-11. *Simulated hydraulic heads in the fracture zones for SS01.*

The influence of the open boreholes on some selected observation points can be seen in Figure 2-12. The hydraulic heads are shown as a function of elevation for the 17 performance measure points specified for Task 7A1 and 7A2, whose location is given in Vidstrand et al. (2015). For both SS01 and SS02a, there is a general trend of decreasing hydraulic head with depth. The open boreholes included in SS02a produce higher simulated hydraulic heads at greater depths (elevation < -300 m) compared to SS01. The reason is that the open boreholes create connections between hydraulic zones, which tend to increase the global hydraulic conductivity of the domain. Since the boundary conditions remain the same prescribed hydraulic heads for SS01 and SS02a, an increased global hydraulic conductivity leads to a decreased hydraulic gradient. Simulation SS02a indeed shows a smaller hydraulic gradient, which translates into less spreading of hydraulic head values as a function of elevation (Figure 2-12).

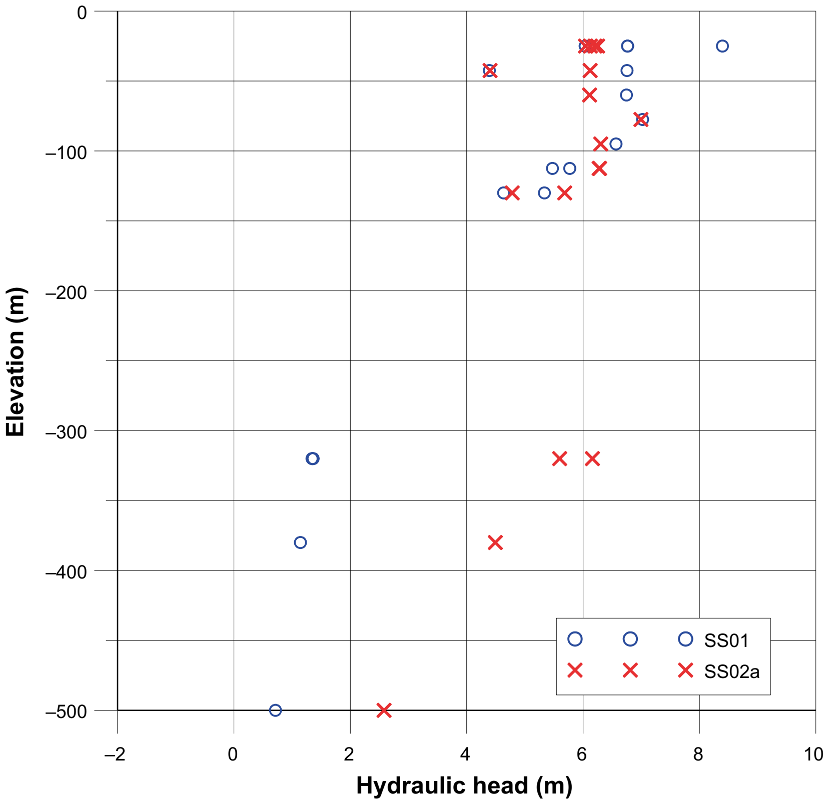

Figure 2-12. Simulated hydraulic head as a function of elevation at the performance measure points for SS01 and SS02a.

The observed and SS02a simulated hydraulic heads for some boreholes are compared and shown in Table 2-5 and Figure 2-13. The maximum and minimum absolute differences between simulated and observed heads are equal to 4.11 m and 0.04 m, respectively. For these eight boreholes, there is a greater spread in simulated hydraulic heads compared to the observed heads (Figure 2-13). Because these boreholes are several hundred meters long, the hydraulic head varies along the axis of the borehole and the degree of agreement between simulated and observed hydraulic heads can differ depending on the hydraulic head value selected for a given borehole.

Table 2-5. Simulated and observed hydraulic heads at selected boreholes for simulation SS02a.

Borehole	Observed hydraulic head (m)	Simulated hydraulic head (m)	Absolute difference (m)
KR04	6.03	6.25	0.22
KR07	5.21	6.20	0.99
KR08	6.18	4.40	1.78
KR10	5.89	4.78	0.89
KR14	6.69	2.58	4.11
KR22	6.08	6.04	0.04
KR27	6.64	6.13	0.51
KR28	5.80	6.12	0.32

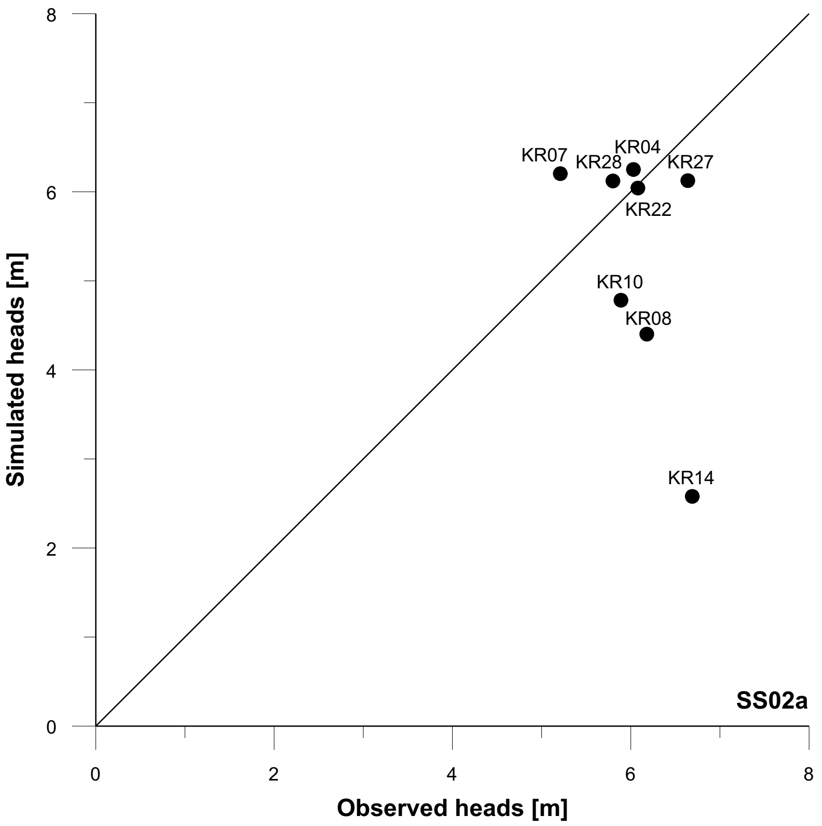

Figure 2-13. Comparison of simulated and observed hydraulic heads for SS02a for some open boreholes.

2.4.2 Steady-state flow with pumping (SS03 and SS04)

Simulations SS03 and SS04 explored steady-state flow conditions, with KR24 pumping, and with or without open boreholes. These simulations show that the impact of the open boreholes on simulated hydraulic heads when KR24 is pumping is similar to the impact already mentioned for case without pumping. The open boreholes tend to reduce the spread of hydraulic head values with depth. The effect of the boreholes is seen when comparing the computed drawdown as a function of elevation for SS03 and SS04a (Figure 2-14). Including the open boreholes for the SS04a simulations reduces drawdown at depth compared to SS03.

The same observation of the impact of the open borehole can be made from looking at the drawdown as a function of the horizontal distance between KR24 and the location of each performance measure point (Figure 2-15). The decrease in drawdown for SS04a is, however, more pronounced for shorter distances to KR24 compared to the performance measure points that are located further away.

Inflow in and out of boreholes

The inflow in and out of boreholes, at the intersection with hydraulic zones, is computed by the model and can be compared for the different simulations. Table 2-6 shows such inflow values for simulations SS02 and SS04b, to compare the case with and without pumping at KR24. The selected boreholes and intervals are those specified in the performance measures.

When pumping borehole KR24, the total withdrawal rate is split into the three intersected zones in the model, with the highest inflow computed for HZ20A, which is the zone with the highest transmissivity in the model. The inflows for the other boreholes listed in Table 2-6 do not change significantly if KR24 is pumped or not. There is no reversal of flow direction except for the intersection between KR06 and BFZ099, where the lowest absolute flow rates are computed.

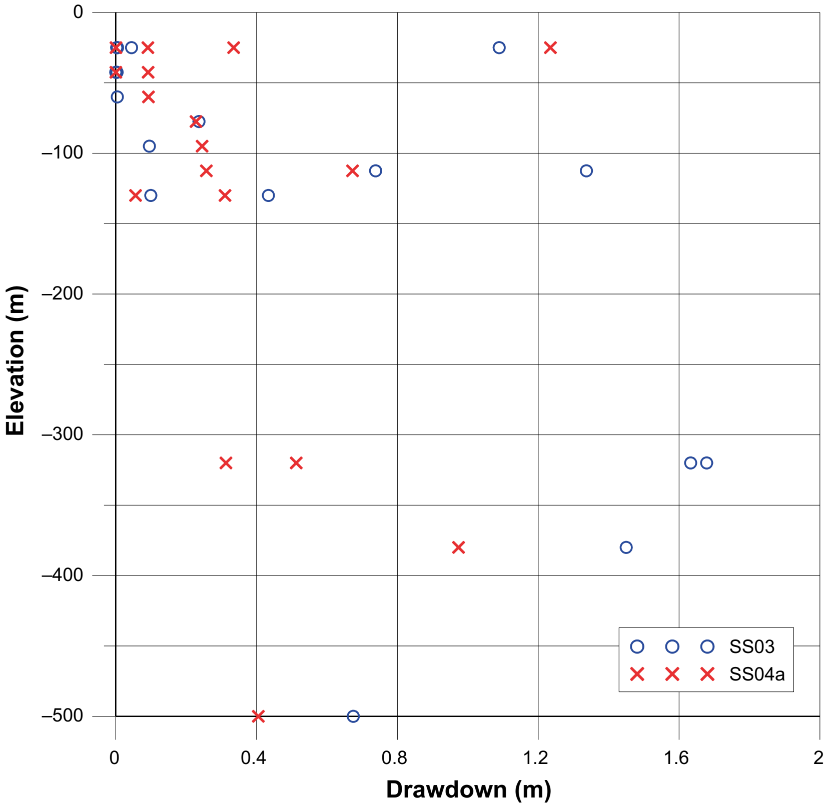

Figure 2-14. *Simulated hydraulic heads as a function of elevation at the performance measure points for SS03 and SS04a.*

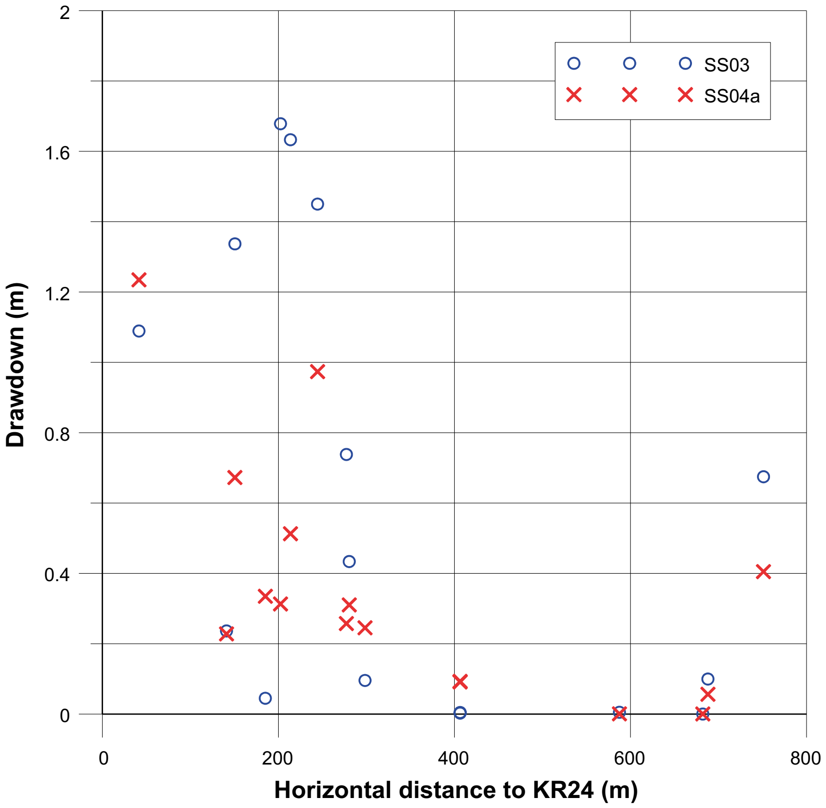

Figure 2-15. *Drawdown as a function of the horizontal distance between KR04 and the performance measure points for SS03 and SS04a.*

Table 2-6. Inflow at intersections between boreholes and hydraulic zones SS02 and SS04a. A positive value is for flow from the borehole to the hydraulic zone and a negative value is for flow in the opposite direction.

Borehole	Intersection	Flow rate, no pumping, SS02 (m^3/day)	Flow rate, pumping, SS04 (m^3/day)
KR24	HZ20B_ALT	1.15E−01	−1.53E+00
	HZ20A	1.59E−01	−4.11E+00
	HZ19C	−2.74E−01	−2.26E+00
KR06	HZ21	3.72E−03	3.97E−03
	HZ21B	1.45E−01	1.53E−01
	HZ001	−1.46E−03	−1.51E−03
	BFZ009	−5.96E−05	3.46E−05
KR14	HZ001	9.15E−04	1.03E−03
	HZ20B_ALT	2.46E−04	2.80E−04
	HZ20A	9.85E−05	1.08E−04
KR22	HZ002	3.54E−04	5.99E−04
	HZ19C	3.21E−04	5.44E−04
	HZ20A	2.58E−04	3.52E−04
	HZ19C	−3.44E−01	−4.88E−01
	HZ19A	−3.56E−01	−5.22E−01

2.4.3 Transient flow with pumping (TR01 and TR02)

For the transient simulations, adaptive time stepping was used, with maximum change of hydraulic head h_{max} equal to 0.75 m (see Equation 2-21), an initial time step of 0.1 day, a maximum time step of 5 days and a maximum time step multiplier of 5. The simulation was run for 90 days and the total number of time steps for TR01 and TR02 was 152 and 144, respectively. Constant flow rates of 12.5 L/min and 5 L/min were imposed at the upper and lower section of KR24, respectively, for the first 69 days and both flow rates were set to zero from 69 days to 90 days to simulate recovery.

The initial hydraulic heads for TR01 are the simulated heads for case SS02a, which is for steady-state flow where only KR24 is represented in the model, which is similar to TR01. The initial hydraulic heads for TR02 are the simulated steady-state heads for SS03, where KR24 and monitoring boreholes are represented in the model. Both sets of initial heads do not match the observed heads and therefore introduce an error during transient flow calibration. This error can be seen in Figure 2-16 for TR02, where the observed and simulated heads for a given interval are different at a time of zero. As a result, it is better to compare simulated drawdowns (Figure 2-17), since both observed and simulated drawdown are initially equal to zero.

The simulated drawdown for the observation boreholes initially increases rapidly (Figure 2-17), which matches the observed drawdown relatively well, but it stabilizes after about 20 to 30 days for all boreholes, while the observed drawdown continued to increase until the end of pumping. This continuous increase of drawdown has been attributed to a regional decrease of hydraulic head during the pumping test, rather than the effect of pumping KR24 (Vidstrand et al. 2015).

Figure 2-18 compares the simulated drawdown with observed drawdown to which a constant value of 1 cm/day has been subtracted. The value of 1 cm/day has been estimated from the analysis presented by Vidstrand et al. (2015) and the intent here is to find if a better match of drawdown is obtained when the natural decreasing trend is removed. The simulated drawdown is closer to the detrended drawdown than the observed drawdown, but there are still significant differences.

A comparison of individual drawdown values at the end of pumping (Table 2-7 and Figure 2-19) show that simulated drawdown agree with most of the detrended observations, with differences less than 0.40 m for all intervals except KR04.

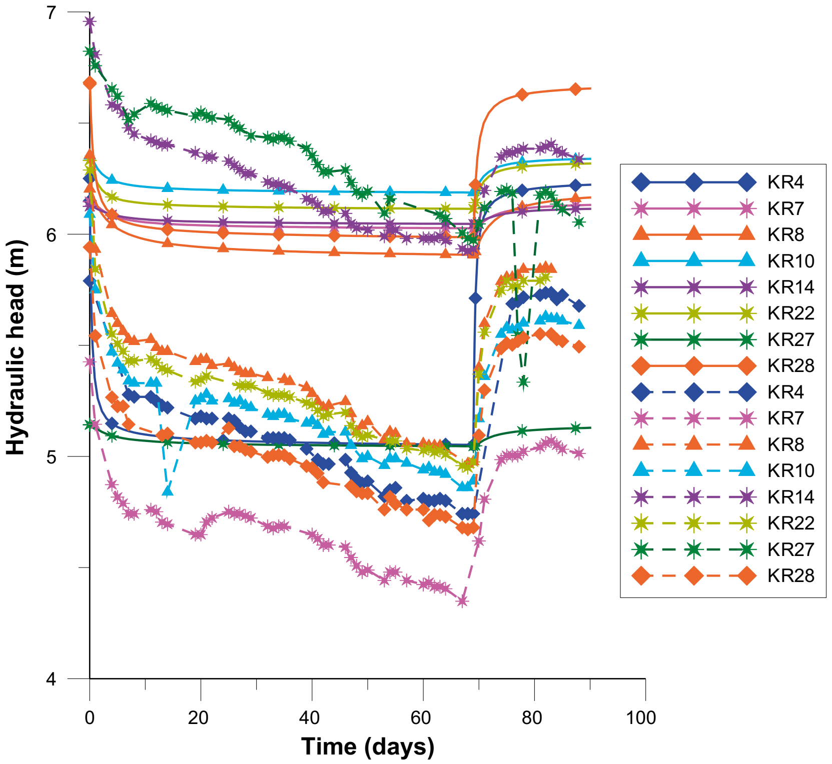

Figure 2-16. *Simulated (solid lines) and observed (dashed lines) hydraulic heads for TR02a.*

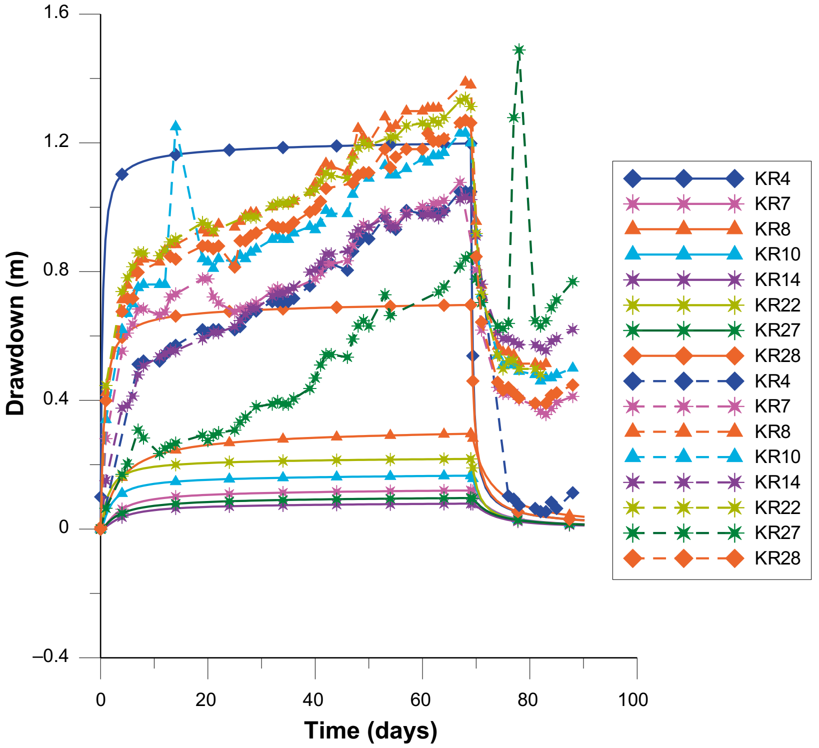

Figure 2-17. *Simulated (solid lines) and observed (dashed lines) drawdowns for TR02a.*

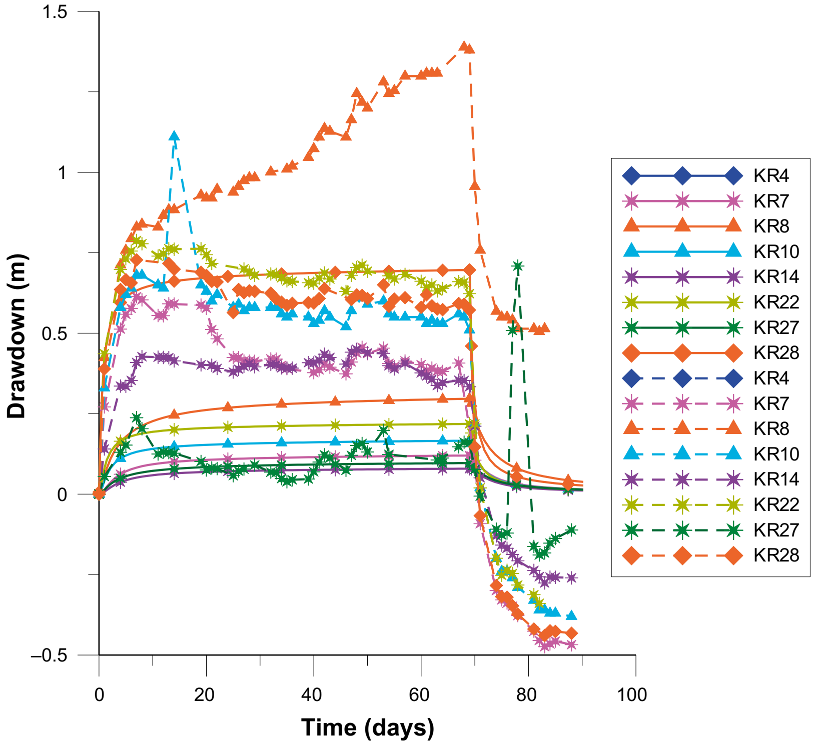

***Figure 2-18.** Simulated (solid lines) and "detrended" observed (dashed lines) drawdowns for TR02a. The detrented drawdowns are the observed drawdowns to which a value of 1 cm/day has been subtracted.*

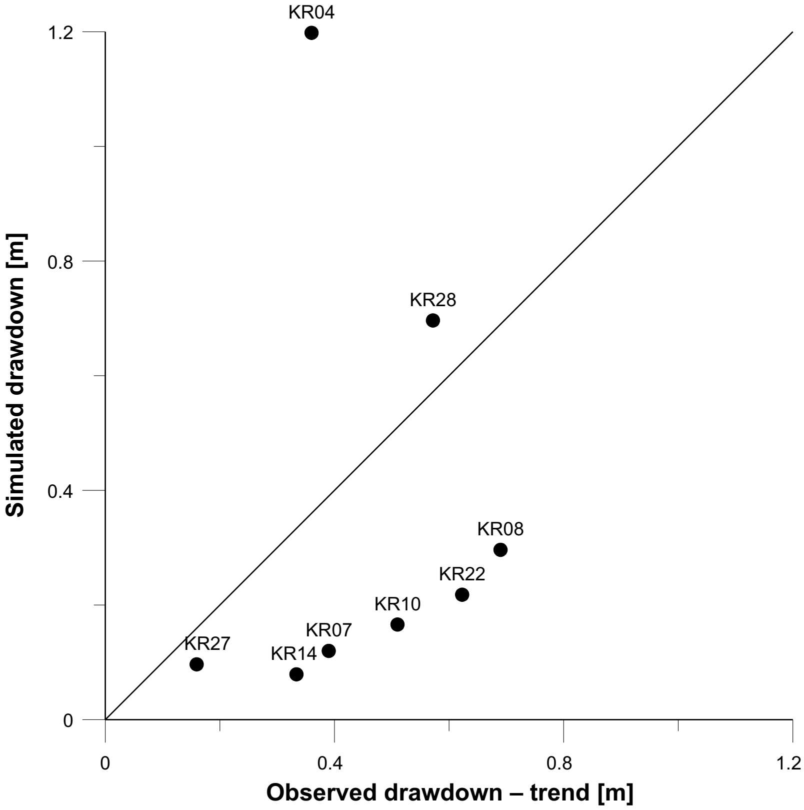

***Figure 2-19.** Observed drawdown (minus a trend) and simulated drawdown after 69 days, at the end of pumping.*

Table 2-7. Simulated and observed drawdown at selected boreholes and at the end of pumping (after 69 days) for simulation TR01.

Borehole	Observed drawdown (m)	Observed drawdown minus trend (m)	Simulated drawdown (m)	Absolute difference simulated – observed (m)	Absolute difference simulated – observed – trend (m)
KR04	1.05	0.36	1.20	0.15	0.84
KR07	1.08	0.39	0.12	0.96	0.27
KR08	1.38	0.69	0.30	1.08	0.39
KR10	1.20	0.51	0.17	1.03	0.34
KR14	1.02	0.33	0.08	0.94	0.25
KR22	1.31	0.62	0.22	1.09	0.40
KR27	0.85	0.16	0.10	0.75	0.06
KR28	1.26	0.57	0.70	0.57	0.12

2.4.4 Pathway simulations (PA01)

The PA01 simulations required to identify pathways from release points (see Table 2-1), using the boundary conditions specified for simulation SS01 and without any open borehole in the domain. A first computation of these pathways was based on the particle tracking capabilities of Tecplot. The particle tracking simulations were verified by conducting an advective-dispersive transport simulation with the model, where a solute source was specified at the release points. This advective-dispersive simulation only served to verify that the trajectories calculated with Tecplot agreed with the solute migration simulated by the model.

In addition to particle tracking, another attempt at identifying pathways and travel times was based on the model capabilities to simulate life expectancy for the release points, which is the time taken by fluid particles originating from release points to reach an outflow boundary of the model. For these simulations, the simulations are run in a backward-in-time mode, which consists in reversing the flow field. A life expectancy of zero is assigned at the outflow boundaries and a backward-in-time simulation is then run to compute the mean life expectancy for every node in the domain. In addition to the mean life expectancy, the model also computes the probability density function and the cumulative density function of life expectancy at every node.

Both the advective-dispersive and the mean life expectancy transport simulations require dispersive parameters for the porous matrix and the hydraulic zones. These parameters have not been measured and the values that were assumed are shown in Table 2-9. Molecular diffusion is also simulated in the model, with an effective molecular diffusion coefficient assumed equal to $8.64 \cdot 10^{-6}$ m^2/day.

The trajectories computed by Tecplot are shown in Figure 2-20. The particles travel towards the south and exit the domain at the southern boundary. Although it is not clearly seen in the Figure, Tecplot predicts that particles travel faster from release point 1, which is located in zone HZ19C. Tecplot also predicts that travel from release point 3 (HZ20B_ALT) is very limited and particles released from that point do not reach the southern boundary.

Table 2-8. Coordinates of the release points in the model.

Release point	Coordinates x,y,z (m)	Hydraulic zone
1	(1525922.0, 6791993.0, −112.0)	HZ19C
2	(1525922.0, 6791993.0, −300.0)	HZ20A
3	(1525922.0, 6791993.0, −380.0)	HZ20B_ALT

Table 2-9. Transport properties.

Domain	Porosity	Longitudinal dispersivity (m)	Transverse dispersivity (m)
Hydraulic zones	1.0	5.0	0.5
Rock matrix	0.0025	1.0	1.0

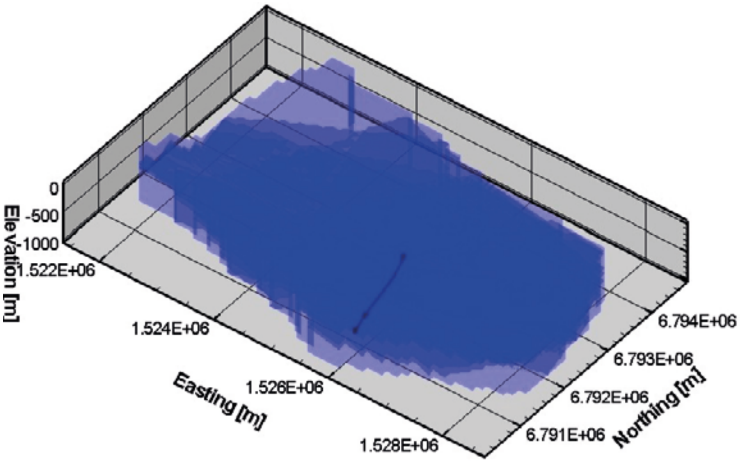

Figure 2-20. Trajectories of particles from release points, computed by Tecplot. The traces of the domain boundaries and hydraulic zones are shown in translucent colour.

To verify the Tecplot trajectories, an advective-dispersive simulation was conducted with the SS01 flow field. The initial solute concentration was zero everywhere in the domain. The nodes corresponding to the location of borehole KR24 were assigned a constant solute concentration equal to zero, all inflow boundaries were assigned a third-type boundary conditions with the concentration of incoming fluid equal to zero, and the solute was allowed to freely advect out of the domain at the outflow boundaries. The computed solute concentrations (Figure 2-21) show a trajectory similar to that predicted by Tecplot, towards the south. These simulations also show preferential transport along HZ19C and HZ20A (the two "parts" of the plume in the Figure correspond to these two zones) and limited transport along HZ20B_ALT.

The life expectancy statistics are shown in Figure 2-22 and Figure 2-23. The probability density function (Figure 2-22) shows that the life expectancy for fluid particles released at the KR24 location can be computed as a random variable. The life expectancy computations agree with particle tracking and show that the life expectancy is the shortest for release point 1 (HZ19C) and the longest for release point 3 (HZ20B_ALT). For HZ19C, the probability density function rapidly increases and reaches a peak at about 4000 days (about 12 years), after which it gradually decreases. For release point 2 (HZ20A), the probability of a particle reaching an outflow boundary is negligible until about 3000 days, and it reaches a maximum value at about 10 000 days. The probability density function for the last release point (HZ20B_ALT) remains very small for the simulation time considered (less than 55 000 days).

The cumulative density function Figure 2-23 is obtained by integration of the probability density function. After 55 000 days, there is a probability of about 70% that a fluid particle originating at release point 1 will have reached an outflow boundary. The probability is less for the other 2 points, with the probability for release point 3 being about 2%. This very low probability reflects the travel path from release point 3, which is mainly in the very low hydraulic conductivity rock matrix, where solute transport is very slow and controlled by diffusion.

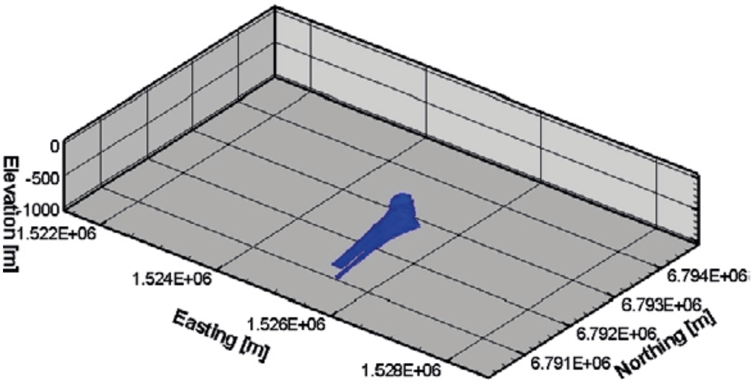

Figure 2-21. Relative concentration equal to 0.001 at a time of 30 years, for a solute source located at KR24.

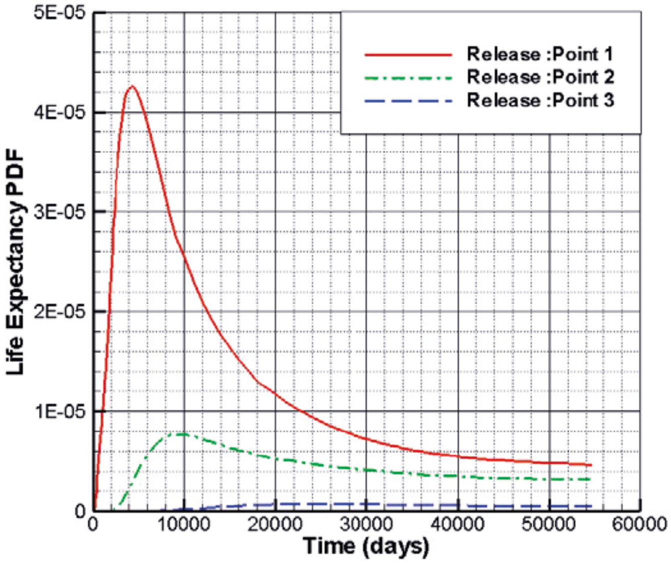

***Figure 2-22.** Probability density function for life expectancy, computed at the release points.*

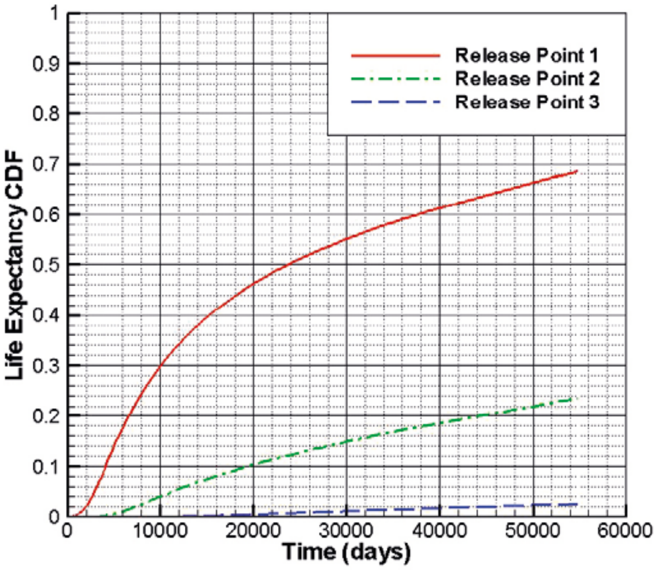

***Figure 2-23.** Cumulative density function for life expectancy, computed at the release points.*

2.5 Inverse modelling

Inverse modelling was a part of subtask 7A1 with the objective of better fitting the model to observed hydraulic heads and borehole inflows. Subtasks 7A4 and 7A5 are closely linked to 7A1 since a better model obtained in 7A1 could be used to answer questions related to compartmentalization and performance assessment.

Inverse modelling was attempted to improve the model, either manually or automatically, but none of these attempted produced a significantly better match of hydraulic heads, and results from these attempts are therefore not presented. During the calibration attempts, the flow rates were also investigated but simulated flow rates proved to be much more variable compared to observed flow rates, than simulated hydraulic heads compared to observed ones. It suggests that calibrating to flow rates is more challenging than calibrating to hydraulic heads.

During manual inverse modelling, parameters changed were the transmissivities of entire zones. Transmissivity values that were tested for each individual zone were taken in the interval between the mean transmissivity plus or minus one standard deviation. Attempts were not made to locally modify the zone transmissivity, for example by specifying local values in the vicinity of boreholes.

Automated inverse modelling for SS02 was also attempted with the PEST software (Doherty 2004). Using PEST required developing a simplified interface to allow PEST to drive the HydroGeoSphere simulations and modify the HydroGeoSphere input files during calibration. The adjustable parameters allowed to vary in the model were the aperture of individual hydraulic zones. During the PEST simulation, the initial guess for each adjustable parameter was the aperture derived from the mean transmissivity (Table 2-2) and the allowed interval was taken from the mean permeability plus or minus two standard deviations. Because the aperture values are small, the PEST option to take the log-transformed value of aperture was taken. The observations, or targets, were the observed hydraulic heads shown in Table 2-5. As a result, there were therefore 13 model parameters to vary and only 8 targets to reproduce.

During optimization, PEST tries to minimize the sum of squared residuals, with the residual being the difference between an observation (target) and the simulated value. Using default values for most PEST input parameters, PEST could not significantly lower the sum of squared residuals, even if a very large number of model runs were tried (over 100 model runs). A message issued by PEST during optimization was that the majority of adjustment parameters (apertures) had no effect on observations (target), which seem to prevent a significant reduction in the sum of squared residuals. Such a problem is cited in Doherty (2004) but without a definite reason as to the reason for this type of message.

The PEST simulations were preliminary and a better knowledge of the PEST capabilities would help get better results, since PEST contains several options designed to improve calibration. Doherty (2004) writes that "*The fact that PEST provides so many control variables by which it can be "tuned" to a particular model is one of the cornerstones of its model-independence*." The very large number of control parameters also requires that significant time be spent learning to use PEST efficiently and understand the effect of these control parameters.

2.6 Discussion and Conclusions

2.6.1 Assessment of influence of boreholes

Open boreholes increase the global hydraulic conductivity of the rock mass and create connections between hydraulic zones. As a result, they tend to decrease the hydraulic head gradients in the groundwater flow system. Simulations suggest that open boreholes reduce the spread of hydraulic heads among all observation points. They also reduce the drop in hydraulic head with depth.

2.6.2 Assessment of usefulness of PFL data

The flow rates measured with the PFL were not used extensively for the Task 7A work presented here. One reason is that the PFL give very detailed flow measurements and that a prior interpretation of these measurements is required before trying to efficiently simulate them, along with a sufficient understanding of the flow system. Such detailed interpretation and understanding require time and effort and are probably outside the scope of the task. In addition, a well-calibrated model is probably required to make full use of the flow measurements. Although it was not tested in Task 7a, calibration of a model to both hydraulic heads and PFL flow rates would certainly improve confidence in the model. Model calibration to both hydraulic heads and PFL flow rates was done for Task 7B, which is presented later in this report.

In the context of Task 7, generic models for a simplified system could perhaps provide additional insight into the usefulness of PFL data, for example by showing how flow rates change depending on boundary conditions, properties of hydraulic zones and connectivity created by open boreholes. Examples of such simplified systems are the simulations conducted at the beginning of Task 7 and presented at the first workshop in 2005 (Vidstrand et al. 2015).

2.6.3 New developments

The task force allowed the verification of the model capabilities for simulating fluid flow into discrete hydraulic zones and open boreholes, as well as computing inflows in and out of boreholes. In addition, a methodology was developed for discretizing irregular fractures into a regular 3D mesh (Graf and Therrien 2008). One advantage of the method is that there is no need to design a complex 3D mesh with, for example, tetrahedral elements, which is often time-consuming and a major part of the modelling effort. Improvements are however needed to provide a better representation of all recorded intersections between fractures and boreholes, perhaps by conditioning the mesh generation to ensure that nodes are located at these intersections.

Although the method proved useful and efficient, the representation of the intersection between fracture zones and boreholes in the model did not always coincide with the observations. One reason is that a staircase approach is taken to discretize the 2D hydraulic zones and the 1D open boreholes, such that the mesh has an effect on the exact location of the intersection. For a system where the hydraulic zones and the boreholes conduct the majority of the flow, it seems that capturing the intersections is more important than capturing their exact location. The current model did capture the intersections and connectivity of the hydraulic zones and borehole network properly, but there were some observed intersections that were not reproduced accurately with the mesh.

2.6.4 Some remaining issues

Calibration was not successful but there were perhaps some questions related to the level of calibration to reach. For example, modification of local hydraulic properties, near boreholes, could be used to fine tune calibration and improve the match to heads and flowrates, but it might be difficult to conclude if the better match is the result of local fine-tuning or the result of a better representation of the system.

Another difficulty in calibrating the model for Task 7A is that the base model provided for the Task, and the data available, were selected to simplify the representation of the groundwater system and avoid the need for the modelling teams to design their own site model using all available data. Some simplifications concern the boundary conditions and the properties of the upper part of the rock matrix. These simplifications probably had an impact on simulated hydraulic heads and therefore influenced the success of calibration.

3 Task 7B

3.1 Introduction

This section concerns work conducted during Task 7B, whose aim is to understand the fluid flow and response to hydraulic perturbations at the block scale. While Task 7A considered a region of approximately 10 km^2 in the vicinity of borehole KR24 at the Olkiluoto site, Task 7B considers a smaller volume of approximately 500 m surrounding the group of KR14–18 boreholes.

The objectives of Task 7B, presented in Vidstrand et al. (2015), are to quantify the reduction of uncertainty in the properties of the fracture network and to assess the Posiva Flow Log (PFL) data when analyzing the fractured rock. The approach chosen here is to use transmissivity profiles obtained from the Posiva Flow Log and double-packer testing (with Posiva's HTU-tool) to create a statistical description of conductive fractures along the boreholes. The performance of the groundwater system and its response to different interference pumping in the presence of open and sealed-off boreholes are then simulated. The sensitivity of the hydraulic parameters used for the numerical groundwater flow model developed for the KR14–18 region of the Olkiluoto site is also tested by adapting the conceptual model during the task.

Task 7B is divided into subtasks 7B1 and 7B2. The specific goal of subtask 7B1 is to develop a conceptual model for the fractured rock at the scale of the block considered here. A geostatistical approach characterized by a transitional probability model based on Markov chains (Carle 1999) has been adopted to represent the fractured rock at that scale. The fractures identified in borehole cores with the PFL technique are used to define the vertical transition probability of fractured rock facies.

Subtask 7B2 consists of a series of forward and inverse numerical simulations, based on the conceptual model developed within Task 7B1. The objective of these simulations is to gradually improve the conceptual model and background fracture representations by accounting for the uncertainties in the hydrostructural model rather than arbitrarily adjust parameters, such as fracture skin, to better reproduce the observations and calibrate the model. Subtask 7B2 is thus conducted according to the task description, which states that justification for the conceptual model and simulation approach should be provided independently of the calibration method used (Vidstrand et al. 2015).

The modelling tools used for Task7B are HydroGeoSphere, a numerical code for subsurface groundwater simulations (Therrien et al. 2009), T-PROGS, a geostatistical transition probability geostatistical software (Carle 1999), and PEST, a model-independent parameter estimation (Doherty 2004).

3.2 Site Description

The area around boreholes KR14–18 and KR15B–18B, shown by the red circle in Figure 3-1, is located in the centre of Olkiluoto Island and covers approximately 500 m by 500 m. Boreholes KR14, KR15, KR16, KR17, and KR18 are deep A-boreholes, whose lengths range from 130 to 515 meters. The B-boreholes KR15B, KR16B, KR17B, and KR18B are shallow boreholes drilled near the corresponding deep boreholes. B-boreholes have a length of 45 meters.

The casing pipes have different lengths in these boreholes. The casing installed in borehole KR14 is 10 m long, while those installed in other deep boreholes KR15–KR18 have a length of 40 m. The longer well casing for boreholes KR15–KR18 is explained by the presence of shallow B-boreholes in their vicinity. The hydraulic heads in the uppermost portion of the domain are thus measured in the shallow boreholes, while the deep boreholes register the hydraulic response in the deeper bedrock.

3.2.1 Hydraulic tests in the KR14–KR18 boreholes

Vidstrand et al. (2015) present a brief description of two series of hydraulic tests conducted in the KR14–KR18 boreholes, which have generated drawdown and flow measurements that are the focus of Task 7B.

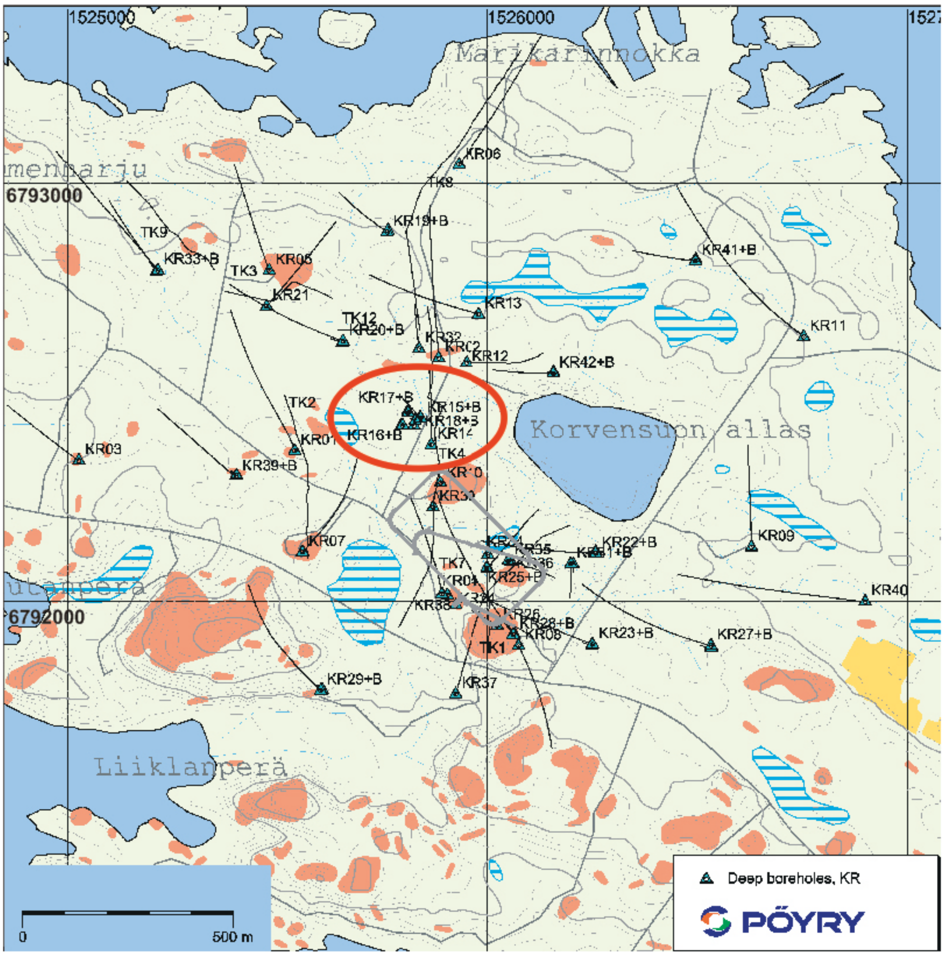

Figure 3-1. *Location of the KR14–KR18 boreholes on Olkiluoto Island.*

The first series of interference tests was conducted in boreholes KR14–KR18 and KR15B–KR18B between December 2001 and April 2002 (Rouhiainen and Pöllänen 2003). All flow and drawdown measurements were conducted in open boreholes. In a first step, single hole tests were conducted in every borehole during which flow rates and drawdown were measured along 2-m sections, with and without pumping the borehole being tested. In the second step, interference tests were conducted where each borehole was pumped in turn and the head response (drawdown) and flow response (flow rates in the test sections) were measured in the other boreholes. The same depth intervals were used both for the single hole tests and the interference tests. An example of the hydraulic head measured during one of the interference tests is shown in Figure 3-2.

The second series of tests was conducted in 2004 and, in contrast to the first series described above, boreholes were packed off and pressure responses were measured in the packed-off intervals. Those pressure response tests were conducted in 4 phases (Vidstrand et al. 2015):

1. Phase 1: Pumping of open borehole KR14 between September 14 and September 21, 2004, and monitoring of pressure changes in surrounding packed-off intervals.
2. Phase 2: Pumping of open borehole KR18 between September 29 and October 6, 2004, and monitoring of pressure changes in surrounding packed-off intervals.
3. Phase 3: Injection of water, using the HTU (Hydraulic Testing Unit) for selected packed-off intervals in KR18, and monitoring of pressure changes in surrounding packed-off intervals.
4. Phase 4: Injection of water, using the HTU (Hydraulic Testing Unit) for packed-off intervals in KR18 different than those used in Phase 3, and monitoring of pressure changes in surrounding packed-off intervals.

An example of the pressure responses measured during these interference tests is shown in Figure 3-3.

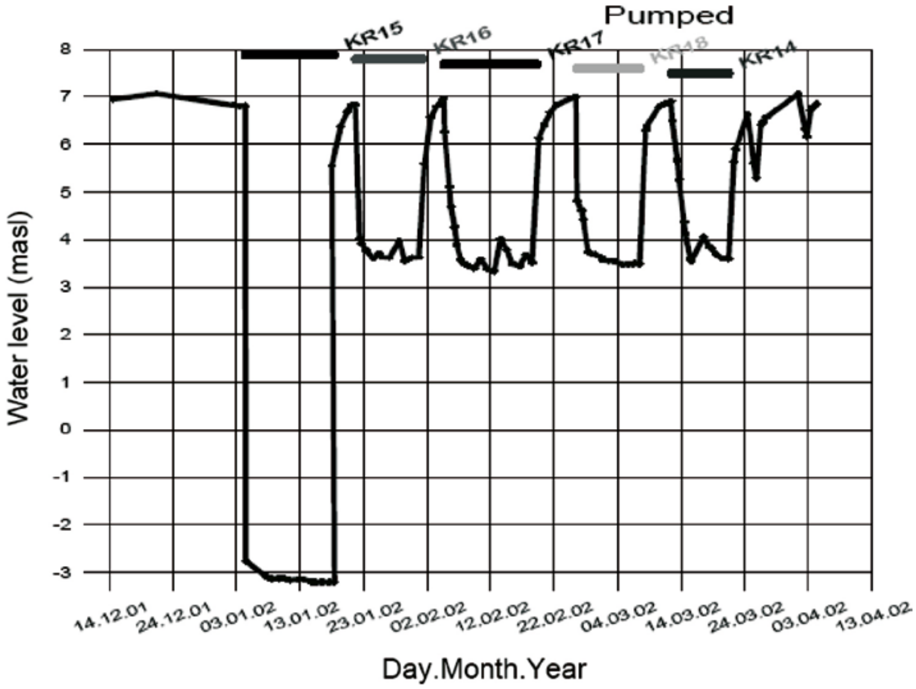

Figure 3-2. *Water level measured in borehole KR15 during the interference tests with open boreholes. The borehole being pumped is indicated at the top of the figure (figure taken from Rouhiainen and Pöllänen 2003).*

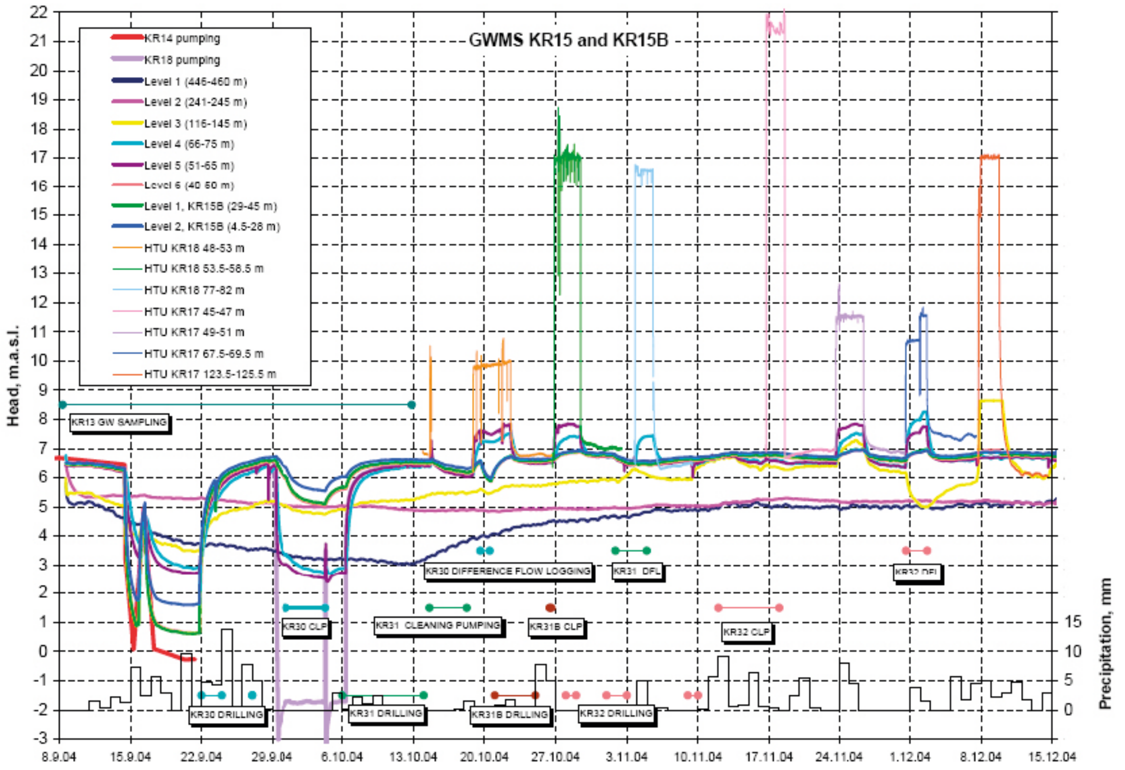

Figure 3-3. *Illustration of results of the KR14–18 pressure interference tests conducted in 2004 (from Vidstrand et al. 2015)*

3.3 Hydrogeological modelling

3.3.1 HydroGeoSphere

The simulations described in this report have been conducted with HydroGeoSphere (Therrien et al. 2009), which is a numerical simulator specifically developed for supporting water resource and engineering projects pertaining to hydrologic systems with surface and subsurface flow and contaminant transport components. The governing equations for subsurface groundwater flow and solute transport are solved with the Control Volume-Finite Element (CVFE) method. A finite element mesh is used to discretize the simulation domain, while a dual mesh is used to define control volumes around mesh nodes. Since the numerical method and the governing equations have been presented previously in the section describing Task 7A, no further details are provided here.

For Task 7B, HydroGeoSphere was used in conjunction with T-PROGS and PEST, two additional tools adopted here for the definition of the hydrostructural model and for inverse modelling, respectively. T-PROGS generates spatial geostatistical distributions of fractured rock facies based on observations of vertical and horizontal transition probabilities. These observations are obtained from PFL measurements and fracture density evaluation along core intervals. The facies distribution obtained with T-PROGS is then used to assign material properties in the simulation domain considered by HydroGeoSphere.

Automatic inverse modelling was attempted for Task 7A, but the limited knowledge of PEST capabilities affected the modelling results. Task7B simulation scenarios are well suited to better exploit the PEST inverse modelling technique. Moreover, a PEST-HydroGeoSphere interface has been developed to calibrate the model with both head and flow observations. It is more difficult to obtain a good match between simulated and measured flows than between simulated and measured hydraulic heads, because of the large variation of flow values. However, since PFL measurements were available, they have been included in the inverse modelling process to observe their influence on model calibration.

3.3.2 T-PROGS

The Transition PRObability Geostatistical Software (T-PROGS) is a set of FORTRAN programs based on the transition probability/Markov approach for geostatistical analysis and simulation of spatial distributions of categorical variables, such as geological units and facies. T-PROGS involves three main steps: (a) calculating transition probabilities based on measurements, (b) modelling spatial variability with Markov chains, and (c) performing conditional simulation (Carle 1999). T-PROGS has been used here to generate fractured rock facies distributions in the area surrounding the KR14–KR18 boreholes.

The probability $t_{jk}(h_\phi)$ that there is a transition between geological facies j and k for two measurement locations separated by distance h_ϕ, which denotes a lag in the direction ϕ, is defined as:

$$t_{jk}\left(h_\phi\right) = \Pr\left\{k \text{ occurs at } x + h \middle| j \text{ occurs at } x\right\} \tag{3-1}$$

where x is a spatial location vector. Measurements of $t_{jk}(h_\phi)$ along boreholes reflect the spatial continuity and juxtapositional tendencies of geological facies, similar to a variogram for a continuous variable such as hydraulic conductivity or porosity.

A spatial Markov chain model is used to model the observed transitional probabilities, which are expressed along any direction as:

$$\mathbf{T}(h_\phi) = \exp\left[\mathbf{R}_\phi h_\phi\right] \tag{3-2}$$

where $\mathbf{T}(h_\phi)$ is a N × N matrix of transition probabilities, with N being the number of categories (or facies) to be considered and $\mathbf{R}_\phi$ the matrix of transition rates described by:

$$\mathbf{R}_\phi = \begin{bmatrix} r_{11,\phi} & \cdots & r_{1N,\phi} \\ \vdots & \ddots & \vdots \\ r_{N1,\phi} & \cdots & r_{NN,\phi} \end{bmatrix} \tag{3-3}$$

where entries $r_{jk,\phi}$ describe the rate of change from facies j to facies k per unit length in direction ϕ.

In order to fit a Markov chain model, Equation (3-1) is used to calculate observed transition probabilities along boreholes. Equation (3-2) is then used to fit the Markov chain model to the data by filling the transition rate matrix shown in Equation (3-3).

Fitting is straightforward when data are abundant and the transition rates are well defined, which is the case for continuous measurements along boreholes. When data are scarce and insufficient to infer obvious transition rates, geological information can be used to build the Markov chain model. Information such as mean facies length, volumetric proportions and juxtapositional tendencies can be used to build the Markov Chain model. For example, Carle and Fogg (1997) have shown that the sills of the transition probability plots reflect volumetric proportions p of the column categories and are related to transition probabilities by

$$p_k = \lim_{h_\phi \to \infty} t_{jk}\left(h_\phi\right) \quad \forall j,k \tag{3-4}$$

The volumetric proportions are obtained directly from the borehole analysis.

Geological information useful to build the Markov chain model include the mean length $\bar{L}_{k,\phi}$ of facies that have been related to the diagonal transition rate $r_{kk,\phi}$ by

$$r_{kk,\phi} = -\frac{1}{\bar{L}_{k,\phi}} \quad \forall j,k \tag{3-5}$$

as defined by Carle and Fogg (1997). With that method, estimates of the mean length can be incorporated in Equation (3-3) to establish the diagonal transition rates of the Markov chain model.

The last observation that can be used to build the Markov chain model and fill the off-diagonal terms in Equation (3-3) is the embedded transition probability. Embedded transition probability differs from spatial transition probability in that it defines the probability that one embedded or discrete facies is next or adjacent to another one in a given direction. In that case, auto-transition can't be observed. In addition, the transition from one facies to the other is used instead of lag distances. The embedded transition probability in the vertical direction is defined by:

$$\pi_{jk,\phi} = \Pr\{k \text{ occurs above } j \,|\, j \text{ below}\} \tag{3-6}$$

where k and j denote embedded occurrences. The off-diagonal transition rates in Equation (3-3) are related to embedded transition probabilities (Carle 1997b) by

$$r_{jk,\phi} = -\frac{\pi_{jk,\phi}}{L_{j,\phi}} \quad \text{for } j \neq k \tag{3-7}$$

A background facies can be defined by automatically fitting the transition rates, or embedded transition probabilities (see Carle 1999 for details). This further reduces the number of input parameters in the model.

3.3.3 PEST

PEST, which means Parameter ESTimation, is a nonlinear parameter estimator software used for automatic model calibration. Most models are nonlinear because simulated output variables, equivalent to observations, are nonlinearly related to parameters that are estimated. An example of nonlinearity is given by the relationship between hydraulic conductivity and hydraulic head. Darcy's law, written as

$$Q = -KA\frac{dh}{dx} \tag{3-8}$$

can be used to demonstrate this nonlinearly of hydraulic head h with respect to hydraulic conductivity K (Hill and Tiedeman 2007). Knowing the hydraulic head h_0 at a given location, Equation (3-8) can be solved to calculate the hydraulic head h at a distance x from the known location of h_0:

$$h = h_0 - \frac{Q}{KA}x$$

Using the result above, the derivative of hydraulic head with respect to the hydraulic conductivity is expressed by:

$$\frac{dh}{dK} = -\left(\frac{Q}{K^2 A}\right)x \tag{3-9}$$

The derivative *dh/dK* can be defined as the sensitivity in a parameter estimation problem for which *K* is estimated. Equation (3-9) shows that, since *dh/dK* is a function of *K*, the relationship between hydraulic head and hydraulic conductivity is non linear for a parameter estimation problem.

The non-linear relationship between model parameters and model-generated observations is linearized by formulating it as a Taylor expansion about the currently best parameter set at the beginning of each iteration (Doherty 2004). Therefore, the derivatives of all observations with respect to all parameters are calculated and the linearized problem is solved for a better parameter set.

PEST is based on the Gauss-Marquardt-Levenberg method of parameter estimation. A detailed description of the estimation process is found in Doherty (2004) and only some specific aspects are repeated here. Let us assume that a natural or man-made system can be described by the linear equation

$$Xb = c \tag{3-10}$$

where *X* is a [m×n] matrix. The elements of *X* are constant and hence independent of the elements of *b*, which holds the system parameters, while *c* is a vector of order *m* containing numbers that describe the system's response to a set of excitations embodied in matrix *X*, and for which we can obtain corresponding field or laboratory measurements by which to infer the system parameters comprising *b*.

A general non linear model can be expressed by:

$$c_0 = M(b_0) \tag{3-11}$$

Where b_0 contains the set of parameters and c_0 is the corresponding set of model-calculated observations generated using M. The linearized form of Equation (3-11) is obtained by the Taylor expansion. Thus, to generate a set of observations *c* corresponding to a parameter vector *b* that differs only slightly from b_0, Taylor's theorem states that the following relationship is approximately correct:

$$c = c_0 + J\,(b - b_0) \tag{3-12}$$

where *J* is the Jacobian matrix containing the derivatives of the observations with respect to each estimated parameter. The approximation improves with proximity of *b* to b_0. Matrix *J* has dimensions [*m*×*n*] and is given by

$$J = \begin{bmatrix} \dfrac{\partial h_i}{\partial K_j} & \cdots & \dfrac{\partial h_i}{\partial K_n} \\ \vdots & \ddots & \vdots \\ \dfrac{\partial h_m}{\partial K_j} & \cdots & \dfrac{\partial h_m}{\partial K_n} \end{bmatrix} \qquad i = 1, n \quad j = 1, m \tag{3-13}$$

where each column *j* contains the derivative of all *m* observations with respect to parameter *j*, while each row contains the derivative of observation *i* with respect to all *n* parameters involved in the estimation process.

The derivatives in the Jacobian matrix can be evaluated using either forward or central differences. The ability to calculate the derivatives of all observations with respect to all adjustable parameters is fundamental to the Gauss-Marquardt-Levenberg method of parameter estimation (Doherty 2004). Accuracy in derivatives calculation is fundamental to PEST's success in optimizing parameters, but it also represents the most time-consuming part of PEST's parameter estimation procedure.

The goal of calibration is to derive a set of model parameters for which the model generated observations are as close as possible to the set of experimental observations, in the least square sense. To achieve this goal, the following objective function is defined as:

$$\Phi = \left(c - c_0 - J\left(b - b_0\right)\right)^t Q\left(c - c_0 - J\left(b - b_0\right)\right) \tag{3-14}$$

Parameter estimation of nonlinear models is an iterative process based on the evaluation of weighted sum of squared differences between model generated observation values and those actually measured in the laboratory or field (Doherty 2004). In Equation (3-14), $(b{-}b_0)$ is the parameter upgrade vector, $(c{-}c_0)$ defines the discrepancy between the model-calculated observations c_0 and their experimental counterparts c, and Q is a m-dimensional square diagonal matrix whose i-th diagonal element is the square of the weight w_i associated to the i-th observation.

The vector b that minimizes the objective function is given by :

$$b = b_0 + u \tag{3-15}$$

and the parameter upgrade vector u can be also written using the Gauss-Newton formula as:

$$u = \left(J^t Q J\right)^{-1} J^t Q r \tag{3-16}$$

where r is the vector of residuals expressed above as $(c{-}c_0)$. For many problems, especially those involving different types of observations and parameters whose magnitude may vary greatly, the elements of J can be largely different in magnitude, causing round off errors when the upgrade vector is calculated (Doherty 2004). To overcome this problem, a scaling matrix S is introduced and Equation (3-16) becomes (see Doherty 2004 for details):

$$S^{-1} u = \left(\left(JS\right)^t QJS + \alpha S^t S\right)^{-1} \left(JS\right)^t Qr \tag{3-17}$$

where α is called Marquardt parameter, which is introduced to adjust the parameter upgrade vector to the direction of the gradient of the objective function. The largest element of $\alpha S^t S$ is denoted as lambda λ in Doherty (2004).

When interfaced with a model like HydroGeoSphere, PEST's role is to minimize Φ by adjusting parameter values and, thus, the parameter upgrade vector. By comparing parameter changes and objective function improvement during the current iteration with those from the previous iterations, PEST can tell whether it is worth undertaking another optimization iteration (Doherty 2004). To start the first optimisation iteration, the Levenberg-Marquardt algorithm requires that the user supply an initial value for the Marquardt lambda λ, which is used to adjust the direction of the parameter upgrade vector to that of the gradient of Φ. The Marquardt lambda corresponds to the Marquardt parameter α of the original problem before the introduction of the scaling matrix S. The first lambda that PEST employs in calculating the parameter upgrade vector during any optimization iteration is the lambda inherited from the previous iteration.

Correlation coefficient

The correlation coefficient should not be confused with the parameter correlation coefficients, which are given in the parameter coefficient matrix. The correlation coefficient R represents the fit of simulated values to observations. Ideally, simulated values should be as close as possible to observations such that weighted simulated values should align along a straight line with slope equal to 1 and an intercept of zero when plotted against weighted observed values.

The correlation coefficient is calculated as (Doherty 2004):

$$R = \frac{\sum\left(w_i c_i - m\right)\left(w_i c_{oi} - m_o\right)}{\left[\sum\left(w_i c_i - m\right)\left(w_i c_i - m\right)\sum\left(w_i c_{oi} - m_o\right)\left(w_i c_{oi} - m_o\right)\right]^{0.5}} \tag{3-18}$$

where:

c_i is the i^{th} observation value,

c_{oi} is the model-generated value corresponding to observation c_i,

m is the mean value of weighted observations,

m_o is the mean value of weighted observations,

w_i is the weight associated with the i^{th} observation.

A value of R above 0.9 generally indicates that the trends in the simulated values closely match the observed values. However, this coefficient depends on the range of values for the observations, which may be large if different types of observations are considered, such as hydraulic heads and volumetric flow. Therefore, the interpretation of R should be done cautiously (Hill and Tiedeman 2007).

Residuals are defined as the difference between measured and simulated values, which are hydraulic head values or flow values in the context of Task 7B. Measured values are sometimes referred to as observations and therefore, in this report, the terms observed values and measured values are used interchangeably. Plotting weighted residuals versus weighted simulated values provides a better test of model bias than plotting weighted observations versus weighted simulated values. The reason is that the typically large range in magnitude of the observations and simulated values can obscure trends in the differences between them. This limitation is eliminated when weighted residuals are considered instead (Hill and Tiedeman 2007).

Parameter correlation coefficient

The parameter correlation coefficients (*pcc*) are evaluated for each pair of parameters to be estimated. Their values may vary from −1.0 to 1.0. The parameter correlation coefficients are given in the parameter correlation matrix, where a diagonal element pcc_{ii} represents the auto-correlation for parameter *i* and is therefore equal to 1.0, which represents perfect correlation, while the off-diagonal elements pcc_{ij} represent the correlation between parameter in row *i* with parameter in column *j*. Extreme correlation between parameters is indicated by an off-diagonal element near 1.0 or −1.0. Extreme correlation also signifies, in general, that the parameters cannot be estimated uniquely. But this non unique estimation conclusion is a rule of thumb, since experience in calibration shows that unique estimates can be also obtained with *pcc* near unity (Hill and Tiedeman 2007).

Confidence intervals

Individual confidence intervals are generally used to evaluate uncertainty in parameter estimates. A linear interval for parameter b_j is calculated as (Hill and Tiedeman 2007):

$$b_j \pm t\left(n, 1-\frac{\alpha}{2}\right)s_{b_j} \qquad (3\text{-}19)$$

where $t(n,1–\alpha/2)$ is the Student t-statistics for n degrees of freedom and a significance level α (which is commonly 5% or 10%), while s_{b_j} is the standard deviation of the b_j parameter. The degrees of freedom are equal to:

$$n = ND+NPR–NP \qquad (3\text{-}20)$$

where:

NP: number of estimated parameters.

NPR: number of prior information.

ND: number of observations.

The intervals can be confidence or prediction intervals, where the latter is needed if the interval is to be compared to a measurement because prediction intervals include the effects of the measurement error. The intervals can also be individual or simultaneous, where the latter is needed if the probability of two or more events is of interest. Finally, the intervals can be linear or nonlinear, depending on whether simple linear theory is used to produce the intervals or the nonlinearity of the groundwater flow equation is considered (Hill 2004).

More accurate nonlinear confidence intervals can be calculated using inferential statistics or Monte Carlo methods (Hill and Tiedeman 2007). Vecchia and Cooley (1987a) developed inferential methods to compute nonlinear confidence intervals on any function of the model parameters. Unlike a linear interval, a nonlinear interval is generally not symmetric about the optimal value. However, they are computationally expensive and they are usually calculated only for selected quantities of interest (Hill and Tiedeman 2007). For example, they are generally evaluated for model prediction only and not for model parameters.

Estimates of parameters and dependent variables from a calibrated groundwater model are generally uncertain because the data used for calibration are uncertain and because the model never perfectly represents the system or exactly fits the data. Confidence intervals on the estimated model parameters can be used to express the degree of uncertainty of these quantities, but this calculation is not straightforward because the solution of the groundwater flow equation for hydraulic heads, and quantities such as flows that are a function of hydraulic heads, is generally a nonlinear function of the model parameters (Christensen and Cooley 1999).

If PEST is run in estimation mode, the confidence intervals are linear. As mentioned by Christensen and Cooley (1999), the nonlinear regression model can be linearized using Taylor series, which is the method adopted in PEST. Parameter confidence limits are calculated on the basis on the same linearity assumption used to derive the equations for parameters improvement implemented in each PEST optimisation iteration. In fact, for each iteration, the relationship between model-parameter and model-generated observations is linearized by formulating it as a Taylor expansion. Remarkable differences are observed in interval width depending on the use of prior information as an additional observation group. The inclusion of prior information, being mathematically equivalent to taking extra measurements, may alter the numerical predominance of parameters over observations and thus provide the system with the ability to supply a unique set of parameter estimates.

Observation and parameter sensitivities

The composite observation sensitivity of observation o_j is defined as (Doherty 2004):

$$s_j = \left(QJJ^T\right)_{i,j}^{1/2} / n \qquad (3\text{-}21)$$

The composite sensitivity of observation *j* is calculated as the magnitude of the *jth* row of the Jacobian matrix multiplied by the weight associated with that observation. Then, this magnitude is divided by *n*, which is the number of adjustable parameters. It is thus a measure of the sensitivity of that observation to all parameters involved in the parameter estimation process.

The composite sensitivity of a parameter *i* is defined as the magnitude of the vector comprising the column of the Jacobian matrix *J* pertaining to that parameter divided by the number of observations (Doherty 2004):

$$s_i = \left(J^T QJ\right)_{ii}^{1/2} / m \qquad (3\text{-}22)$$

where *m* is the number of observations with non-zero weight. The relative composite sensitivity of a parameter is obtained by multiplying its composite sensitivity by the magnitude of the value of the parameter. It gives a measure of the composite changes in model outputs that are incurred by a fractional change in the value of the parameter (Doherty 2004). Composite parameter sensitivities allow for the identification of those parameters that may be degrading the performance of the estimation process because of their lack of sensitivity to model outcomes.

PEST control parameters

PEST control file can be modified by the user to change default values of control parameters. The parameters that were modified to improve the calibration process were AUIRESTITN, RLAMBA1, RLAMFAC, and AUIPHIRATACCEPT. They are explained in detail in Doherty (2004) and only a short description is provided here:

- AUIRESTITN: this parameter is used to give the Automatic User Intervention (AUI) a « rest » every now and then. This allows parameters that are repeatedly held on the basis of their insensitivity to undergo some adjustment. A value of 3 is considered, such that the AUI is paused every third iteration.
- RLAMBDA1: this real variable is the initial Marquardt lambda. PEST attempts parameter improvement using a number of different Marquardt lambdas during any given optimization iteration. During parameter estimation, the Marquardt lambda generally gets smaller. An initial value of 1.0 to 10.0 is appropriate for most models. High Marquardt lambda values can cause optimization to be inefficient and slow, but they often help in getting optimization started, especially if initial parameter estimates are poor (Doherty 2004). A value of 7 is adopted here.
- RLAMFAC: this real variable is the factor by which the Marquardt lambda is adjusted. It must be greater than 1.0. PEST reduces lambda by dividing it RLAMFAC; when it increases lambda it multiplies it by RLAMFAC. A value of 2 is chosen here.

- AUIPHIRATACCEPT: During every optimization iteration PEST first calculates an upgraded parameter set with no parameters held at their current values. The resulting objective function is then the "current objective function". If PEST decides to undertake one or several AUI iterations, it will not accept the parameter values calculated during those iterations unless the objective function falls below the fraction AUIPHIRATACCEPT of the current objective function. If it does fall below this value, however, the new objective function then becomes the "current objective function". A value of 0.9 is adopted here.
- NPRIOR: if prior information is included in the estimation process, the value of NPRIOR, which is zero by default, must be modified. The value equal to the number of prior information considered must be attributed to the NPRIOR parameter. It is important to observe that the use of logarithmically-transformed parameters requires that the prior information relations be adjusted accordingly. For example, if a logarithmic transformation is considered, the sum or the difference of two or more parameters becomes a product or a quotient, respectively.

3.4 Hydrostructural model

The coordinates of the area corresponding to the simulation domain extends between 6 792 300 m and 6 792 700 m along the north-south direction, and between 1 525 850 m and 1 526 050 m along the east-west direction. The lateral extent of the domain is therefore 400 m by 400 m and boreholes KR14–KR18 are located at its centre. Along the vertical direction, the domain extends from ground surface to a depth of 200 m. The bottom boundary is chosen to correspond approximately to fracture HZ20A, which lies at a depth of about −200 m in this area (Figure 3-4).

The lengths of the boreholes considered for the simulations are 45 m for the shallow B-boreholes and 515 m for deep boreholes KR14 and KR15. In the model, however, these two deep boreholes are truncated at a depth of −200 m a.s.l. which is the bottom boundary of the simulation domain.

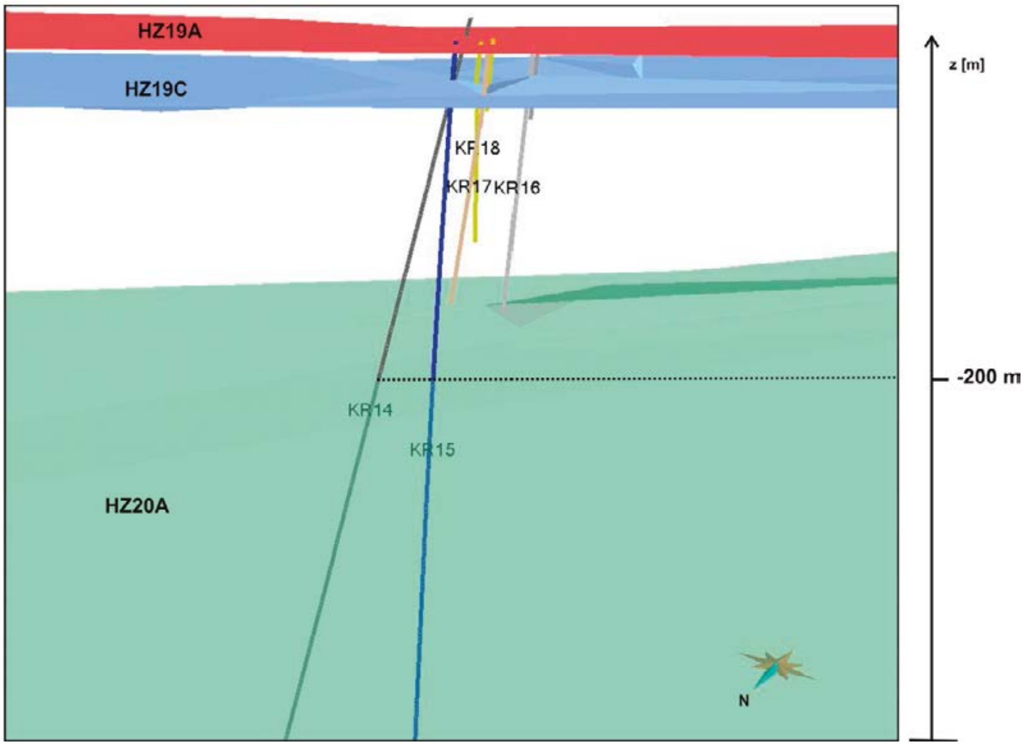

Figure 3-4. Vertical cross-section of the KR14–18 area, showing fracture zones HZ19A, HZ19C and HZ20A and boreholes. The bottom of the simulation is located at the elevation −200 m.

In addition to HZ20A, two other major fracture zones considered in Task7A, HZ19A and HZ19C, intersect the simulation domain. On the basis of the geometry defined in Task 7A, HZ19A and HZ19C are the zones closest to ground surface. These zones are not represented as discrete fractures in the model but it was rather decided to use a flat top boundary and to interpolate water table elevations on that boundary. Some discrete fractures can potentially be added during the simulations to improve adjustment of simulated results to observations. The decision not to explicitly represent HZ19A and HZ19C was motivated by the representation of the fractured rock by a spatial transitional probability of facies instead of a classical discrete fracture network (DFN) approach, assuming that these fracture zones can be accounted for by representing them as facies of higher hydraulic conductivity. Moreover, because of the uncertainty in the identification and characterization of fractures near ground surface, a flat top domain with an interpolated water-table is considered a better option.

3.4.1 Geostatistical approach

In fractured igneous and metamorphic rocks, groundwater flows primarily in hydraulically-active fractures. Depending on the distribution of fractures in the rock mass, the spatial distribution of hydraulic conductivity and groundwater fluxes can be very heterogeneous and exhibit sharp spatial transitions due to the discrete nature of the fractures. While this heterogeneity could be well captured by DFN models, fracture length and connectivity data are often scarce to build such model.

Equivalent porous medium (EPM) models have been used as an alternative to DFN models by developing relationships between discrete fracture properties and equivalent porous media properties. EPM models are usually built from the spatial variation of a property, such as hydraulic conductivity, for example by using variogram models, followed by interpolation using methods such as kriging. While this approach seems to yield realistic models for continuous variables, it fails to capture the sharp variation of hydraulic conductivity observed in fractured rocks. Indicator or categorical geostatistics using categorical classifications have been proposed to overcome this drawback (see for example Goovaerts 1996), but it requires an extensive number of field observations to yield realistic models. Another disadvantage is that, for cases where data is scarce, other geological observations cannot be used to improve the model.

An alternate and promising approach used by Park et al. (2004) in fractured rock environments relies on transition probability and Markov chain geostatistics to create a three dimensional model of categorical facies (Carle and Fogg 1997). As in categorical geostatistics, this approach relies on the definition of facies but differs in that the model is based on observed transition probabilities of the facies. EPM facies used here, and described in a later section, represent different levels of fracture intensity for which hydraulic conductivity and specific storage values are assigned.

Markov chain models can be fitted to observed transitional probabilities but they have the advantage that they can be constructed from other observed properties such as volumetric facies proportions, mean facies length and estimate of juxtaposition tendencies (Weissmann et al. 1999). While observed transitional probabilities are well defined along boreholes, it is usually not the case in other directions. Knowledge of volumetric proportions and mean facies length obtained from other observation sources, both quantitative and qualitative, can be used to create a geologically tenable model when the data are sparse (Weissmann et al. 1999).

3.4.2 Background fractures

Although Task 7B focuses on a block scale around boreholes KR14 to KR18, surrounding boreholes were also used in the analysis to increase the number of fracture observations in the geostatistical analysis. The list of boreholes used in the analysis is given in Appendix A (Table A-1) along with their relevant attributes. This analysis focuses on background fractures only, without including fractures that are assumed to belong to fracture zones such as HZ19A, HZ19C and HZ20A and that were identified by Posiva Oy in Data Delivery 29. Fractures zones are deterministically represented in the model using continuous discrete fractures across the domain. Background fractures in the study area are sub-horizontal, as shown in the stereographic projection of fracture poles in Figure 3-5. The distribution of fracture poles suggests that these fractures belong to a single set, with a mean orientation of 301N with a dip of 9°. Background fractures are assumed to have a limited extent because they could not be traced from one borehole to another.

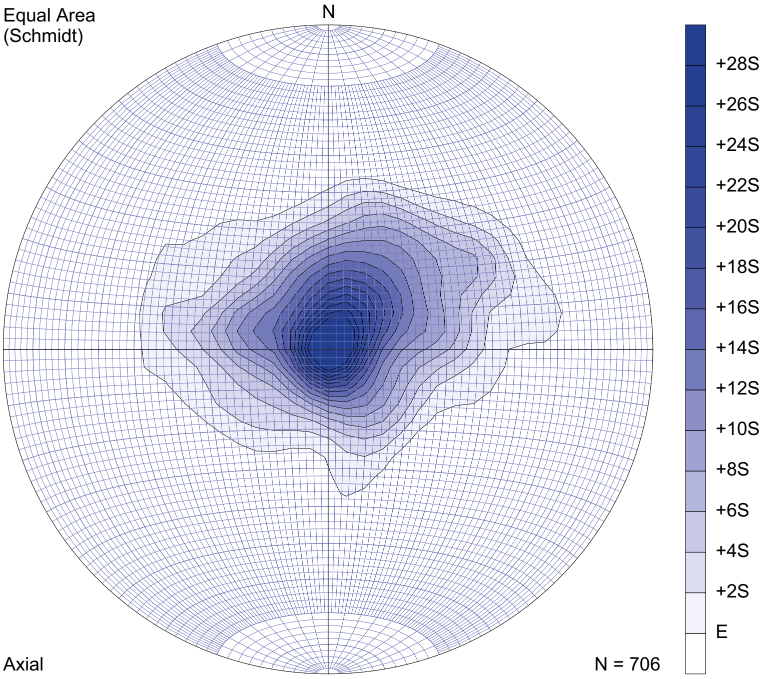

***Figure 3-5.** Schmidt equal-area stereographic projection of background fractures poles (strike/dip).*

Hydraulic properties of single fractures were measured in every borehole with the Posiva Oy flow logging (PFL) tool. Unlike traditional borehole flowmeters, which measure the total cumulative flow rate along a borehole, the PFL DIFF measures the flow rate into or out of specific borehole sections. The advantage is improved detection of incremental flow changes along a borehole. Flow changes are generally very small and they can easily be missed with conventional flowmeters (Väisäsvaara et al. 2008).

The PFL tool can distinguish between conductive and non-conductive fractures. For conductive fractures (i.e. those that are above the detection limit of the PFL tool), a fracture transmissivity value is obtained. In the following analysis, only fractures with a measured transmissivity value are considered. Figure 3-6 shows the histogram of measured fracture transmissivities for all conductive fractures identified with the PFL tool in the boreholes listed in Table A-1 in Appendix A.

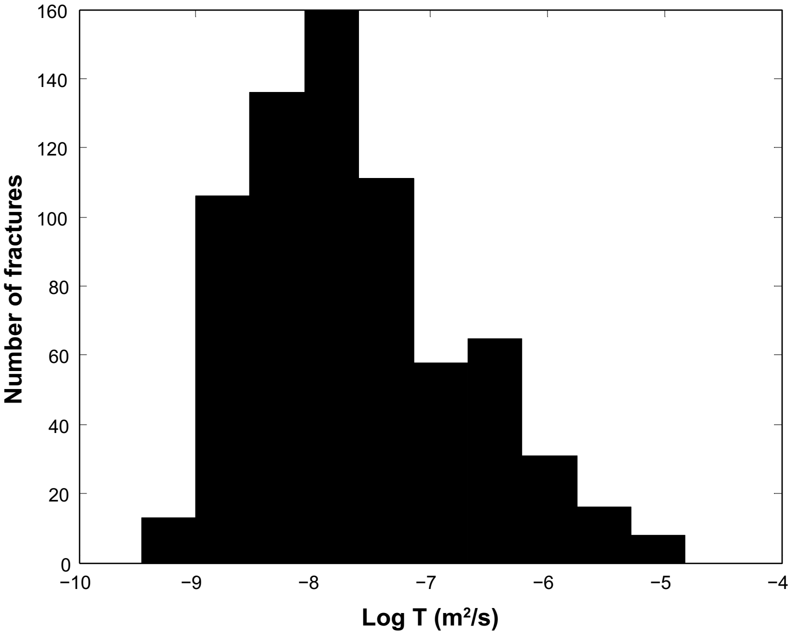

***Figure 3-6.** Histogram of background fractures transmissivity as measured with the Posiva Oy flow logging tool.*

3.4.3 Fractured rock classification

Several relationships have been found and/or proposed between individual fracture hydraulic properties and other fracture attributes such as length (Dershowitz et al. 2003a), depth (Ingebritsen and Manning 1999), strike and density (Park et al. 2004). At the Olkiluoto site, there is little information on the length of background fractures such that a relationship between transmissivity and fracture length cannot be established. Fracture transmissivities versus depth are plotted in Figure 3-7. One could assume a decrease of transmissivity versus depth over the borehole length range, but at the scale of the modelled block, the difference in transmissivity with depth is likely insignificant. Moreover, this relationship provides no information on the lateral distribution of the fracture properties.

Another option is to relate EPM hydraulic conductivity to fracture density in the rock mass, which is the approach taken here. There is seldom a definite correlation between fracture density and transmissivity in fractured rock environments because some fractures are non-transmissive and others are highly transmissive. To overcome this common lack of correlation, we only consider the transmissive fractures in the rock mass such that only the fractures observed in the boreholes for which a transmissivity value has been measured are used for the analysis.

The number of transmissive fractures per interval has been calculated and the fracture density was then evaluated. The transmissivity T_i of interval i along the boreholes is obtained by summing the transmissivity T_k of individual fractures k within the interval (Figure 3-8) using:

$$T_i = \sum_{k=1}^{n} T_k \tag{3-23}$$

where n is the number of fractures in interval i. The transmissivity of the interval is then converted to hydraulic conductivity by dividing the transmissivity of the interval T_i by the interval length Δl:

$$K_i = \frac{T_i}{\Delta l} \tag{3-24}$$

The selected interval length Δl for calculating fracture density along the considered boreholes is 5 m. Since the objective is to provide a representation of the background fractured rock, major fracture zones are neglected, as mentioned in Section 4.2.

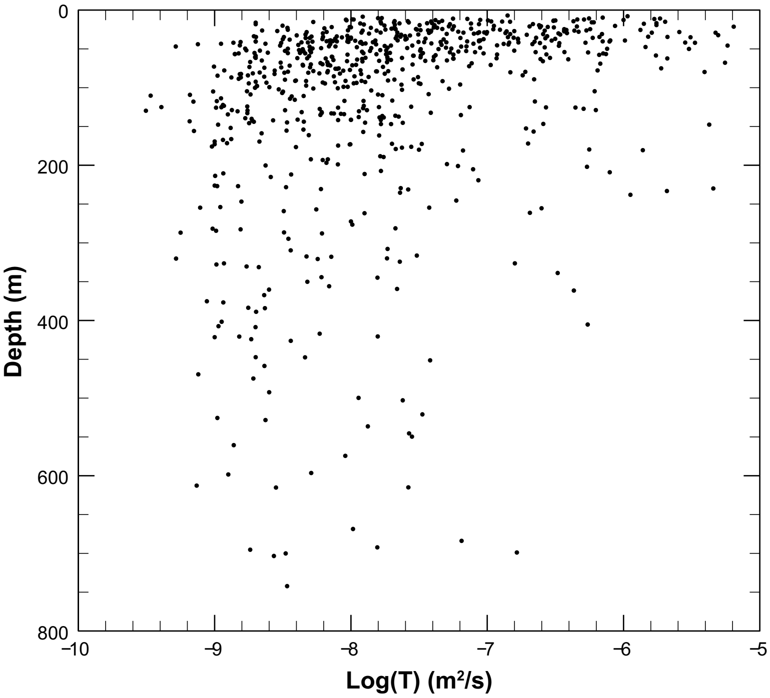

Figure 3-7. Fracture transmissivity versus depth for boreholes listed in Appendix A.

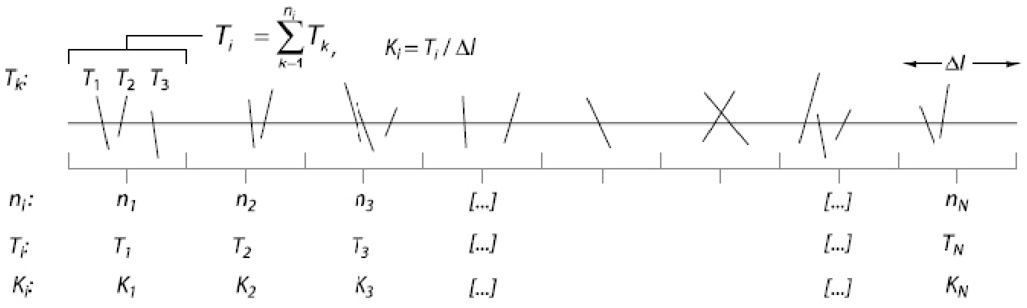

Figure 3-8. *Illustration of the calculation of EPM hydraulic conductivity along borehole intervals.*

A plot of computed transmissivity as a function of fracture density (Figure 3-9) shows that transmissivity, and therefore hydraulic conductivity, increases with fracture density. While the correlation coefficient is quite high for the mean values ($R^2 = 0.92$), the correlation is probably much weaker when using all the observed data. The following power law has been fitted between fracture density and transmissivity:

$$\log T = -\exp\left(-0.178 \ln \rho_f + 1.821\right) \tag{3-25}$$

Using Equation 3-24 the relationship between hydraulic conductivity and fracture density can also be plotted (Figure 3-10).

The relationship expressed by Equation (3-25) could be explained by the depth at which both fracture density and hydraulic properties are measured. Both density and transmissivity tend to be higher close to ground surface and the relationship could be a function of depth. The influence of depth was not analyzed here and it was rather assume that Equation (3-25) can be used to define facies using ranges of fracture density, which are proxies for hydraulic conductivity (Table 3-1). The first facies distribution generated is constituted of four facies, described as unfractured bedrock (UFB), slightly fractured bedrock (SFB), moderately fractured bedrock (MFB) and highly fractured bedrock (HFB) for which the range of fracture density and hydraulic conductivity values is given in Table 3-1. This classification is arbitrary and mainly inspired by the rock facies classification proposed by Park et al. (2004),

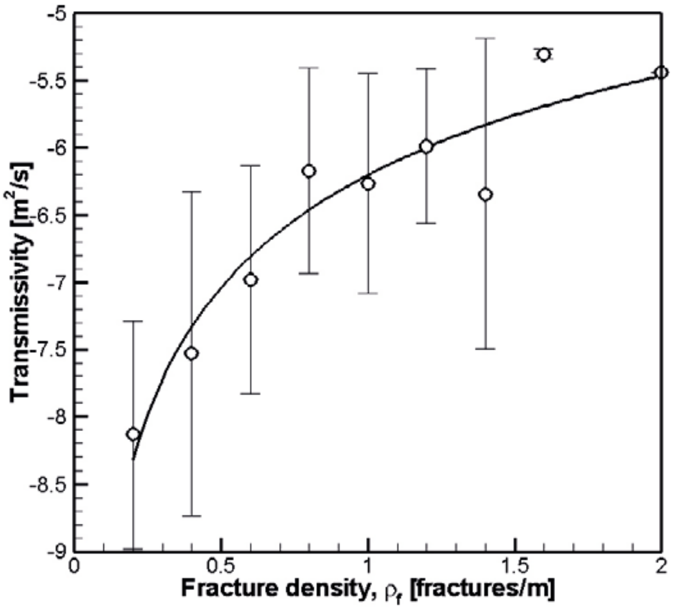

Figure 3-9. *Relationship between transmissivity and fracture density for all borehole intervals considered (interval length is 5 m).*

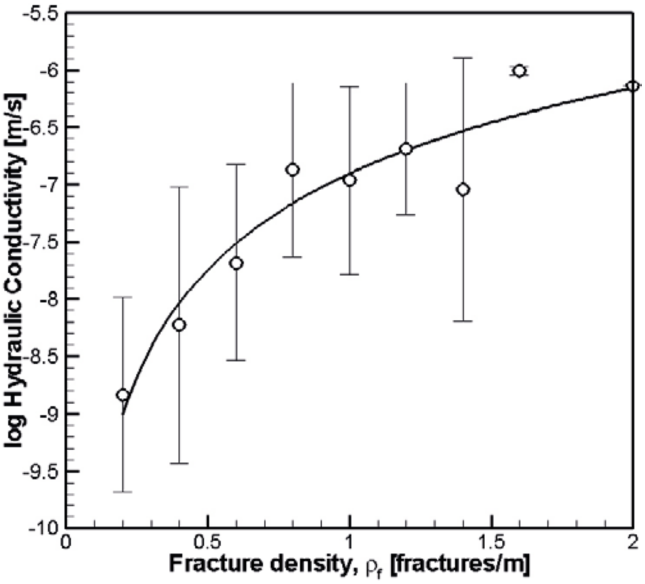

Figure 3-10. Relationship between hydraulic conductivity and fracture density for all borehole intervals considered (interval length is 5 m).

who applied the same transition probability geostatistical approach on the data collected from the Underground Research Laboratory in southeastern Manitoba, Canada. Facies SFB, SMFB (sparsely to moderately fractured), MFB, MHFB (moderately to highly fractured), and HFB were defined for fracture density varying from 0.1 to 2.5 fractures/m. On the basis of this previous work, facies configurations other than those presented in Table 3-1 are tested, as will be shown in Section 4.4.3.

The hydraulic conductivity values are calculated from this first facies distribution. Additional distributions were tested to calibrate the hydrogeological models considered in Task 7B. Average values of transmissivity will be used as initial values in the model but will be updated during the automated inversion process such that the final values of transmissivity for the facies will be different than presented here.

Table 3-1. Fractured rock facies.

Rock facies category	Fracture density range	Mean log T
UFB	$0 < \rho_f < 0.5$	–
SFB	$0 < \rho_f < 0.5$	−7.9
MFB	$0.5 < \rho_f < 1.0$	−6.5
HFB	$\rho_f > 1.0$	−5.9

3.4.4 Transitional probability model

On the basis on the theory presented in Section 3.3.2, the observed and the simulated transition facies probabilities are presented in the following section.

Vertical model development

The observed spatial transitional probabilities along the vertical direction are shown in Figure 3-11, along with the Markov chain model for the vertical direction shown with a solid line. The fit between observations and the model is good, although the model does not capture the exact shape of the observed transition rates. The sills, which correspond to the volumetric proportions (see Equation (3-4)) of facies, are given in Table 3-1. Inspection of the volumetric proportion reveals that most of the rock mass is unfractured, with less than 30% being fractured. Within the fractured rock mass, the largest volume is slightly fractured, followed by moderately and highly fractured. Also, although they were not explicitly used for fitting the Markov chain model, the observed vertical mean lengths of the facies are given in Table 3-2. The longest facies is the UFB while the remaining facies have about the same length (≈ 6 to 8 m).

Table 3-2. Statistical properties of the fractured rock facies.

	Facies			
	UFB	**SFB**	**MFB**	**HFB**
Proportions, %	67.93	23.75	6.10	2.22
Mean length (m)				
Vertical	28.5	8.2	7.8	6.8
Horizontal	60.6[1]	40.0	20.0	10.0

[1] Calculated during the Markov chain fitting process as background category.

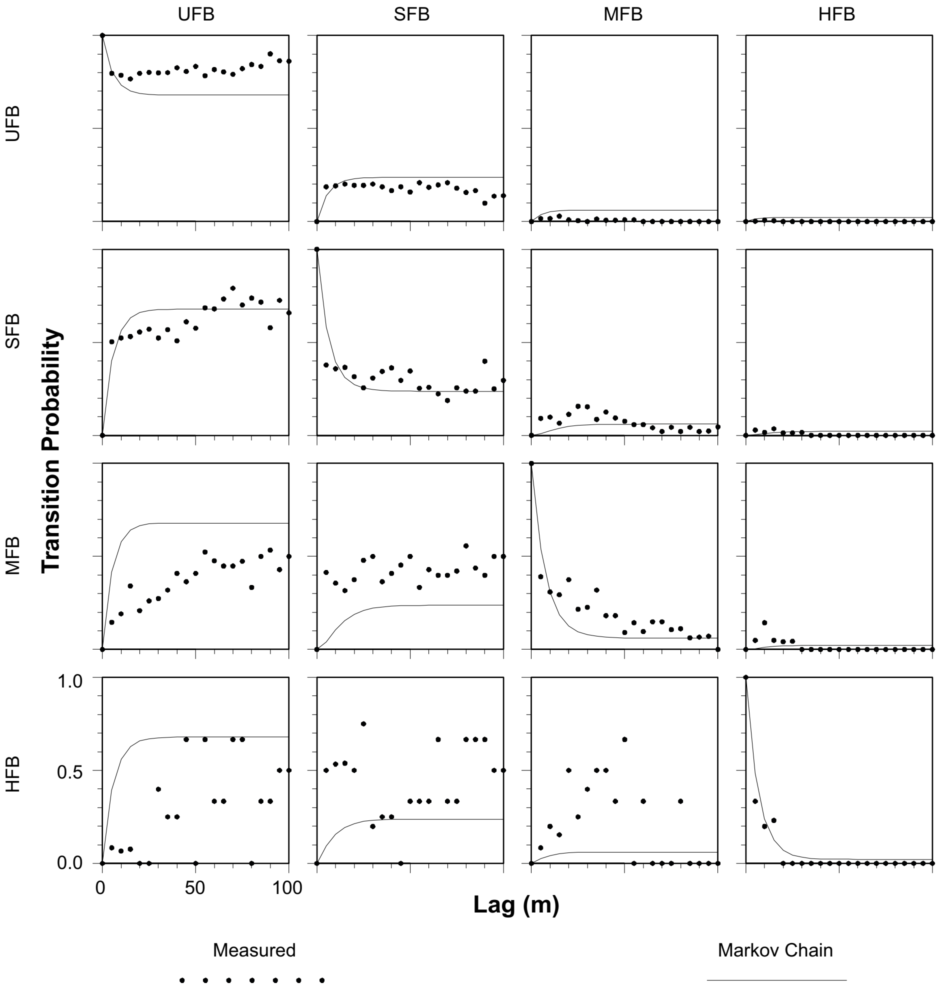

Figure 3-11. Observed transition probabilities along the vertical direction, and fitted Markov chain model.

The embedded transition probability matrix, Π_z, defined in Equation (3-6), is computed from observed transitions of facies along the boreholes. The embedded transition probability is the probability that a given facies is located above or next to a second facies, with the assumption that auto-transition, which is a transition from a given facies to itself, cannot be observed. The embedded transition probability matrix therefore provides a direct overview of transitions in the rock mass, and it is here given by:

$$\Pi_z = \begin{array}{r} \text{UFB} \\ \text{SFB} \\ \text{MFB} \\ \text{HFB} \end{array} \begin{bmatrix} & 0.39 & 0.35 & 0.26 \\ 0.99 & & 0.01 & 0.01 \\ 0.96 & 0.02 & & 0.02 \\ 0.91 & 0.05 & 0.04 & \end{bmatrix} \qquad (3\text{-}26)$$

The embedded transition probability matrix shown in Equation (3-26) indicates that there is a probability of 39% that SFB occurs above UFB, 35% for MFB and 26% for HFB.

Horizontal model development

The observed horizontal transition probabilities, shown in Figure 3-12, indicate that compared to vertical transitions, transition rates are not as well defined and that there is a large scatter in the spatial distribution of the transition probabilities. One reason is the absence of horizontal continuous facies measurements and the limited number of boreholes, which limits a direct fit with the Markov chain model. Horizontal facies length could not be observed because there are no horizontal boreholes in the area and because the spacing between the boreholes is larger than the length of the individual fractures. For this reason, other geological evidence is needed to infer a plausible horizontal length.

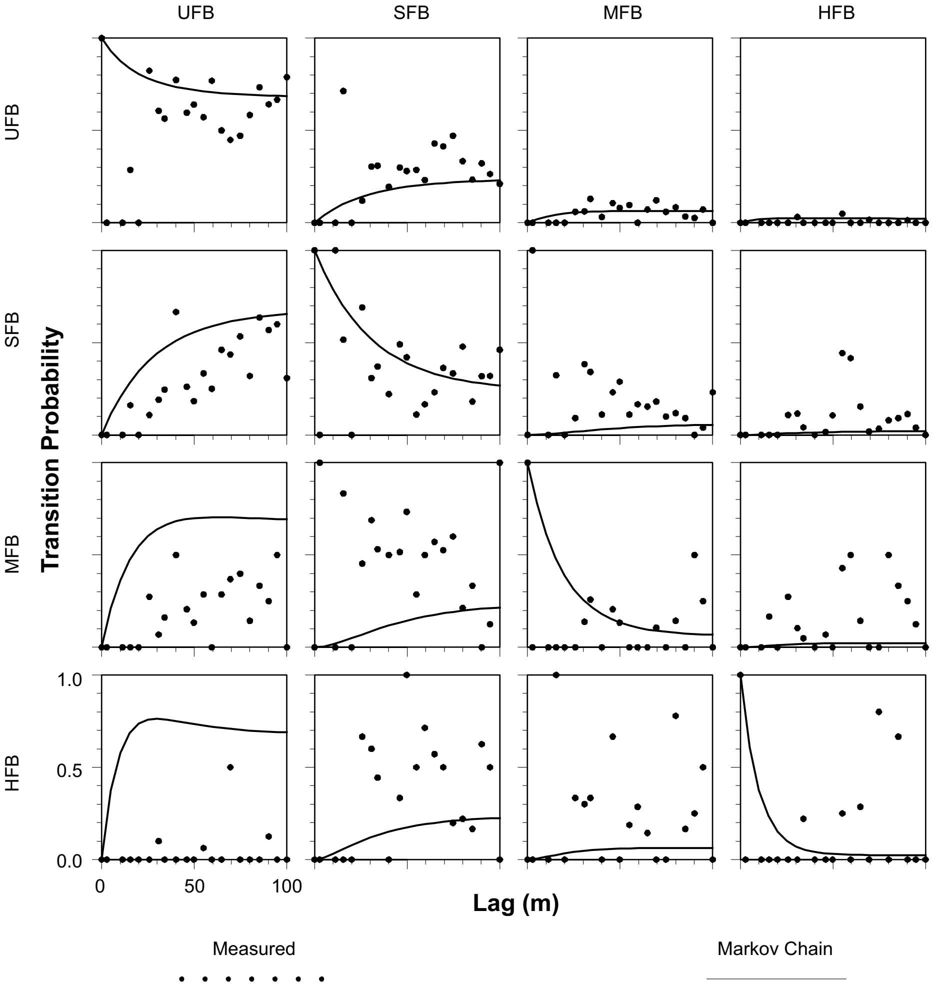

Figure 3-12. Observed transition probabilities along the horizontal direction, and fitted Markov chain model.

Several authors have linked individual fracture aperture to its length (Bonnet et al. 2001, Dershowitz et al. 2003a). The general form for this relationship is given by:

$$A=\delta L^{b} \tag{3-27}$$

where A is aperture, L is fracture length and δ and b are regression parameters. According to Bonnet et al. (2001), $b$varies between 0.5 and 2 and is close to one for isolated fractures. At Äspö (Sweden), Dershowitz et al. (2003a) have found an exponent b of 1.4 and a value of δ of 5.0×10^{-10}.

Structural geological mapping results at the Olkiluoto site are presented in Paulamäki (2007). A total of 933 fractures were measured across outcrops or observation points for N–S and E–W traverses. The fracture frequency is not controlled by rock type. The lengths of mapped fractures in the study area range from the lower cut-off of 1 m to 20 m, with only one fracture longer than 20 m. About 30% of the fractures are visible in their full length, their average length being 3.8 m. These values are limited to surface fractures. Since the frequency of hydraulic conductive fractures decreases with depth (Tammisto et al. 2009) and their length is more uncertain, fracture length values presented in Paulamäki (2007) are used to compare and support facies length values estimated using Equation (3-27) presented above.

We can predict a mean fracture length using the mean fracture transmissivity ($T = 2.0\times10^{-8}$ m^2/s) and realistic regression parameters. For instance, we know that most fractures have the same orientation (parallel fractures) and it could therefore be assumed that they are isolated from each other in the rock mass. For this type of fracture distribution, a coefficient b=1 has been found to be realistic (Bonnet et al. 2001). Coefficient $\delta$is assumed equal to the value obtained by Dershowitz et al. (2003a) in a similar environment ($\delta = 5.0\times10^{-10}$) at Äspö.

The mean length obtained with the aforementioned parameters is 40 m. This length is slightly below the average distance between boreholes KR14–18 (44.13 m, see Appendix A, Table A-2). This mean length seems realistic, and would represent the upper end of the estimated length interval, because background fractures are not assumed to extend across several boreholes.

The individual fracture length estimated above has to be translated into a facies length to be used in the Markov chain model. While the single fracture length estimate could be used for the SFB facies, more intensively fractured facies (MFB and HFB) are likely to have smaller length because fractures next to each other are not likely to extend similarly such that highly fracture zones will be shorter than the individual fractures. The basic hypothesis is that the facies length is comparable to the length of an individual fracture. This hypothesis is assumed valid for bedrock facies with low fracture density. As the fracture density increases, a facies length shorter than the length if individual fractures is considered. Here, it is estimated with Equation (3-27) that the SFB fractures have a length of 40 m and that MFB and HFB have lengths of 20 and 10 m, respectively. These latter two length values are assumed, in the absence of other data, and they are comparable to the fracture lengths measured during geological mapping at Olkiluoto (Paulamäki 2007).

The UFB facies is defined as the background facies so there is no need to specify a length; it will be computed automatically during the Markov chain fitting process. The mean length obtained after the fitting process is 60.6 m.

The embedded transition probabilities calculated along the vertical direction with Equation (3-26) are used along with the inferred mean horizontal facies length to fit the Markov chain model to the observed transition rates using Equations (3-5) and (3-7) as shown in Figure 3-11. Fitting the model to observation is difficult due to the scattered nature of the measurements, but it is now better constrained by using geological attributes.

Spatial model

Three-dimensional conditional simulations of fracture facies are created using the three dimensional Markov chain model along with sequential indicator simulation and simulated quenching (Carle 1996, 1997a). The three dimensional Markov chain model is simply the three one-dimensional Markov chain models (strike, dip, upward) defined in the previous two sections. The strike and dip Markov chain models are the same because it was assumed that the rock mass was isotropic along the mean fracture plane.

Conditional simulations create multiple, equally probable, spatial distribution of the fracture facies that honour data observed along the boreholes, which are in this case fracture facies. Conditional simulations should therefore not be seen as spatial interpolation, but rather as stochastic realizations. One simulation produced by conditional sequential indicator simulation and simulated quenching based on the three-dimensional Markov chain model is presented in Figure 3-13, where the domain is truncated to show borehole KR14 at the front of the domain. The white cells in the model indicate the location of the boreholes where the model is conditioned. It can be seen that the facies are elongated along a plane that is almost horizontal and characterized by a dip of 9°, which is the average value for the 706 background fractures analyzed (Figure 3-5). This dip value is low and thus not easily visible in the simulation domain presented in Figure 3-13 due to the coarse cells used.

Background fractures in the study area are sub-horizontal. The rock facies considered to define the conceptual model are the following:

1. Unfractured Bedrock, UFB.
2. Sparsely Fractured Bedrock, SFB.
3. Sparsely to Moderately Fractured Bedrock, SMFB.
4. Moderately to Highly Fractured Bedrock, MHFB.
5. Highly Fractured Bedrock, HFB.

Four hydrostructural models are considered to test their influence on groundwater flow simulation results (Table 3-3). All models are based on transitional probabilities of facies to characterize the background fractured rock. Model-4 is composed of five facies (UFB, SFB, SMFB, MHFB, HFB), while other models (Model-1 to Model-3) contain four facies (SFB, SMFB, MHFB, HFB). The difference between Model-1 and Model-2 is the seed used for random number generator used during the conditional simulations executed with T-PROGS. The different seed provides a distinct, but equally probable, spatial facies distribution. Using Model-2 in addition to Model-1 allows to evaluate the influence of the spatial distribution of facies on the groundwater flow simulation results.

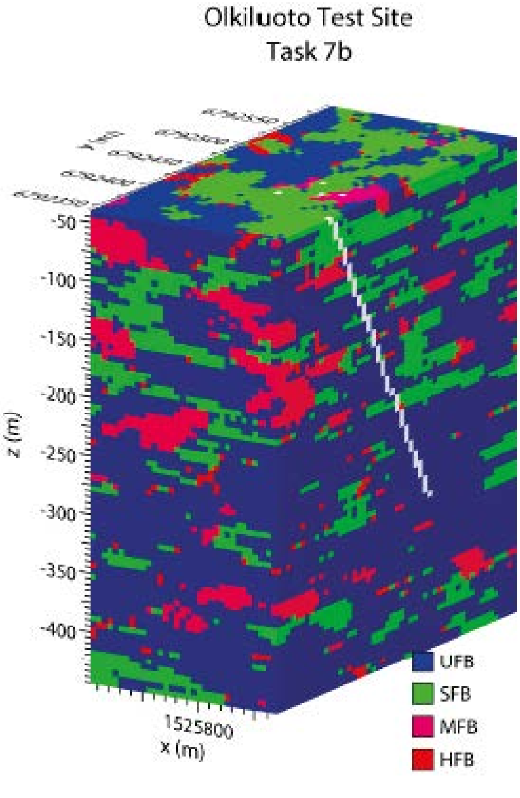

Figure 3-13. Example of a geostatistical realization of the fracture distribution.

In Model-3, two discrete fractures where added to the four facies characterizing the background fractures. Model-3 is the reference model for numerical simulation, although some comparisons of results obtained with other models will be presented. The model names listed in Table 3-3 are used to distinguish the different simulation results throughout this report.

An overview of the hydrostructural models tested with groundwater flow simulations is given in Figure 3-14, where the difference in facies distribution is clearly visible in Figure 3-14a, Figure 3-14b, and Figure 3-14c, while in Figure 3-14d two discrete fractures added to represent major fracture zones are shown. More details on these two fractures will be given in Section 3.5.1.

Table 3-3. Different hydrostructural models considered in this study.

Model name	Number of facies	Discrete fractures
Model-1	4	NO
Model-2	4 (different seed)	NO
Model-3	4	YES
Model-4	5	NO

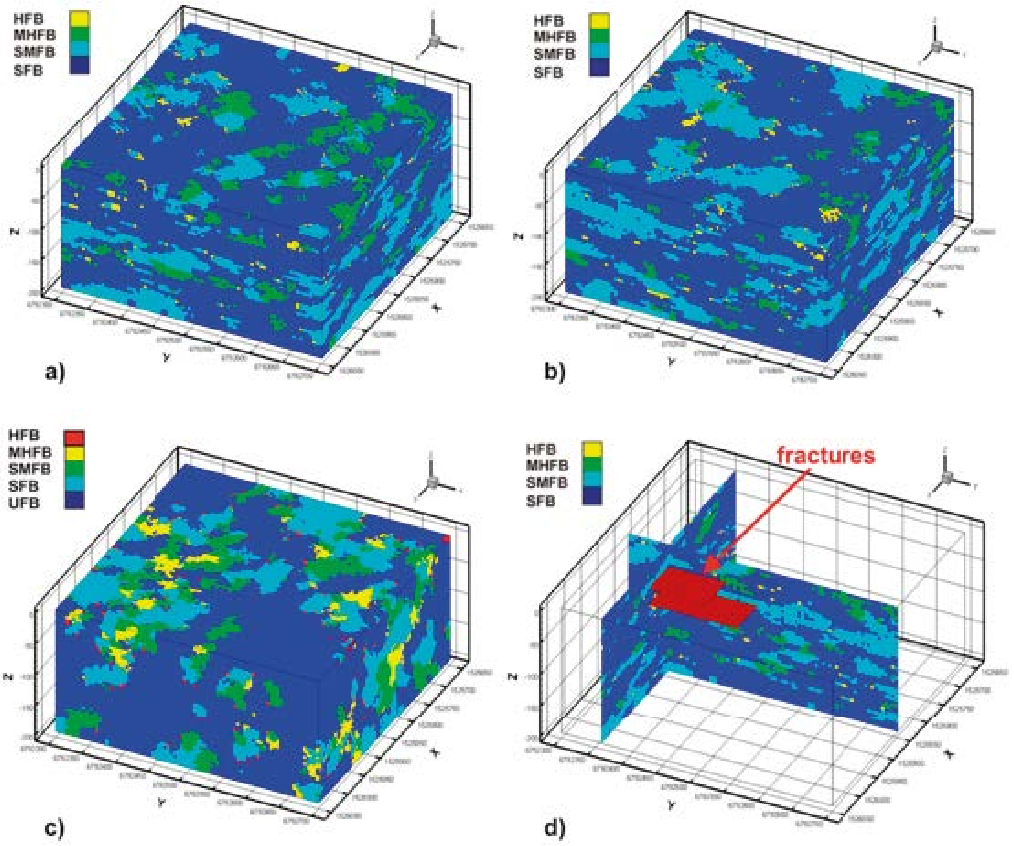

Figure 3-14. *Different hydrostructural models tested: a) 4 facies, base case b) 4 facies, alternative spatial distribution c) 5 facies and d) 4 facies + two discrete fractures.*

3.5 Simulations

Table 3-4 lists the simulations that have been completed for Task 7B. All simulations have been completed, but the approach taken for simulations PA20C and PA29 does not use particle tracking, as suggested, since particle tracking is not available within the HydroGeoSphere model.

Table 3-4. List of simulations for Task 7B.

Name	Description	Boreholes	Purpose
SS20a	"Natural conditions"	No boreholes	Forward
SS21	"Natural conditions"	Boreholes are open and free to cross-flow	Calibration
SS22	"Natural conditions"	Boreholes are packed-off	Calibration
SS20b	"Natural conditions"	No boreholes	Based on models calibrated after SS21 & SS22
PA20c	"PA conditions"	No boreholes	Forward
SS23a	Pumping in KR14	Boreholes are open and free to cross-flow	Forward
SS23b	Pumping in KR14	Boreholes are open and free to cross-flow	Calibration
SS24a	Pumping in KR14	Boreholes are packed-off	Forward
SS24b	Pumping in KR14	Boreholes are packed-off	Calibration
SS25a	Pumping in KR18	Boreholes are open and free to cross-flow	Forward
SS25b	Pumping in KR18	Boreholes are open and free to cross-flow	Calibration
SS26a	Pumping in KR18	Boreholes are packed-off	Forward
SS26b	Pumping in KR18	Boreholes are packed-off	Calibration
TS27	Pumping in KR15	Boreholes are open and free to cross-flow	Forward
TS28	Pumping in KR14	Boreholes are open and free to cross-flow except for one isolated flowing structures in other boreholes	Forward
PA29	"PA conditions"	No boreholes	Forward

Results shown here focus on calibrated models, while results from forward models are used as initial conditions, or estimates, for calibration. Only hydraulic head observations are considered in the first phase of calibration. In general, pumping in KR14 is reproduced more accurately than pumping in KR18. Further inverse modelling has been performed to include flow observations (Posiva Flow-logging data) as targets for calibration. Adding flow measurements as calibration targets is motivated by the fact that the Task 7B performance measures include flows and heads at a series of locations in different boreholes (Vidstrand et al. 2015). As indicated in the data delivery, the borehole flow distribution should be computed and compared to the PFL measurements during pumping in boreholes KR14 and KR18. PFL flow values are given for borehole sections 2 meters apart. In contrast, the mesh resolution is 5 meters. Thus, flow measurements are associated to the nearest mesh node, which may not be the exact location of the PFL measurement. The comparison between PFL measurements and simulated flows has been conducted in the last part of the Task 7B modelling, since some developments of the HydroGeoSphere-PEST interface were required to incorporate flow observations as targets for calibration.

Adding different types of data generally provides more information about the system. In groundwater flow model calibration, it is important to provide information about flows. Hydraulic heads often do not contain enough information, as indicated by the frequency with which extreme values of parameter correlation coefficients occur when using only hydraulic heads (Hill 2004). Simulations are at first for cases without prior information. Then, the addition of prior information was also tested and its effect on model outcome is discussed below.

3.5.1 Simulations setup

The mesh generated with HydroGeoSphere for subsurface flow simulations has the same spatial resolution and dimensions as the one created with T-PROGS. The facies distribution created with T-PROGS is then used to define the fractured rock hydraulic properties for the HydroGeoSphere simulations.

The four hydrostructural models presented in Figure 3-14 have been tested. No noticeable change in the objective function value is observed between models, although computed hydraulic heads at observation boreholes are different. Additional observation boreholes have also been included to evaluate the variation in computed hydraulic heads between models. Simulations for the four initial models suggest that representing background fractures with T-PROGS facies was not enough to characterize the hydraulic response to pumping, especially for simulations SS23 and SS24. Therefore, it was decided to introduce two discrete fractures (KR14_4H and Plane-1) in the hydrostructural model, on the basis of the hydraulic features characterized during the interference tests conducted at Olkiluoto.

Information on hydraulic features at the block-scale, representative of the KR14–KR18 region, is found in Klockars et al. (2006). Hydraulic feature KR14_4H was identified as causing the strongest observed responses during a pumping test in borehole KR14. This feature connects the section of borehole KR14 around 50 m to shallow boreholes KR15B and KR18B. The water level observations also show that structure KR14_4H has better flow connection to B-boreholes than to the other boreholes. A second hydraulic feature mentioned by Klockars et al. (2006) is Plane-1, which describes hydraulic connection between borehole KR14 and the uppermost observation levels in boreholes KR15–KR18. Because boreholes KR15–KR18 are cemented down to about 40 m, and the depth of boreholes KR15B–KR18B is only about 45 m, the difference in water level observations during the interference test between deeper boreholes and B-boreholes leads to the assumption that hydraulic connections between boreholes are mostly sub-horizontal (Vaittinen et al. 2003).

For the simulations including discrete fractures, the fracture aperture in forward modelling and initial value during inverse modelling is set to 1×10^{-4} m, which corresponds to a transmissivity of 9.1×10^{-5} m^2/s. For comparison, Vaittinen et al. (2003) indicate that the transmissivity of fracture KR14_4H is 3.2×10^{-5} m^2/s. Discrete fractures KR14_4H and Plane-1 are represented, for the sake of simplicity, as horizontal planes in the model, therefore not accounting for their precise location and geometry. Representing these fractures as horizontal planes is justified by the fact that simulation results are influenced by the fracture aperture and by the connections fracture-borehole, while the precise spatial location and geometry of fractures have less impact at this scale. In addition, as mentioned above, these fractures have been characterized as sub-horizontal (Vaittinen et al. 2003), such that it can be assumed that the use of horizontal planes is appropriate.

In the model, long inclined boreholes, in particular KR14, are split into several connected intervals to try to better reproduce their trajectory. The discretized boreholes are shown in Figure 3-15, where their staircase profile defined on the regular spaced block-based mesh, used to generate the T-PROGS facies, is clearly visible, especially for KR14.

The isotropic hydraulic conductivity values used for forward modelling are listed in Table 3-5. Background facies SFB is not included in the estimation process and a low hydraulic conductivity is assumed for that facies. In addition, anisotropy is considered for SFB to improve calibration, with $K_x = 6.3\times10^{-8}$ m/s and $K_y = K_z = 3.2\times10^{-9}$ m/s. Hydraulic conductivity can be estimated using its real, or native, value or by using its logarithm. Log-transformations can produce an inverse problem that converges more easily and prevents the native parameter values from becoming negative (Hill and Tiedeman 2007). Using native values has the advantage of emphasizing the connection between model results and field data. It is generally better that modellers use native values as much as possible (Hill and Tiedeman 2007).

Table 3-5. Hydraulic conductivity values in forward modelling.

Facies	K [m/y]	K [m/s]
SMFB	15	4.7×10^{-7}
MHFB	60	1.9×10^{-6}
HFB	250	7.9×10^{-6}

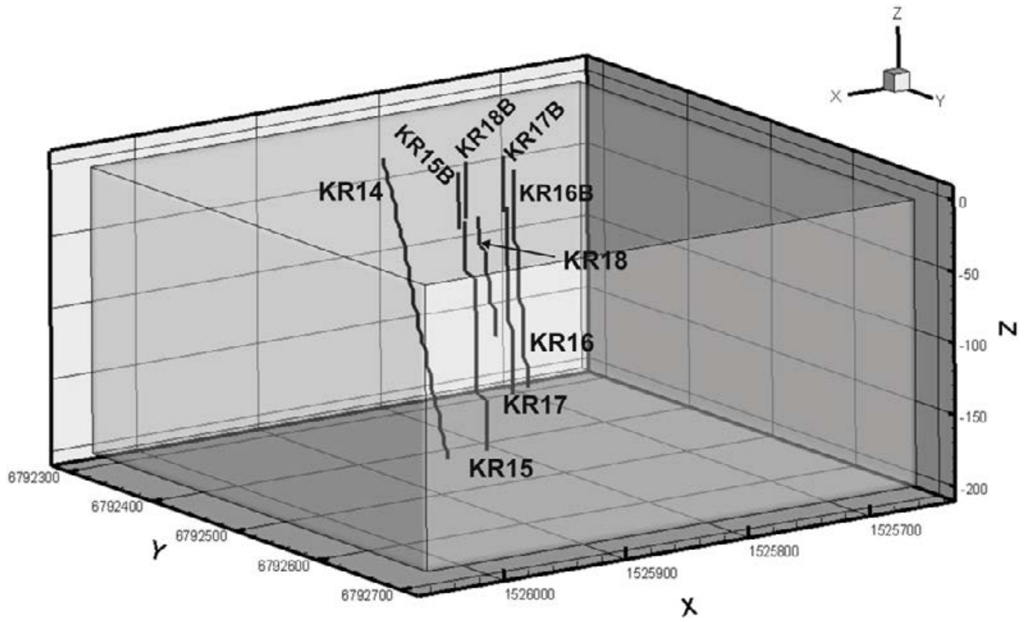

Figure 3-15. Discretized boreholes in the HydroGeoSphere mesh.

Some calibration tests using log-transformed parameters were conducted for simulation SS23, using only hydraulic heads as observations and without prior information. The results obtained were not conclusive. Although the lower bounds of confidence intervals remain always positive, the whole interval is wider if the log-transformation is considered. Very large upper interval bounds are obtained, such as a hydraulic conductivity on the order of magnitude of 10^{-2} m/s for the SMFB facies or 10^{7} m/s for MHFB facies. PEST provides linear confidence intervals, which should be seen as an indication of the uncertainty for estimated parameters and not as absolute intervals. The relationship between hydraulic head and hydraulic conductivity is non linear for a parameter estimation problem and a breakdown in the linearity assumption may cause exaggerated confidence interval size and, as consequence, an extreme uncertainty on the parameter value. There is no detailed information on the determination of confidence intervals with PEST and the parameter log-transformation provides results whose interpretation is not straightforward. It should be mentioned that, as expected, the convergence of the inverse problem is faster for log-transformed parameters, where only 62 model calls are executed by PEST, than for native parameters, where 111 model calls are required. On the basis of these observations and considering that one of the main goals of this task is to provide some indications on the uncertainty associated with the system, the use of native parameters is preferred.

For transient simulations TS27 and TS28, the porous rock specific storage is assumed equal to 1×10^{-6} m, which is the value used for simulations in Task 7A. The two discrete fractures considered in Model-3 are assumed non deformable and fluid-filled, such that there is no contribution to the storage term from fracture compressibility. With that assumption, their specific storage is:

$$S_{s_f} = \rho_w g \alpha_w = 1000\left[\frac{kg}{m^3}\right]\times 9.8\left[\frac{m}{s^2}\right]\times 4.4\times10^{-10}\left[\frac{m\,s^2}{kg}\right] \approx 4.4\times10^{-6}\left[m^{-1}\right] \qquad (3\text{-}28)$$

To speed up simulations during PEST calibration, hydraulic heads computed for the forward modelling simulations are used as initial hydraulic heads in HydroGeoSphere prior to launching PEST. These initial hydraulic heads are to closer to the resulting computed heads than would arbitrary initial hydraulic heads, which speeds up the head solution in HydroGeoSphere since it uses an iterative matrix solver. The gain in computational efficiency is significant because PEST launches a large number of HydroGeoSphere simulations during calibration.

Computation of hydraulic heads is strongly controlled by the fixed heads imposed at the top boundary. This boundary condition is removed for simulations of pumping in boreholes KR14 and KR18. This choice is motivated by the difficulty to reproduce the measured drawdown by keeping the first-type boundary condition at the top of the domain, as explained further in the description of SS25.

Observed drawdown is preferred to hydraulic head as calibration target because it reduces the influence of the undisturbed head distribution, as explained in the performance measures data delivery. However, as the PEST calibration targets are hydraulic heads, they are calculated from the undisturbed head distribution considering the observed drawdown.

HydroGeoSphere simulations runs much faster if the borehole radius is lowered from 0.04 to 0.001, but the smaller radius causes an unrealistic and large variation in hydraulic heads along well axes, especially if pumping is simulated. For simulation SS21, without pumping, a radius of 0.001 m causes a large variation in the hydraulic heads, such that model calibration will depend on the position of the observation points along the borehole axes. Therefore, a radius equal to 0.01 m has been chosen, as a trade-off between computing time and appropriate hydraulic head computation.

As explained in Section 3.3.3, accuracy in derivative calculations is fundamental to PEST's success in optimizing parameters. A very low flow solver convergence value, 1.0×10^{-12}, is adopted in HydroGeoSphere for the iterative solution of the flow equation. This low value contributes to more accurate derivative computation, but it slightly increases the simulation CPU time.

Locations of observation points for simulations SS21, SS23, and SS25 are listed in Table 3-6, together with borehole top and bottom z coordinates. Boreholes KR15–KR18 are cemented down to about 40 m while the depth of boreholes KR15B–KR18B is only about 45 m, as explained in Section 2. Because the borehole discretization depends on the mesh type and its resolution, the location of observation points must be carefully checked. Nodes that do not belong to the boreholes may be selected as observation points. This error may lead to a misleading interpretation of numerical results. One observation point per well is used for simulation with open boreholes, while separated borehole sections are defined to reproduce the packed-off boreholes for simulations SS24 and SS26.

Table 3-6. Boreholes and observation points for simulations SS21, SS23, and SS25.

Borehole	Top [m]	Bottom [m]	Observation point depth [m]
KR14	0	−200	−120
KR15	−40	−200	−120
KR15B	0	−45	−15
KR16	−40	−170	−95
KR16B	0	−45	−25
KR17	−40	−155	−95
KR18	−40	−125	−70
KR18B	0	−45	−25

Simulations SS23 and SS25 concern the difference flow method used to analyze hydraulic cross hole interference tests conducted between December 2001 and April 2002 (Rouhiainen and Pöllänen 2003). Simulations SS24 and SS26 concern the hydraulic crosshole interference tests carried out in the same boreholes during the Fall 2004 and described in Klockars et al. (2006).

Simulation SS20A

This first simulation does not include boreholes. A first-type flow boundary condition representing the water-table is imposed to the top and lateral domain boundaries. The groundwater flow field simulated here is then used for PA simulations, which are presented later and where particle tracking and mean life expectancy are calculated. Hydraulic head contours and hydraulic gradient are influenced by the facies distributions, as shown in Figure 3-16. A discharge zone is visible in the North-East portion of the domain, for the slice located at y=6 792 350 m.

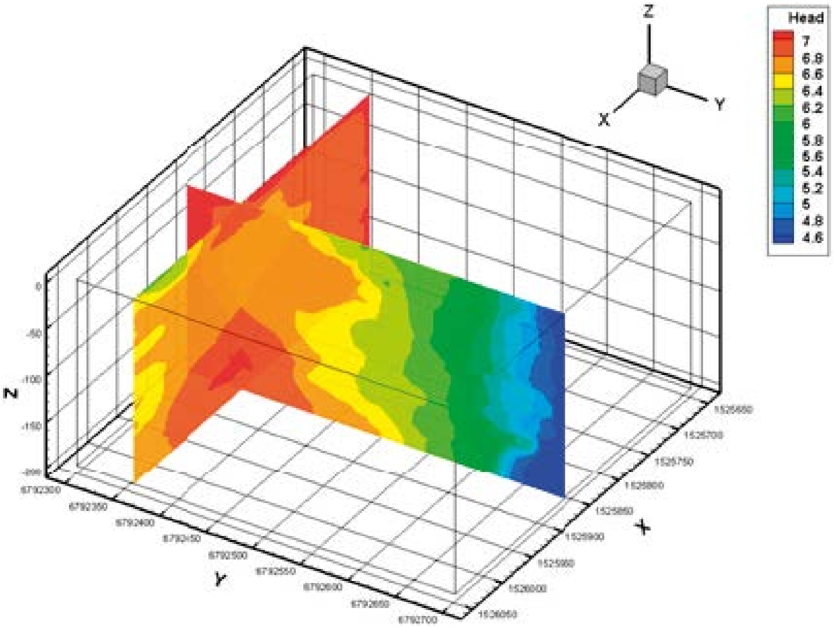

Figure 3-16. *Hydraulic heads for SS20A, slices inside the domain located at x=1 525 850 m and y=6 792 350 are shown.*

Simulation SS21

This simulation is identical to SS20A, except that open boreholes are now included in the model. Eight observation points are included in the model and they are located in boreholes KR14, KR15, KR15B, KR16, KR16B, KR17, KR18, and KR18B, respectively (Table 3-6). Borehole KR17B is not included as an observation point because its measured head is higher than 8 m, which is greater than the highest value of mean long term water-table data used to define the first-type boundary condition at the top of the domain, and cannot be reproduced with that boundary conditions. Only heads values below 7.0 m can be simulated, since the highest water-table value is 7 m. A value of 0.2 m was subtracted to all observed heads, as the measurements were taken when the water-table was lower than the mean water-table elevation.

The undisturbed hydraulic head distribution simulated (Figure 3-17) is considered as initial conditions for pumping simulations SS23, SS24, SS25, and SS26. Thus, the simulated drawdown for those simulations will be calculated with reference to the head distribution simulated here. Comparing hydraulic heads shown in Figure 3-17 to those obtained for SS20 (Figure 3-16) shows the influence of open boreholes on computed hydraulic heads. For example, the heads are higher around borehole KR14, since open boreholes are high-permeability elements that create connections between the fractured rock facies, therefore increasing the global hydraulic conductivity of the domain.

Several trials with different hydraulic conductivity values and variation of calibration parameters suggested that the objective function could not be lowered below 0.07, using realistic intervals for fitting hydraulic conductivities. Allowing large ranges for hydraulic conductivity variations may lower the objective function and improve calibration, excessively low or high hydraulic conductivity will be inappropriate for the other scenarios that simulate pumping in borehole KR14 and KR18. In addition, if PFL flow measurements are included as targets for calibration, the hydraulic conductivity must be appropriate to ensure that computed flows are of the same order of magnitude as measured flows. Simulated and measured heads for SS21 are shown in Figure 3-18. It was difficult to reproduce the small hydraulic head variations observed, that are between 6.7 m and 6.85 m. Regardless of the hydraulic conductivity values in the simulation, the calculated heads are almost all equal to 6.8 m. This result is probably caused by specifying the water-table as the top boundary condition.

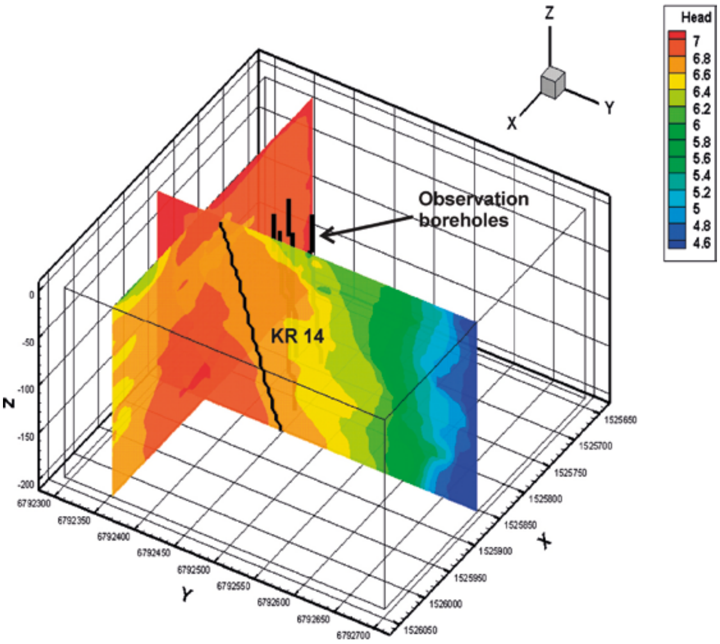

Figure 3-17. *Hydraulic heads for SS21, slices inside the domain located at x=1 525 850 m and y=6 792 350 m are shown together with the discretized boreholes (black lines).*

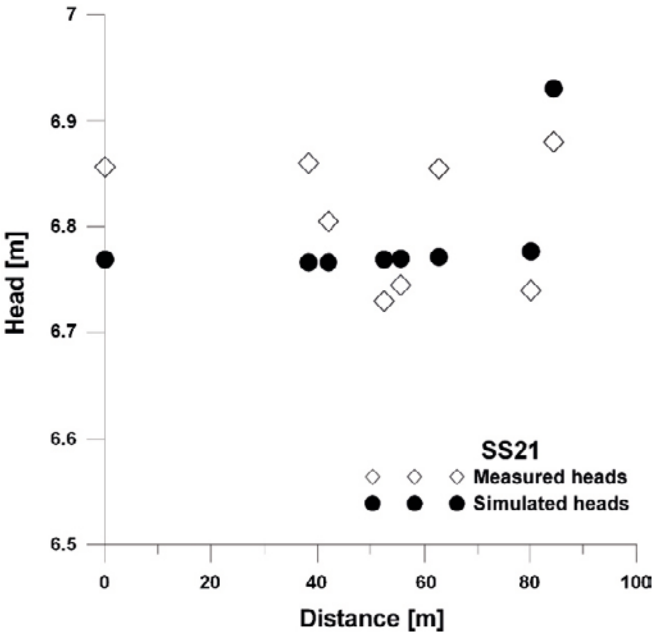

Figure 3-18. *Simulated and measured hydraulic heads for SS21.*

Simulation SS22

Packed-off boreholes are considered here. A total of 26 packed-off sections are represented in the model and each section contains an observation point. The complete list of the packed-off sections is listed in Appendix B (Table B-1).

The hydraulic head variation in the different packed-off intervals is relatively small. The best result obtained through inverse modelling is ϕ=6.4 and R=0.5. These two values indicate a poor fit between simulated and observed heads. The first-type boundary condition at the top of the domain controls the variation of heads, making it difficult to capture the low hydraulic heads (< 6 m) in borehole intervals KR15_L3, KR16_L1, KR16_L2, and KR17_L1. All simulated hydraulic heads are between 6.6 and 6.8 m.

Simulation SS23

Simulation SS23 considers pumping in KR14 and includes open boreholes. For Model-1, without discrete fractures, the simulated drawdown is larger than measured drawdown at the pumping well, while it is lower at observation boreholes. Discrete fractures were therefore added to better match measured and simulated heads. As discussed in Section 3.5.1, including discrete fractures is based on the interpretation of hydraulic features described in Klockars et al. (2006). After analyzing the facies distribution along borehole KR14, two discrete fractures were added to the conceptual model at the location of the highly-fractured facies. The location of the highly-fractured facies corresponds to the location of hydraulic features KR14_4H and Plane-1, as indicated in Klockars et al. (2006).

Calibration of Model-1 produces negative residuals at observation boreholes and a positive residual, equal to 2.5, at borehole KR14 (Figure 3-19). In contrast, for Model-3, a better distribution of residuals is observed (note that the scale for the vertical axis is different for Figure 3-19a and Figure 3-19b). Results shown in Figure 3-19 were obtained by considering only head measurements as targets for calibration. Table 3-7 shows the differences in simulated drawdown between forward and inverse modelling with Model-1 and Model-3, while Figure 3-20 presents the heads inside the domain during pumping at borehole KR14.

Confidence intervals for estimated hydraulic conductivities, shown in Figure 3-21 and Figure 3-22, illustrates that K_{HFB} is the value with the highest uncertainty since facies HFB has the lowest volume proportion, as explained in Section 3.4.4. The upper bound for K_{HFB} is 1×10^{-3} m/s (Figure 3-21), which is probably too large for highly-fractured crystalline rock.

Table 3-7. Drawdown measured and simulated for SS23.

Observation borehole	Measured drawdown	Simulated drawdown forward[2]	Simulated drawdown calibrated[2]	Simulated drawdown calibrated[1]
KR14	6	6.2	6.0	8.5
KR15	3.4	3.8	3.6	3.1
KR15B	4.4	4.8	4.6	3.1
KR16	3	3.2	2.9	2.4
KR16B	3	3.8	3.6	2.6
KR17	3	3.3	3.0	2.4
KR18	3	3.7	3.5	2.8
KR18B	5.6	4.8	4.6	3.1

[1] Base case, Model1.
[2] With fractures, Model3.

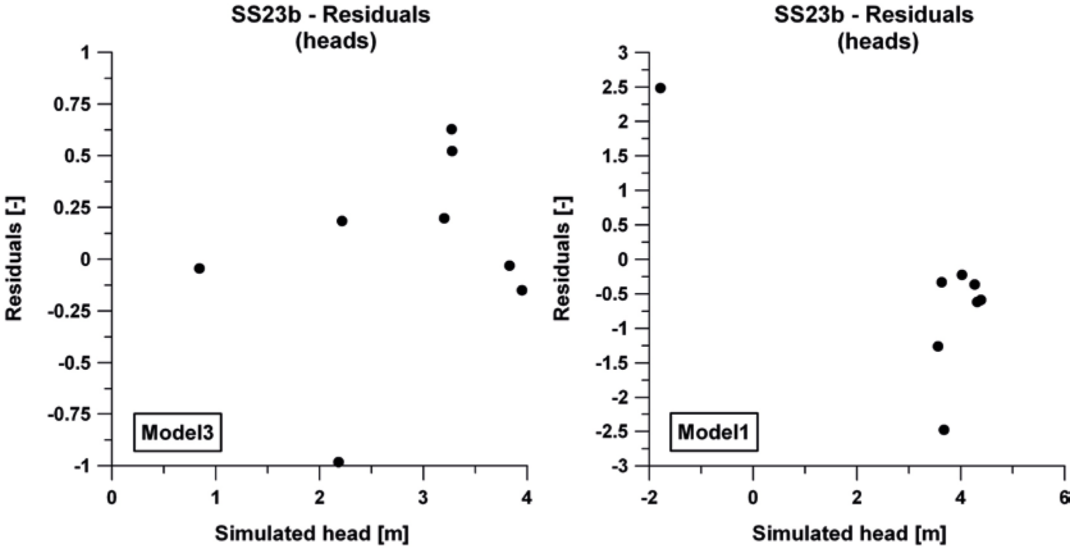

Figure 3-19. Residuals for simulation SS23b with Model-1 and Model-3.

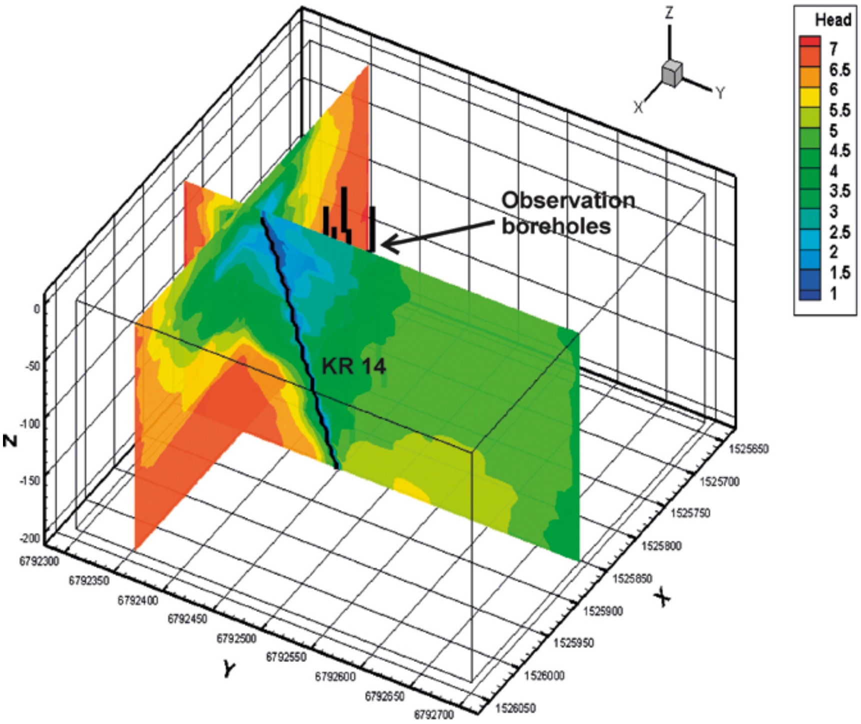

Figure 3-20. *Hydraulic heads for SS23b for vertical slices inside the domain located at x = 1 525 850 m and y = 6 792 350 m, with locations of the discretized boreholes (black lines).*

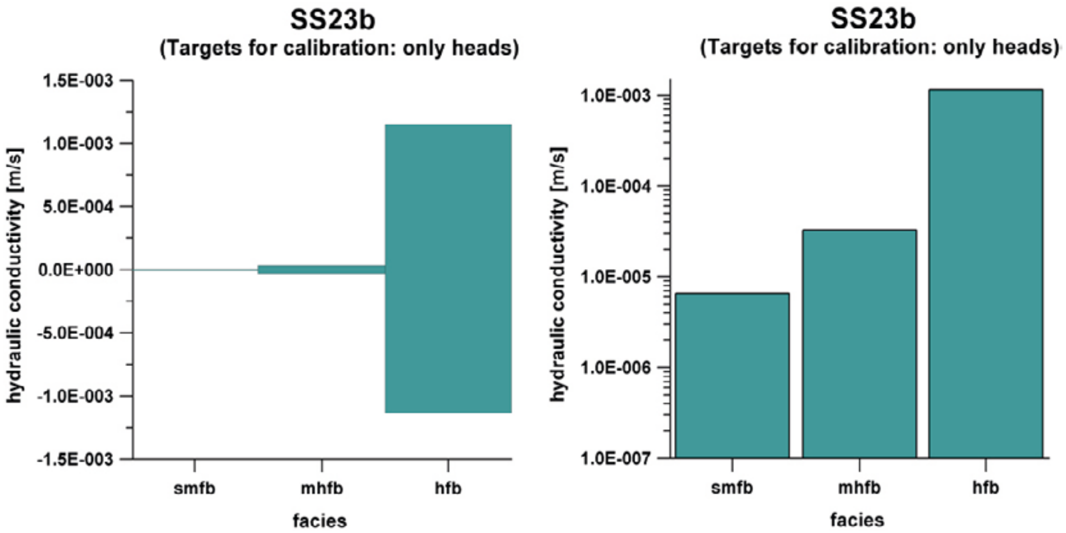

Figure 3-21. *Facies hydraulic conductivity confidence intervals: hydraulic heads are the only targets for calibration (logarithmic scale on the right).*

To reduce the uncertainty in parameter estimation, the following prior information (PI) is added to the PEST calibration:

$$\begin{aligned} K_{MHFB} &= 4 \cdot K_{SMFB} \\ K_{HFB} &= 8 \cdot K_{SMFB} \end{aligned} \qquad (3\text{-}29)$$

These relations assume that hydraulic conductivity varies from one facies to another according to the increase in the fracture density. From core observation and PFL measurements, the average transmissivity values give a ratio K_{MHFB} / K_{HFB} equal to 4 (Table 3-2). The facies whose hydraulic conductivity should be estimated here are SMFB, MHFB, and HFB, as indicated in Table 3-5.

The same ratio of 4 is used to constrain the hydraulic conductivity values by introducing prior information expressed by Equation (3-29), which gives a trend between K and p_f similar to that shown in Figure 3-10.

The resulting confidence intervals with prior information are presented in Figure 3-22. The interval width is significantly reduced compared to calibration without prior information (Figure 3-21). However, the intervals still include negative values, which are unrealistic for hydraulic conductivity.

In a second phase of inverse modelling, PFL measurements were added to hydraulic heads as targets for calibration. Because these observations (targets) are of different types (heads measured in m and flows in m^3/y), different observation weights are chosen. Weights should be inversely proportional to the standard deviations of observations, with "trustworthy" observations having a greater weight than those that cannot be trusted as much (Doherty 2004). Moreover, the weights assigned to different observation types should reflect the relative magnitudes of the numbers used to express the different quantities; in this way the set of larger numbers will not dominate the parameter estimation process just because the numbers are large (Doherty 2004). Based on these guidelines, weights equal to 0.1 and 1 are assigned to flow and head observations, respectively. These values are arbitrarily chosen on the basis of the measured flow values, which are usually one or two orders of magnitude greater than hydraulic heads. Moreover, PFL measurements are available for borehole intervals that are 2 m long, while the spatial resolution of the numerical model is 5 m. Therefore, there is some uncertainty coming from the exact location at which the measurement was taken. Additional uncertainty comes from the fact the sum of measured flow along borehole axes it is not always equal to the total withdrawal from the borehole. These two main sources of uncertainty justify a lower weight for flow than for head measurements.

The only observations used for performance measures are for the deep boreholes but a series of simulations were performed to analyze the influence of observations and weights on calibration. The only target considered for pumping borehole KR14 is flow measurement because a large variation between measured and simulated flow rates is observed at KR-14. It is assumed that it is more important to reproduce the response at observation boreholes than the distribution of flow along the pumping borehole. It is essential to simulate the hydraulic response at observation boreholes to assess the connectivity of the fractured rock at the block-scale. The pumping rate assigned to borehole KR14 is equal to the flowrate used during the pumping test (25 l/min), such that the water volume extracted from the borehole during the simulation is consistent with the test conducted at the site.

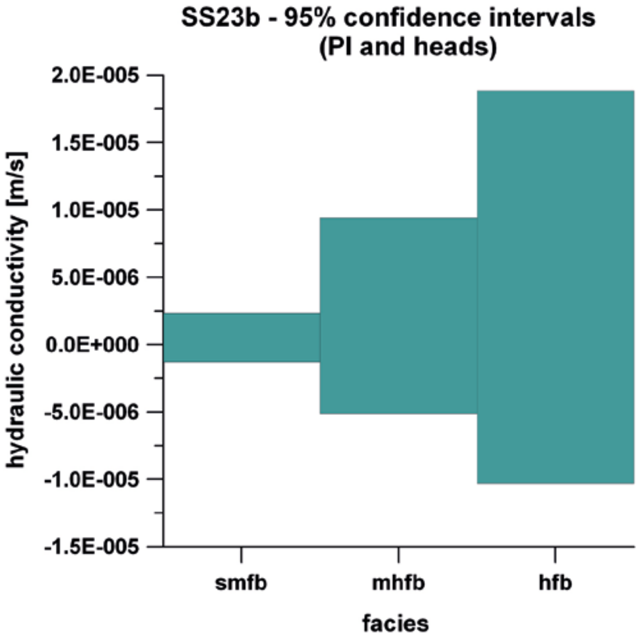

Figure 3-22. *Facies hydraulic conductivity confidence intervals: prior information and hydraulic heads are the targets for calibration.*

In Figure 3-23, the residuals obtained from the simultaneous calibration of head and flow values are shown, along with prior information. The total number of flow observations considered for this simulation is 37. As two different types of observations with different units and weights are considered, the titles "weight*residual" and "weight*modelled value" are preferred for axes y and x, respectively. Larger residuals come from flow observation and they are between +10 and −13, and show a symmetric distribution around zero. A weight equal to 0 was assigned to the flow observation in KR14 because a residual greater than 30 would have otherwise been obtained. Any given observation can be provided with a weight of zero such that it does not affect optimisation at all (Doherty 2004).

The confidence intervals for SS23b are presented in Figure 3-24. The difference with previous results that used only hydraulic heads as targets for calibration (Figure 3-21 and Figure 3-22) is obvious because the confidence intervals for SS23b are narrower and include only positive values of K. Using flow measurements to calibrate the model therefore reduces the uncertainty in parameter estimation. Adding different types of data generally provides more information about the system and, for groundwater flow model calibration, it is important to provide information about flows. Hydraulic heads often do not contain enough information (Hill 2004). To reproduce the observed flow values, not only in magnitude but also in the right direction (flow in or out of boreholes), the hydraulic conductivity must have the right sign (positive). Using flow measurement, and having to reproduce flow magnitude and direction may explain the positive confidence intervals obtained here compared to negative intervals by only using head measurements.

If only deep A-boreholes are considered, the residuals cover a smaller range (Figure 3-25) than in Figure 3-23. However, their distribution is not as good as in the previous results (Figure 3-23). Even if they do not show a specific pattern, they are almost all negative.

Correlation coefficient, objective function, and parameter correlation coefficients for simulation SS23b are summarized in Table 3-8. The parameter correlation coefficients are given as a [5×5] matrix. High correlation is observed when coefficients are higher than 0.95 (USGS 1998). The values listed in the fourth column of Table 3-8 are the lowest and highest coefficients obtained in the matrix. It is obvious that when PFL measurements are considered, it is more difficult to obtain a good fit between observed and measured values (lower correlation coefficient and higher objective function). If prior information is used with hydraulic head measurements only, an extreme correlation between parameters is obtained (high parameter correlation coefficients). This high correlation may cause non unique parameter estimations. In contrast, using prior information with both head and flow measurements lowers the parameter correlation coefficients. Some differences are also observed if measurements in both shallow and deep boreholes are considered or if only deep boreholes are used to calibrate the model. Although it is more difficult to reproduce the flow measurements in both shallow and deep boreholes (higher objective function), using both borehole types as targets for calibration reduces the number of high correlated parameter pairs.

Table 3-8. Calibration results for SS2b3.

Targets for calibration	Correlation coefficient *R*	Objective function *ϕ*	Parameter correlation coefficients *pcc*	Number of *pcc* higher than 0.95
Only heads	0.93	1.73	0.59–0.98	2
Heads and PI	0.96	1.90	0.88–1	20
Heads, PFL values, PI (A and B-boreholes)	0.51	896.6	0.03–0.99	2
Heads, PFL values, PI (only A-boreholes)	0.58	380.5	0.34–0.99	6

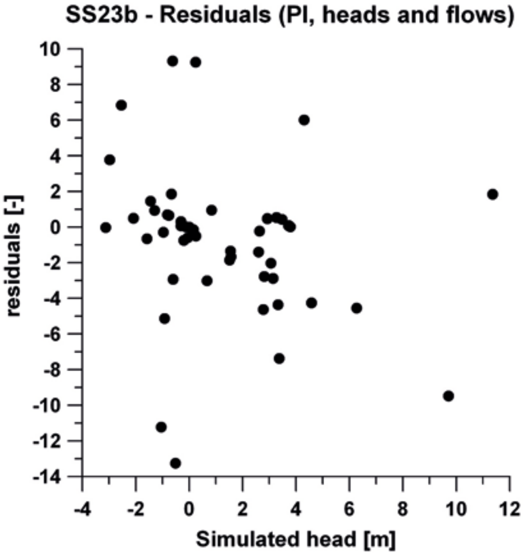

Figure 3-23. *Residuals in simulation SS23: prior information, hydraulic heads and PFL measurements are the targets for calibration (A and B boreholes).*

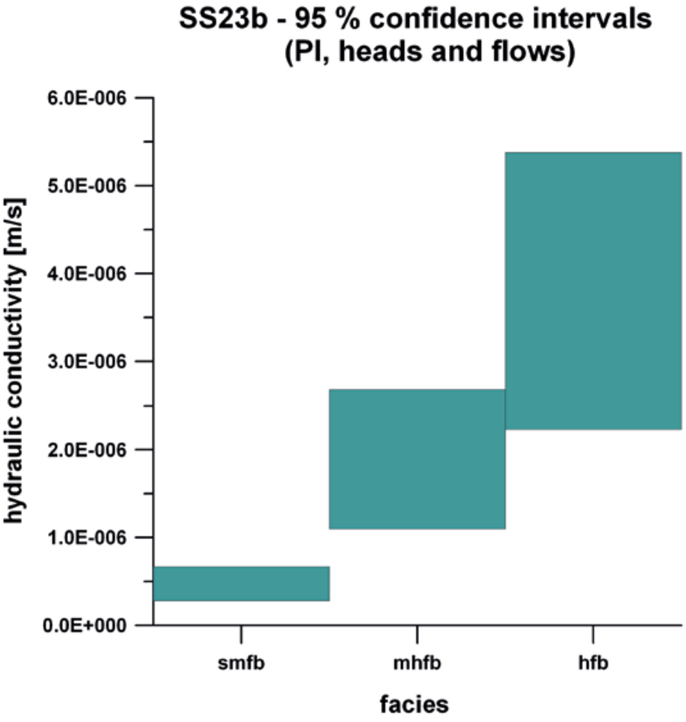

Figure 3-24. *Confidence intervals for K in simulation SS23b: prior information, hydraulic heads and PFL measurements are the targets for calibration.*

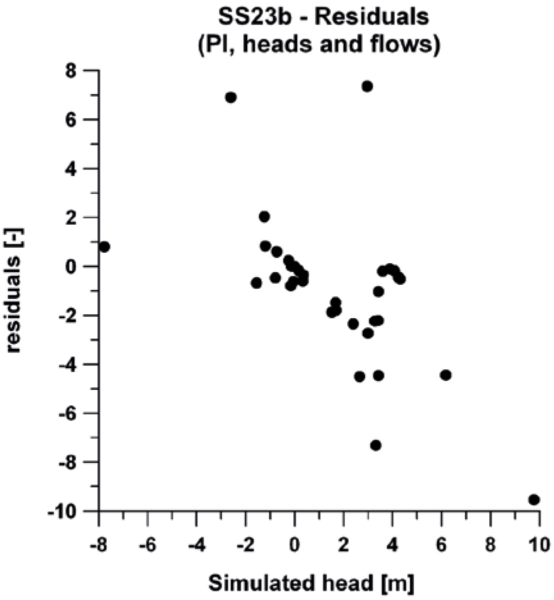

***Figure 3-25.** Residuals in simulation SS23b: prior information, hydraulic heads and PFL measurements are the targets for calibration (only deep boreholes).*

Simulation SS24

Simulation SS24 considers pumping in borehole KR14 and includes packed-off boreholes. Packed-off boreholes are represented by isolated sections in the model, including a total of 28 observation points: four intervals in KR15, two in KR15B, six in KR16, two in KR16B, six for KR17, five for KR18, and two in KR18B, while the last observation point is located at the pumping well.

Without including prior information during parameter estimation, the confidence intervals include negative values, which are unrealistic as previously mentioned. Confidence intervals are, however, narrower compared to those obtained for SS23b. Thus, including more observation points (28 observation points are available here, while only 8 were considered in SS23b) reduces the uncertainty in parameter estimates, as can be seen by comparing Figure 3-21 and Figure 3-26. The lowest objective function obtained for SS24 is 16 and the correlation coefficient is 0.9.

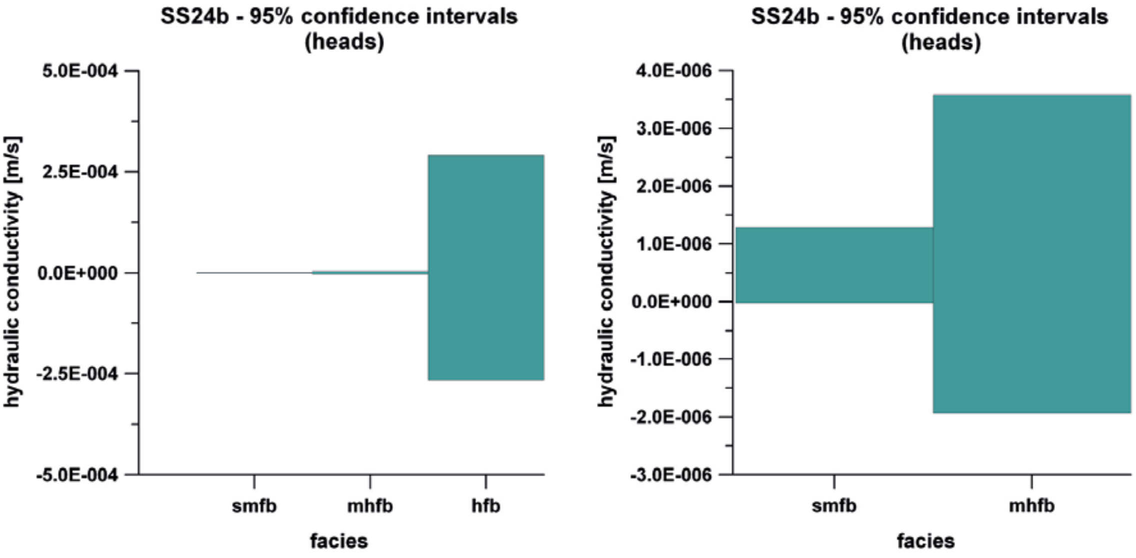

***Figure 3-26.** Confidence intervals for K in simulation SS24b where hydraulic heads are targets for calibration.*

If the same prior information used for SS23 is included in the parameter estimation process for SS24, a similar positive effect is obtained. Adding prior information greatly reduces the width of the confidence intervals and eliminates lower negative bounds (Figure 3-27). The objective function and the correlation coefficient have almost the same values as those obtained without prior information. However, higher parameter correlation coefficients are obtained, as happened with simulation SS23.

Table 3-9, row 3). The residuals, shown in Figure 3-28, have a random distribution, which indicates a good model fit, and they are limited between +1 and −1.5. From these results, it can be stated that the hydraulic response with packed-off boreholes is reproduced quite well with the numerical model.

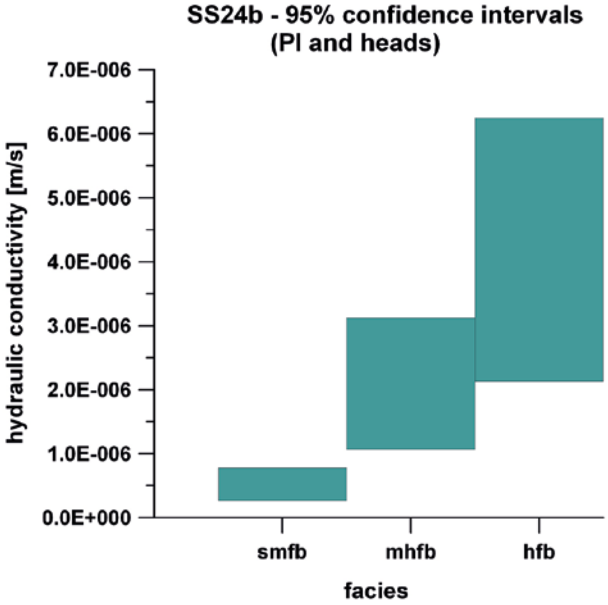

Figure 3-27. Confidence intervals for K in simulation SS24b where prior information and hydraulic heads are targets for calibration.

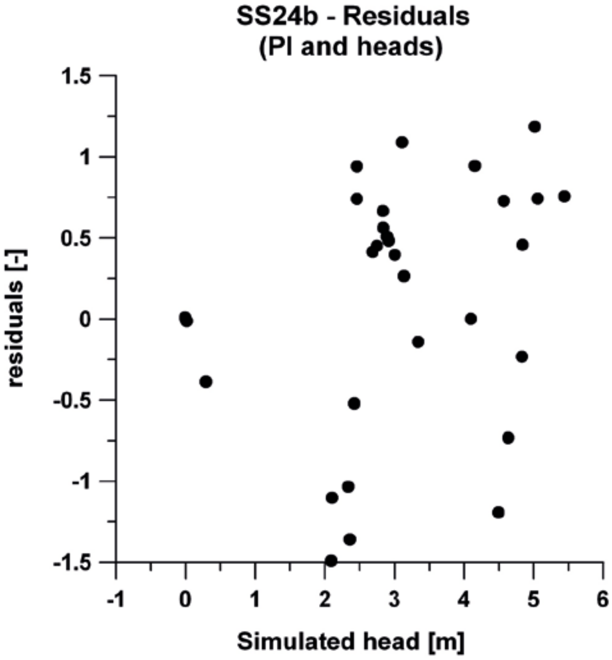

Figure 3-28. Residuals in simulation SS24b where prior information and hydraulic heads are targets for calibration.

Simulation SS25

Fixes heads assigned at the top of the domain limits drawdown during pumping, as explained in Section 3.5.1. The impact of this top boundary condition is evaluated by first assigning and then removing the top boundary condition. Assigning heads at the top boundary produces a hydraulic head at the pumping well of 4.5 m. In contrast, if the top of the domain is considered as no-flow boundary, the hydraulic head decreases to 3.7 m. Moreover, at the observation boreholes, the hydraulic head barely decreases and remain higher than 6 m when the first-type boundary condition is used at the top. In contrast, assigning a no-flow boundary at the top allows heads at that boundary to vary, and the computed drawdown increases at the pumping well as well as at observation boreholes. Therefore, the first-type flow boundary condition is applied only to the lateral boundary of the simulation domain.

Although the pumping rate indicated for SS25 is 5.3 L/min, a value of 7 L/min, which is the value used for simulation SS26, is also used to try to better match simulated and measured drawdown. Results obtained with hydraulic heads as targets for calibration are summarized in

Table 3-9. The larger pumping rate, 7 L/min, results in a smaller objective function. The measured drawdown at the pumping well is 10 m, while simulations never produce a drawdown greater than 8 m when a reasonable good match of drawdown at observation boreholes is maintained. The correlation coefficient does not show a significant difference in the four cases, since its value always is around 0.95.

Table 3-9. Simulation results for SS25b, where hydraulic heads are targets for calibration.

Pumping rate [l/min]	Model	Objective function ϕ	Correlation coefficient R
5.3	Model-1	18.7	0.94
7	Model-1	13.6	0.94
5.3	Model-3	20.7	0.94
7	Model-3	12.4	0.96

PFL measurements are included during calibration by considering a pumping rate equal to 7 L/min with Model-3. The resulting objective function is 2120, with the largest contribution, equal to 1920, coming from the flow observations. Residuals are shown in Figure 3-29. Confidence intervals are shown for two distinct scenarios. In Figure 3-30, the pumping rate is 7 L/min, while in Figure 3-31 a bigger pumping rate (20 l/min) was considered to test the variation of interval width. For the larger pumping rate, the confidence intervals are all positive. Therefore, it seems that not only flow observations contribute to the reduction of parameter uncertainty, but flow magnitude also plays a role in the parameter estimation process.

Simulation SS26

The withdrawal rate from borehole KR18 for simulation SS26 is between 5 and 7 L/min (Klockars et al. 2006). At first, an average value equal to 6 L/min was used for SS26 but, based on the low drawdown simulated, a pumping rate of 7 L/min seemed more appropriate and was used subsequently.

Residuals are shown in Figure 3-32, for a simulation without prior information, and Figure 3-33 when prior information is considered. Prior information reduces the width of the confidence intervals, as can be seen in Figure 3-34. Residuals cover a larger range if prior information is considered (Figure 3-33). However, it should be noted that all residuals are smaller if prior information is considered, except for the hydraulic head at pumping borehole KR18. Therefore, it is quite difficult to reproduce the proper behaviour in the pumping well, as it has already been observed in simulation SS25.

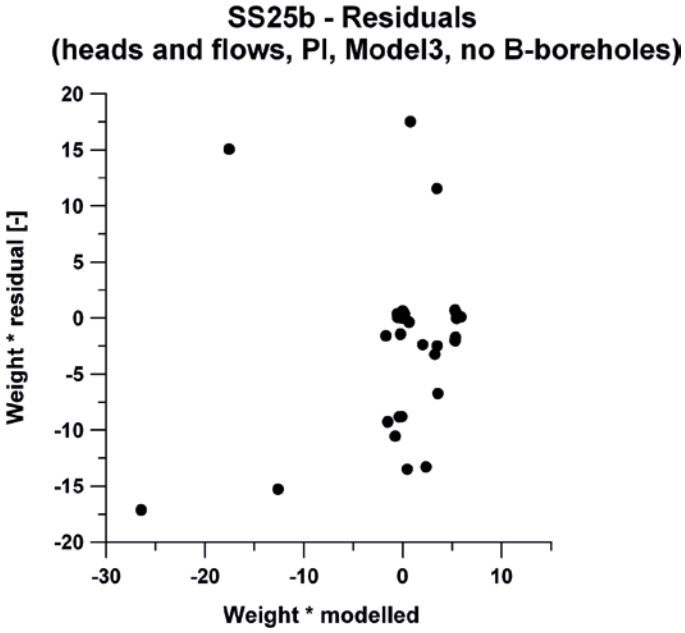

Figure 3-29. *Residuals in simulation SS25b where prior information, hydraulic heads and PFL measurements are targets for calibration.*

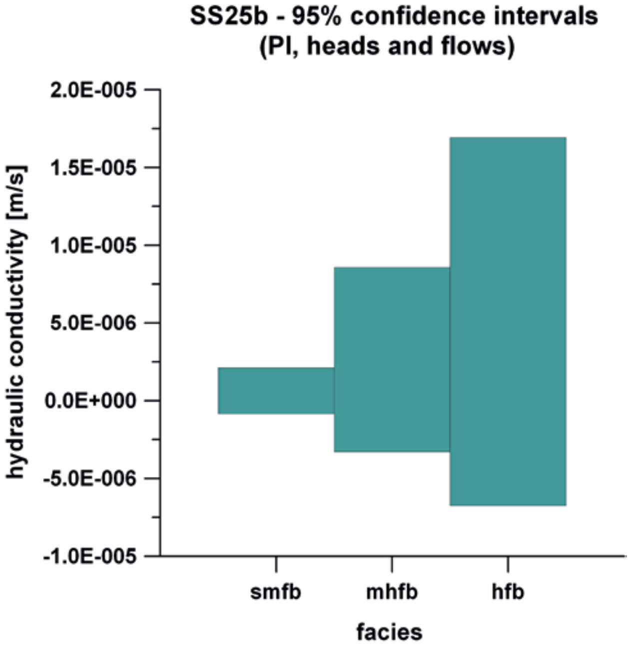

Figure 3-30. *Confidence intervals for K in simulation SS25b where prior information, hydraulic heads and PFL measurements are targets for calibration.*

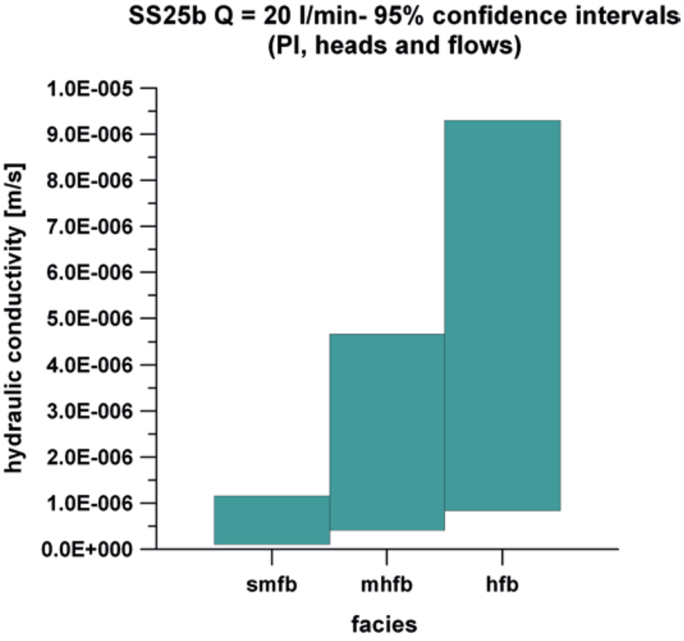

***Figure 3-31.** Confidence intervals for K, for simulation SS25b with pumping rate Q = 20 L/min: prior information and where hydraulic heads and PFL measurements are targets for calibration.*

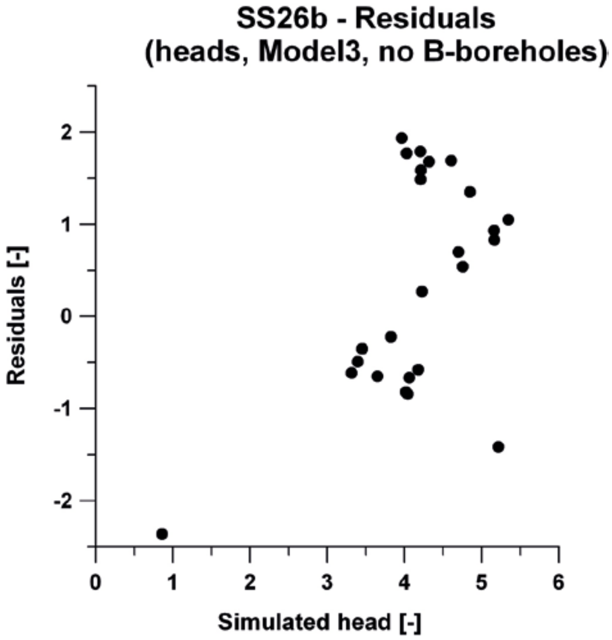

***Figure 3-32.** Residuals in simulation SS26b where hydraulic heads are targets for calibration.*

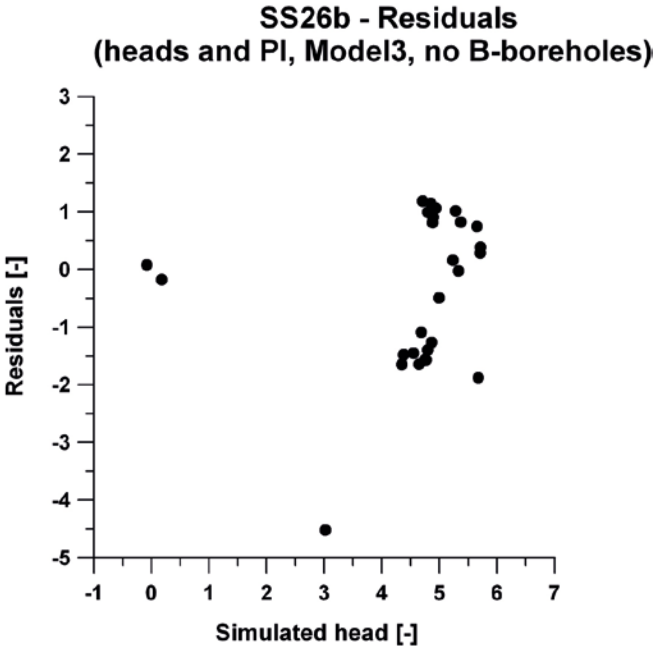

Figure 3-33. *Residuals in simulation SS26b where prior information and hydraulic heads are targets for calibration.*

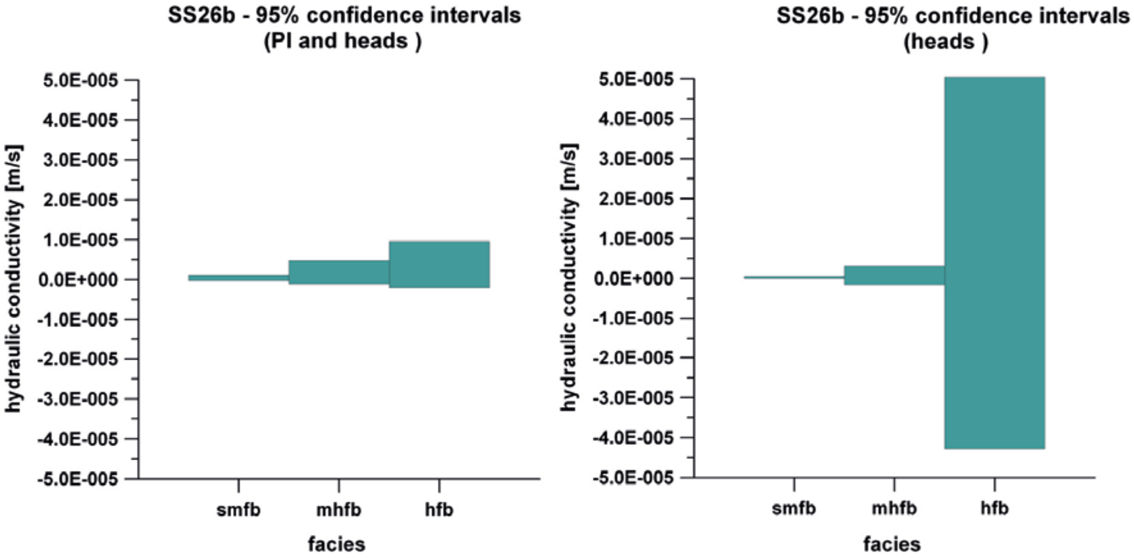

Figure 3-34. *Confidence intervals for K in simulation SS26b: prior information and hydraulic are targets for calibration (left); only heads are targets (right).*

Conclusion on steady state simulations

Estimated conductivity values are presented in Table 3-10, together with the value of the objective function. In simulations SS21 and SS22, only hydraulic heads are considered as calibration targets. PFL measurements and prior information have been considered to calibrate the model during pumping, when stronger hydraulic responses are simulated. Therefore, the estimated hydraulic conductivity values for the first two simulations (SS20 and SS21) have very large confidence intervals and are likely less representative than hydraulic conductivities obtained for pumping simulations.

When PFL measurements are included in the calibration, the objective function is larger. In fact, it is much more difficult to reproduce flow values than hydraulic heads, as flows have a larger variability and are more sensitive to the fractured rock representation. In addition, it should be kept in mind that PFL measurements are available for borehole intervals that are 2 m long, while the spatial resolution of the numerical model is 5 m. Therefore, measured flow values at neighbouring intervals were added and attributed to the nearest mesh node. Note that the observation weights for flow measurements are 0.1, as explained in Section 0.

In simulation SS23b_PI_flow_A, only PFL measurements in deep A-boreholes are considered as targets for calibration, as they are the required performance measures. In contrast, simulation SS23b_PI_flow_AB considers both deep and shallow B-boreholes. Although objective function ϕ is larger for SS23b_PI_flow_AB, the residuals seem to be better distributed around zero than for SS23b_PI_flow_A. Moreover, the confidence intervals are narrower if both A and B-boreholes are considered. Therefore, increasing the number of flow observations reduces the uncertainty of the estimated parameters. In simulation SS25b, increasing the pumping rate in borehole KR18 from 5.3 L/min to 7 L/min produces a better match between measured and simulated heads, and the objective function ϕ decreases from 20.9 to 12.4. A pumping rate equal to 7 L/min has therefore been used for simulation SS25b_Q7_PI_flow, as done for SS26b. The objective function for SS25b_Q7_PI_flow is higher than that for SS23b_PI_flow_A. Additional simulations show that, if the withdrawal rate from borehole KR18 is increased, a better match is obtained (lower objective function in SS25b_Q20_PI_flow) and confidence intervals are entirely in the range of positive hydraulic conductivity values (Figure 3-31).

Table 3-10. Estimated facies hydraulic conductivity and objective function value.

Simulation	SMFB [m/y]	MHFB [m/y]	HFB [m/y]	Ø
SS21	5	100	120	0.07
SS22	20	77	335	6.4
SS23b_PI	17	67	134	1.9
SS23b_PI[1]_flow[2]_A	20	79	160	381
SS23b_PI[1]_flow[2]_AB	15	63	120	897
SS24b	20	25	400	15.7
SS24b_PI	16	66	132	17.5
SS25b_Q5.3	5	25	120	20.9
SS25b_Q7[3]	5	25	125	12.4
SS25b_Q7[3]_PI[1]_flow[2]	20	83	160	2119
SS25b_Q20[3]_PI[1]_flow[2]	20	80	160	1245
SS25b_Q5.3_5zones	5	25	250	5
SS25b_Q5.3_5zones_PI[1]_flow[2]	16	63	125	2326
SS26b	8	25	120	36.8
SS26b_PI[1]	15	60	120	52.4

[1] PI: prior information.
[2] Flow: PFL measurements used as targets for calibration.
[3] Q: withdrawal from borehole KR18 (7 and 20 l/min, respectively).

This simulation illustrates how the pumping rate may affect the model outcome. Instead of increasing the pumping rate, which is not a valid option based on the available pumping test information, a fifth fractured rock zone is introduced. This zone is characterized by a lower hydraulic conductivity around borehole KR18 and the simulation is called SS25b_Q5.3_5zones (Table 3-10). It is thus assumed that there are some uncertainties on the facies distribution around borehole KR18, contributing to the overestimation of the hydraulic conductivity for this portion of the bedrock. These last simulation results for SS25 are encouraging and they prove that a lower hydraulic conductivity around KR18 should be considered, since a better match is obtained with the actual pumping rate equal to 5.3 l/min.

Adding prior information for simulations SS24b and SS26b with packed-off boreholes reduces the confidence intervals for the estimated parameters, as expected. A very large reduction is observed for K_{HFB}, which is the facies that always show an extremely large interval if only hydraulic heads are used as targets for calibration. However, the objective function value for SS26b_PI, with prior information, is greater than for SS26b without prior information. It is also the case for SS24b and SS24b_PI, even if the difference in the objective function is much smaller.

Scenario SS23b has also simulated using only flow observation for inverse modeling. In this case, all weights are equal to 1, since all observations are of same type. Measured versus simulated values are shown in Figure 3-35, where the largest flux corresponds to the pumping borehole KR14. Residuals show a satisfactory distribution (Figure 3-36). Confidence intervals still have a negative lower bound, but their size is smaller than that obtained using only hydraulic head measurements as targets for calibration. However, the simulated hydraulic heads are too low compared to those observed; the simulated drawdown is about 13 m at pumping borehole KR14 and it is between 7 and 9 m at observation boreholes. All these simulated values are larger than the measured drawdown, which is 6 m at borehole KR14 and between 3 and 5 m at observation boreholes. These results suggest both hydraulic head and flow measurements be considered for inverse modeling to better represent the system and its behaviour.

Observation sensitivities show how simulated head and flow values are sensitive to parameter variations. As an illustration, observation sensitivities for SS23b_PI_flow_AB are presented (Figure 3-37). Among head observations (highlighted by the red rectangle in Figure 3-37), the most sensitive is the observation point located at pumping borehole KR14, as expected. In general, flow observations are more sensitive than head observations, except for two flow observations in KR16 that show the lowest sensitivity values, 30 and 50, respectively. The highest sensitivity is found at borehole KR15B, which has a value of about 20 000. B-boreholes allow for the characterization of the groundwater flow field near the surface and are not required as flow performance measures, but their hydraulic response is sensitive to the variation of facies hydraulic conductivity.

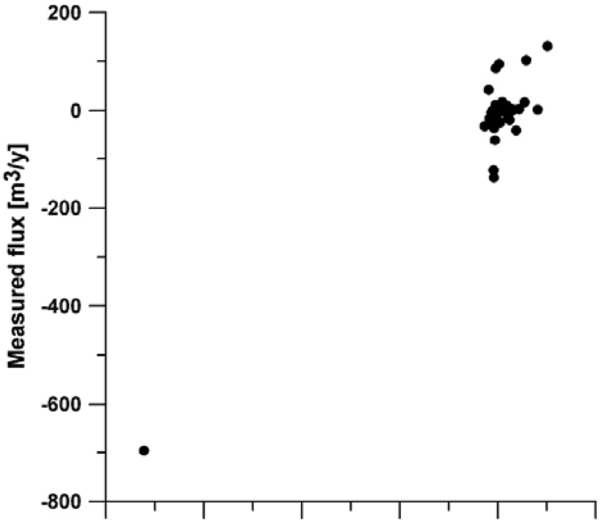

Figure 3-35. *Simulated versus measured flow values for simulation SS23b.*

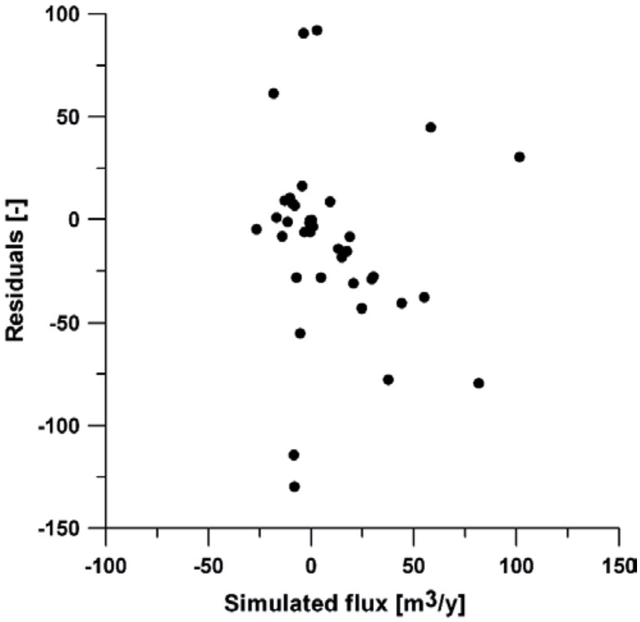

Figure 3-36. *Residuals in simulation SS23b where only flows are considered as targets for calibration.*

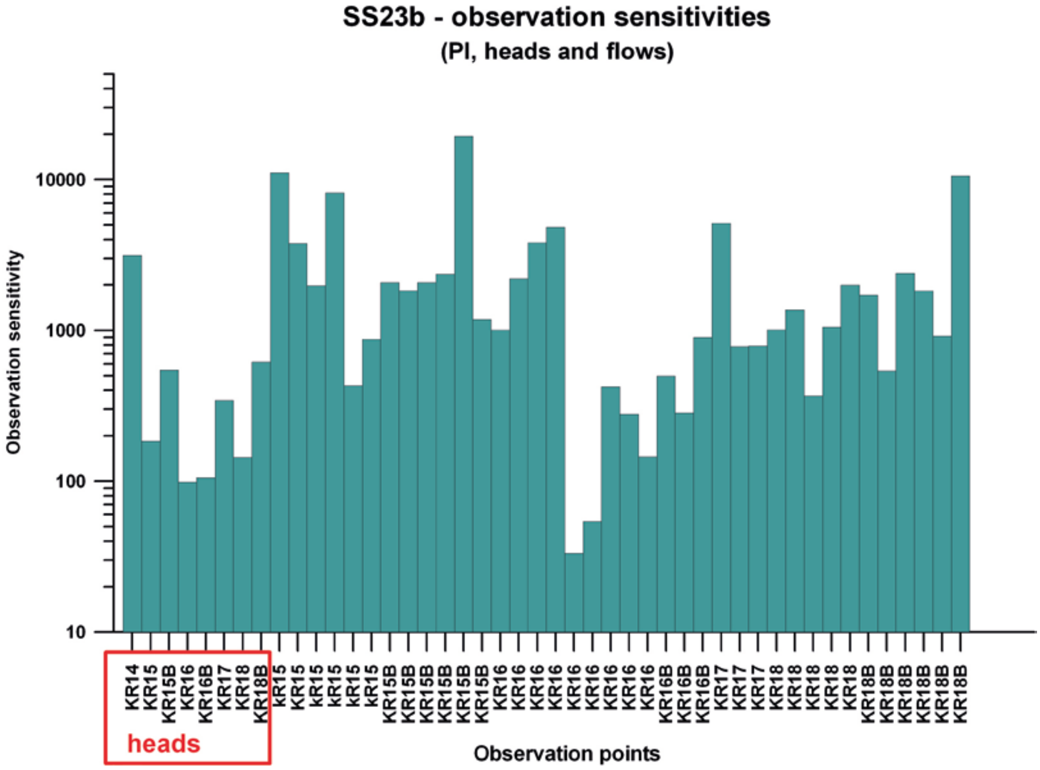

Figure 3-37. *Sensitivities of head (identified with the red rectangle) and flow observations for simulation SS23b_PI_flow_AB.*

The relative composite sensitivity of a parameter gives a measure of the changes in model outputs that are incurred by a fractional change in the value of the parameter, as explained previously. As an illustration, parameter sensitivities are shown for simulations SS23B_PI_flow_AB and SS25b_Q7_PI_flow (Figure 3-38). The sensitivity of fracture apertures is smaller than that of the facies hydraulic conductivity. Relative sensitivities are presented, which allows comparing the effects that different parameters have on the parameter estimation process when parameters are of different type, and possibly of very different magnitudes, such as hydraulic conductivity and fracture aperture.

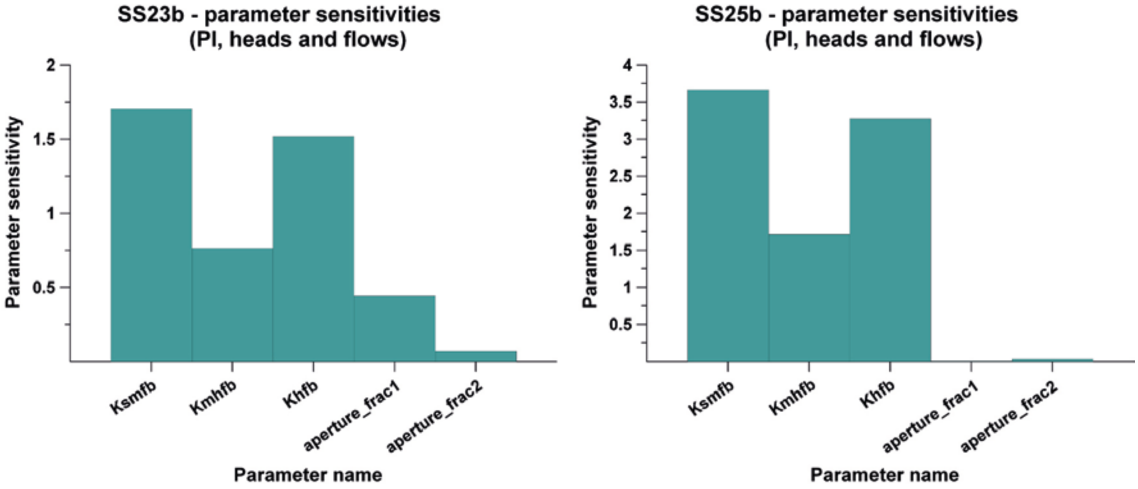

Figure 3-38. *Parameter sensitivities for simulations SS23b/SS25b.*

Comparing the two simulations shows that fracture apertures have higher sensitivity when borehole KR14 is pumped, and that their sensitivity is almost zero when borehole KR18 is pumped. These results confirm the observations shown previously, where the fit between observed and simulated heads did not show large difference between Model-1 and Model-3 for simulation SS25, since the same correlation coefficient was obtained. Thus, numerical results are less sensitive to the variation of fracture apertures for SS25 than for SS23.

Simulation SS25 has also considered a fixed aperture. Fixed parameters do not take part in the optimisation process, at the risk of degrading the optimization process (Doherty 2004). Using a fixed aperture during calibration does not produce differences in the estimated parameter values, but the optimization is faster. Only 28 model calls are required when the aperture parameters are fixed, while 72 calls were required when the optimization of aperture parameters was included.

Some final comments concern the use of prior information. Although its use reduces the width of the confidence interval, higher parameter correlation coefficients are obtained. As a result, parameters may not be estimated uniquely, which may be verified by executing the same calibration using different initial estimates and observing how the estimated hydraulic conductivity values change. Slight changes may be observed, but the new estimated values remain in the same confidence interval, which is supposed to include the true parameter with a probability of 95%.

If prior information is not considered, the parameter correlation coefficients are significantly lower and the estimated parameter values do not change if initial parameter estimates are varied, as shown in Table 3-11. Simulation SS23B has been used to test the influence of initial estimates. Only flow observations from A-boreholes are considered. When no prior information is used, the same estimates are obtained (SS23B_1), regardless of the initial values. In contrast, if prior information is considered, the estimated values may change and may depend on the initial estimates (SS23B_2_PI). The parameter correlation coefficients also show a great difference: high correlation is obtained if prior information is used, while low correlation, and thus probable unique estimates, is observed without using prior information. These behaviours indicated that prior information should be used carefully.

Simulation TS27

Simulation TS27 is a transient simulation of pumping at borehole KR15. Initial heads are those computed from simulation SS21. Instead of assigning a withdrawal rate at the pumping well, the hydraulic head is specified based on the observed drawdown, which is equal to 10 m, and the initial hydraulic head, which is calculated in simulation SS21. The minimal hydraulic head based on drawdown is assigned at borehole KR15 for the first 10 days, to simulate pumping. The drawdown and recovery simulated at observation boreholes are presented in Figure 3-39. The largest simulated drawdown is at borehole KR18, while the smallest in at KR16B, with a difference of more than 1 meter.

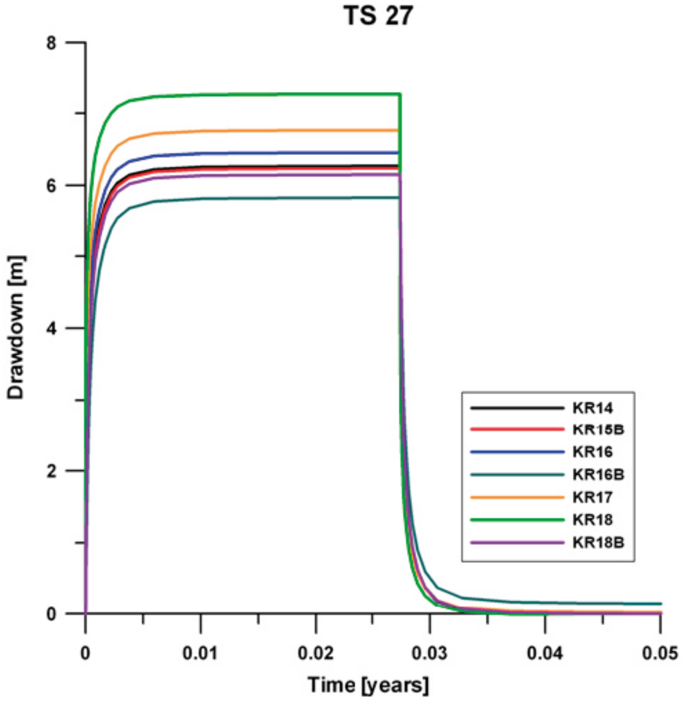

__Figure 3-39.__ Drawdown at observation boreholes during pumping in KR15.

Table 3-11. Influence of initial parameter values on estimated parameter values.

Simulation	SMFB [m/y]	MHFB [m/y]	HFB [m/y]	Max *pcc*
SS23B_1				
Initial values	7	40	150	
Estimated values	15.5	47.7	120	0.57
SS23B_1				
Initial values	18	90	125	
Estimated values	15.3	43.1	120	0.49
SS23B_2_PI				
Initial values	7	40	150	
Estimated values	14.9	59.7	120	0.99
SS23B_2_PI				
Initial values	15	60	250	
Estimated values	20	79.7	160	0.99

Borehole flow distributions have also been evaluated, as required in the performance measures. Flow variation indicated as Δflow in Table 3-12 is calculated with reference to the natural undisturbed condition with open boreholes, simulated in SS21.

Simulation TS28

Simulation TS28 refers to pumping tests with transverse flow measurements carried out between July 2007 and April 2008. Transverse flow measurements were conducted in boreholes KR15, KR15B, KR16B, KR17B and KR18B. Difference flow measurements were conducted in boreholes KR14, KR15, and KR15B. Only the transverse flow measurements in KR15 are considered here as performance measures, as indicated in Table 3-13 (Väisäsvaara 2009).

Initial heads are those produced by simulation SS21. Instead of assigning a withdrawal rate at the pumping well, the hydraulic head is specified based on the observed drawdown, which is equal to

Table 3-12. Calculated borehole flow distributions for TS27.

Z (m) mah	Flow [ml/hr]	∆flow [ml/hr]	Comment
KR14			
30	1461.1	1421.8	SMFB facies
40	54.4	63.0	
50	590.9	604.0	
80	−1339.8	−1452.7	SMFB and MHFB facies
35	16 969.8	18 282.8	fracture
KR15			
60	57 144.9	51 762.2	fracture
75	61 386.2	61 456.7	SMFB facies
KR16			
50	−3940.5	−5071.9	
60	−3311.5	3418.8	fracture
70	−2.1	−10.2	SFB facies
80	−205.4	−211.3	SFB facies
90	−1581.1	−1595.2	
150	331.2	302.4	SFB facies
KR17			
50	−2422.7	−2594.2	
70	848.9	1029.1	
130	277.7	308.1	SFB facies
135	1096.2	1134.4	SFB facies
KR18			
55	−3607.7	−3640.4	
65	−373.3	−388.1	SFB facies
80	−862.8	−825.0	

Table 3-13. Information on transverse flow measurements in borehole KR15.

Drillhole	Date	Activity	Pumped borehole	Drawdown (m)	Selected fracture (m)
KR15	2008-01-15 2008-01-17	Transverse flow measurements	KR14	6	72.3
KR15	2008-01-17 2008-01-22	Transverse flow measurements	KR14	6	125

6 m. This drawdown is subtracted from the initial head to calculate the minimum hydraulic head at borehole KR14, which is assigned for the first 24 hours. After that, recovery at neighbouring boreholes is simulated. The drawdown and recovery simulated at observation boreholes are presented in Figure 3-40. The biggest simulated drawdown is in borehole KR18B, while the smallest one in KR16, with a difference of about 2 meters.

Transverse flow measurements were conducted in borehole KR15 during the pumping. Flow at 59 mah is required as one of the performance measures. The nearest computed value is 119 L/d, which is located at the 60 mah. In Model-3, discrete fracture Plane-1 is located at this depth, while the performance measure is referred to fracture HZ19C, which is one of the major fracture zones considered in Task 7A. Thus, fracture HZ19C is replaced at this block-scale by Plane-1, according to Model-3. Computed flows at depths of 70 m and 125 m (Table 3-14) are 22 L/d and −12 L/d, respectively. A positive value represents flow from the borehole to the hydraulic zone and a negative value is for flow in the opposite direction. Thus, in borehole KR14, the flow is always negative during the first 24 hours, during pumping. After about 1.5–2 hours, the flow reaches a stationary value. At depths of 60 mah and 70 mah, the initial conditions are re-established after 3.7 days, while at 125 mah, the recovery of the initial flow value is much faster (24.1 hour) and then inversion in the flow direction is observed. No information on the flow direction, which is required in the performance measures, is provided by the numerical code. The simulated drawdown at borehole KR15 after 24 hours of pumping is 3.1 m.

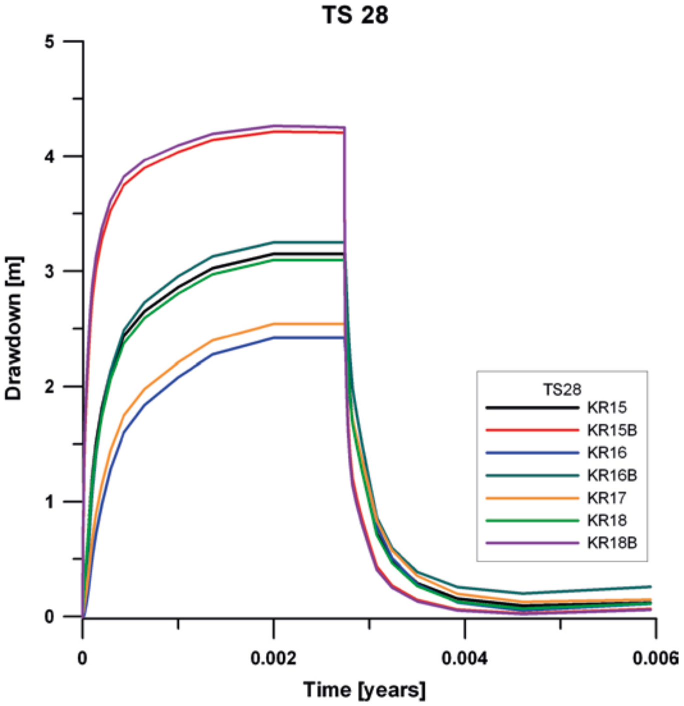

__Figure 3-40.__ Drawdown at observation boreholes during pumping in KR14.

Simulations PA20C and PA29

Performance Assessment simulations PA20C and PA29 are conducted with the HydroGeoSphere travel time probability package, which allows simulating groundwater age and life expectancy based on reservoir theory (Cornaton and Perrochet 2006, Cornaton et al. 2008, Therrien et al. 2009). This approach has been used for Task 7A.

Groundwater age at a given location is the time of travel of groundwater from an inlet boundary to the location, while the groundwater life expectancy is the time of travel from the location to an exit boundary. Life expectancy is therefore zero at an outlet and equal to the transit time at an inlet. In contrast, age is zero at an inlet and equal to the transit time to an outlet. The numerical model finds the zero age zones, which correspond to the outlet for the backward problem. The backward-in-time model is then used to evaluate the life expectancy probability density function. Life expectancy is considered as a main safety indicator for subsurface waste repositories (Cornaton et al. 2008). Life expectancy of particles released from the indicated start points was thus evaluated here.

Boundary conditions are those specified for simulation SS20a, without boreholes in the simulation domain. The difference between simulations PA20C and PA29 is represented by the facies hydraulic conductivity values and the presence of the two discrete fractures. The hydraulic conductivity of the facies considered for PA29 is the average of the estimated values from SS21 to SS26.

The goal of the PA simulations is to identify the pathways from the release points listed in Table 3-14. Nine observation points are located between coordinates 1525800–1525900 and 6792400–6792500 for the x and y directions, respectively. They are all located at a depth of 100 m. The release points are located in the zone shown by the red arrow in Figure 3-41, together with four slices showing the facies distribution in that area.

A first pathway computation is based on the particle tracking capabilities of Tecplot, as done for PA simulations in Task 7A. With this method, only the advective component of the transport mechanism is considered. In contrast, with the HydroGeoSphere travel time probability package, diffusion and dispersion through the porous rock matrix are also considered. The Tecplot particle paths computed for PA20C are shown in Figure 3-42. The particle released from RP1 will have not reached the lateral boundary after 20 years, while those released from RP9, which is located 100 m north of RP1, will have reached the boundary after 20 years.

Table 3-14. Particle release points for simulations PA20C and PA29.

Startpoint	X [m]	Y [m]	Z [m]
RP1	1 525 800	6 792 400	−100
RP2	1 525 800	6 792 450	−100
RP3	1 525 800	6 792 500	−100
RP4	1 525 850	6 792 400	−100
RP5	1 525 850	6 792 450	−100
RP6	1 525 850	6 792 500	−100
RP7	1 525 900	6 792 400	−100
RP8	1 525 900	6 792 450	−100
RP9	1 525 900	6 792 500	−100

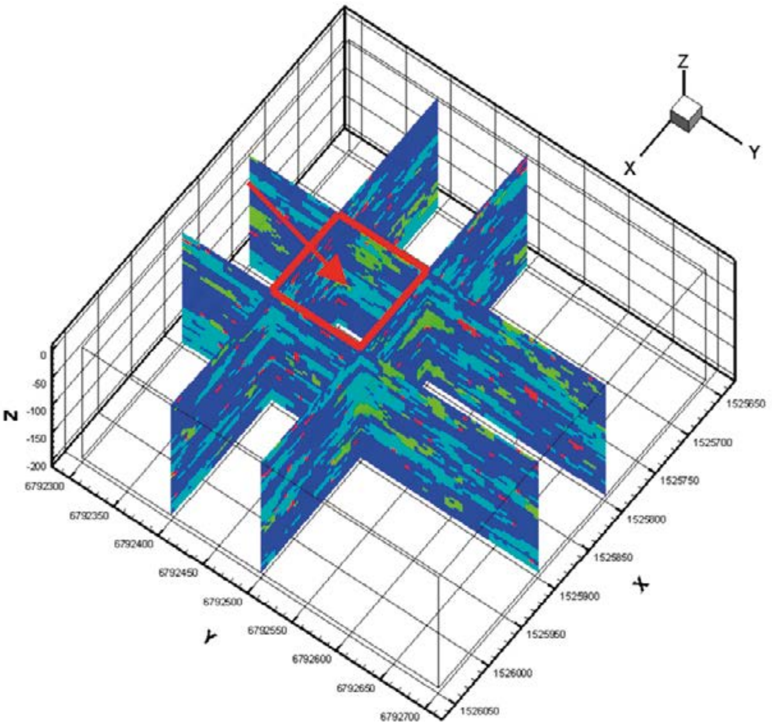

Figure 3-41. Location of the particle release points for simulations PA20C and PA29.

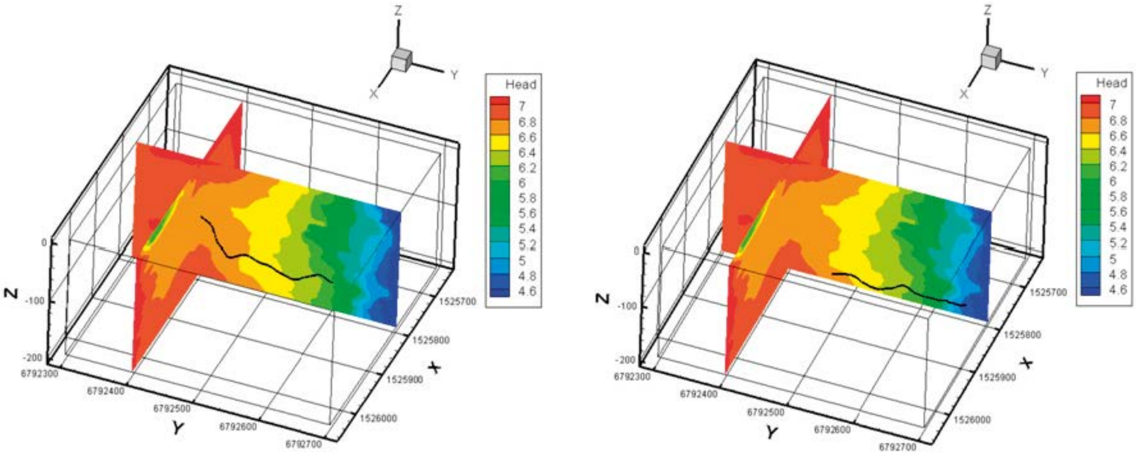

Release point RP1 **Release point RP9**

Figure 3-42. Tecplot particle tracking: RP1 and RP9 after 20 years.

Probability density function (pdf) and cumulative density function (cdf) for life expectancy computed with HydroGeoSphere are the curves presented in Figure 3-43. Release point RP9 has the highest pdf, while RP1 the lowest. Moreover, the peak in the pdf curves is reached at different times, depending on the release point location. Three groups of curves may be identified: the first one has a peak after about 15 years, the second one after 25 years and the last one after 45 years. Finally, simulation PA29 provides lower peaks than those obtained in PA20C, since in the initial model (PA20C) the hydraulic conductivities were overestimated. Observation of the cdf curves for PA20C shows that, after 20 years, there is a probability of about 60% that a particle released from RP9 will have reached an outflow boundary, while a particle released from RP1 has a probability lower than 5%. These probabilities are smaller in PA29. In contrast, the particle paths computed with Tecplot show that, after 20 years, the particle released from RP9 will have reached the boundary, since the diffusion and dispersion through the porous rock matrix were neglected.

The flow across a box inside the modelled volume is also computed, as suggested in the performance measures. The motivation for that calculation is that borehole-based measures will be strongly influenced by the calibration approaches (and hence may result in very similar values between different models), while the predicted flow distribution within the background rock is likely to highlight the differences between models. Six planes are considered and each plane is subdivided into sub-faces (Figure 3-44 and Figure 3-45).

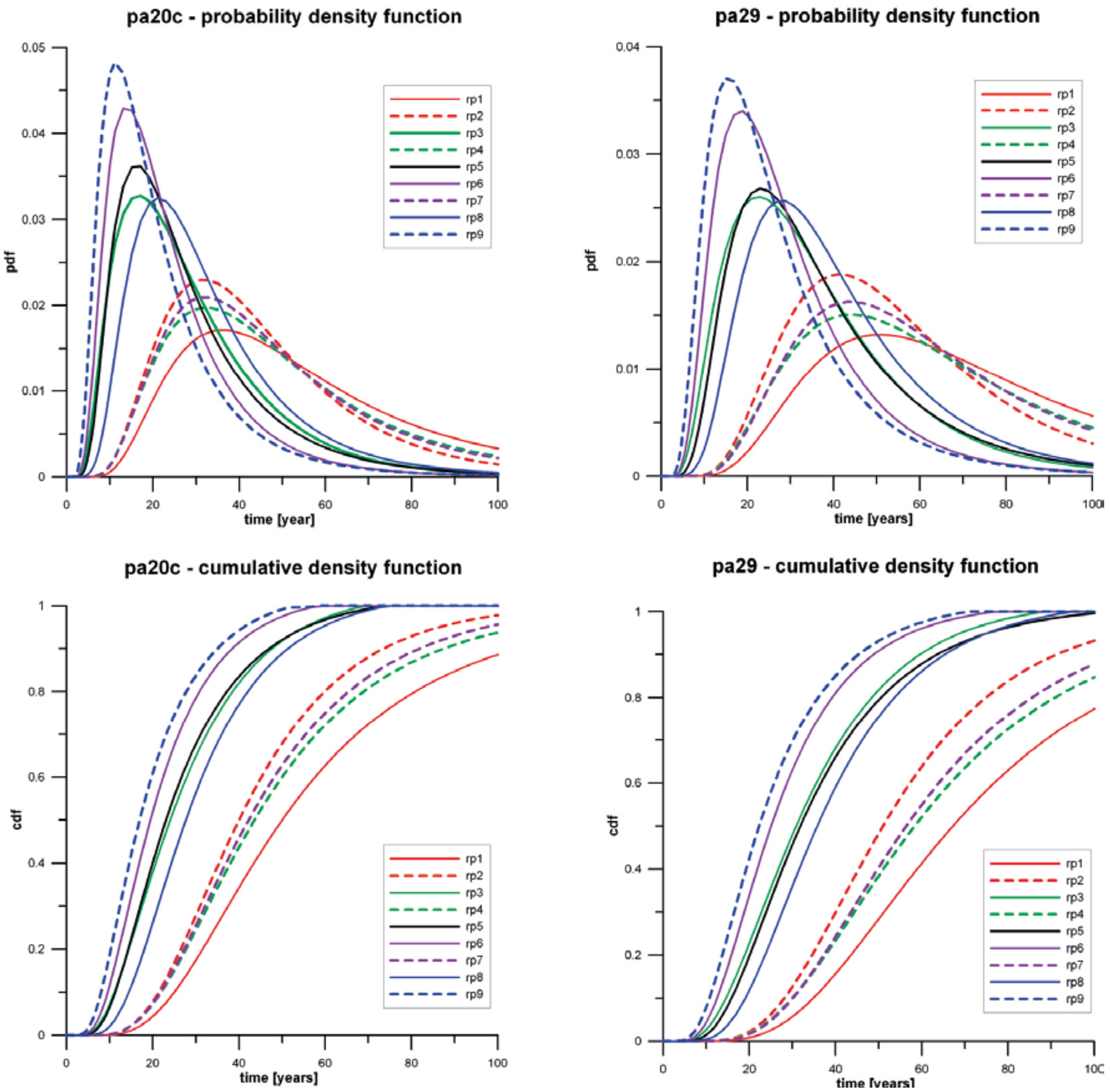

__Figure 3-43.__ Probability density function (pdf) and cumulative density function (cdf) for life expectancy computed at the release points.

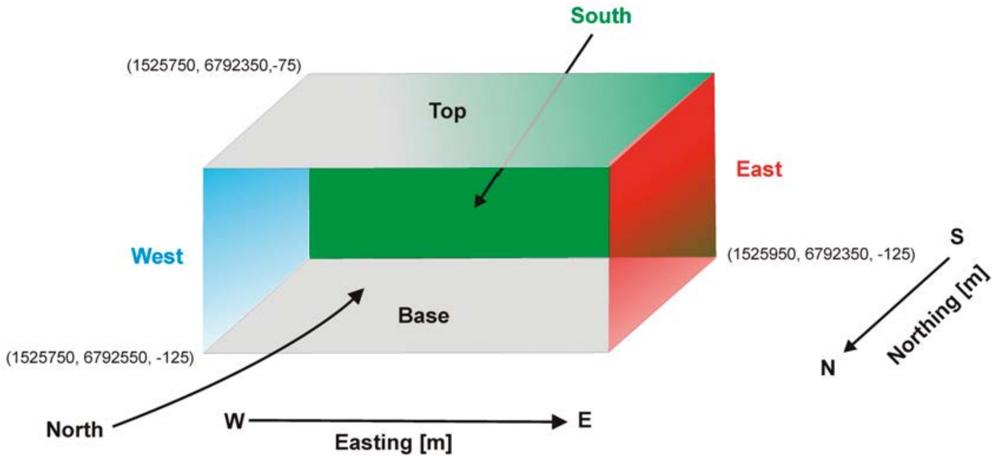

Figure 3-44. *Design of the six planes (north, east, south, west, top and bottom) considered for computing flow distribution within the rock.*

Flow +ve into box (PA29)

Measurement Plane	Number of subrectangles	Tot Q (m^3/s)	Min Q (m^3/s)	Max Q (m^3/s)
Top	16	-5,8E-08	-8,0E-07	5,3E-07
Base	16	2,1E-06	-1,8E-07	3,6E-07
West	8	3,6E-06	1,1E-07	9,0E-07
East	8	1,6E-06	-3,1E-07	4,2E-07
South	8	8,3E-07	5,5E-09	3,0E-07
North	8	-8,3E-06	-3,8E-06	-2,9E-07

Figure 3-45. *Flow computed across the six planes.*

3.6 Conclusion

The main goal of Task 7B was to perform inverse modelling of simulations SS21, SS23, SS24, SS25, and SS26 to provide calibrated models and parameter estimates. As a result, reduction of uncertainty in the properties of the fracture network and Posiva Flow Log data assessment constituted the main topics of numerical result interpretation.

Upper and lower bounds were supplied for adjustable parameters (facies hydraulic conductivity and fracture apertures). This information is essential for inverse modelling, since it informs PEST of the range of permissible values that a parameter can take (Doherty 2004). In addition, prior information, which is based here on realistic ratios between facies hydraulic conductivities, was introduced to constrain the parameter estimates. Hydraulic heads and PFL measurements were used as targets for calibration.

The facies distribution should provide the appropriate hydrogeological representation of the fractured rock, regardless of what kind of stress is applied, such as pumping or natural groundwater flow. The hydraulic responses to pumping in borehole KR14 and KR18 is different. The hydraulic response observed during pumping in borehole KR14 is reproduced quite well by the numerical model. In contrast, the drawdown simulated in borehole KR18 is always lower than that observed, even using lower hydraulic conductivity values than those for the simulation of pumping in borehole KR14. The match between observed and simulated hydraulic response can only be improved by increasing the withdrawal rate at borehole KR18. The difficult in matching the hydraulic response during pumping at KR18 may be caused by an inaccurate representation of the fractured rock facies around borehole KR18 or by some hydraulic feature that cannot be captured by the conceptual models tested here. A variable aperture may be more appropriate for fracture KR14_4H, which intersects both boreholes KR14 and KR18. In fact, the aperture estimated for SS23 is larger than what is estimated for SS25. This fracture is perhaps less transmissive at the intersection with borehole KR18 than at the intersection with borehole KR14.

PFL measurements were useful for model calibration. In fact, it is better to calibrate a groundwater model using both hydraulic heads and flows. A large variation of flow values is often observed at locations separated only by few meters, making it difficult to reproduce these values with numerical simulations that are based on a continuum representation of the porous medium, as opposed to a discrete fracture network approach. However, including flow observations as targets for calibration allows for a better interpretation of inverse modelling results, since more residuals are analyzed and different observation types provide more information about the system behaviour. The number of observations influences the confidence interval size, as shown by Vecchia and Cooley (1987), who obtained an increase in interval size as the number of observations decrease. In most practical cases, the number of parameters that can be uniquely estimated is much smaller than the number of observations comprising the calibration dataset due to the limited information content of most such datasets (Moore and Doherty 2005). Moreover, adding different types of data generally provides more information about the system and, in particular, it is important to provide information about flows in groundwater flow model calibration. Hydraulic heads seldom contain enough information, as indicated by the frequency with which extreme values of parameter correlation coefficients occur when using only hydraulic heads (Hill 2004). Thus, the width of linear confidence intervals for estimated parameters, and thus the parameter uncertainty, is reduced here by including PFL measurements as targets for calibration. It is however important to adjust observation weights to different observation types, to make the contribution to the objective function from each observation group similar in magnitude.

The use of prior information helps to constrain the hydraulic conductivity, and reduces the uncertainty on the parameter estimates. However, this procedure increases the parameter correlation coefficients, which will then indicate a possible lack of unique parameter estimates.

The modeling work conducted here demonstrates that for an exhaustive characterization of hydrogeological systems, the number and type of available measurements have a direct influence on inverse modeling results. In particular, the PFL tool provides very useful data that must be considered for model calibration. Fracture data along borehole cores also constitute suitable data to exploit for the characterization of fractured rock using geostatistical approaches, which do not require building extremely complex DFN models.

4 Task 7C

Task 7C focused on groundwater flow in low-transmissivity fractures identified during construction of the three ventilation shafts of the ONKALO underground research laboratory (Vidstrand et al. 2015). The goal of Task 7C was to develop a near-field single-fracture scale model incorporating essential micro-structural information. This model should help assess flow patterns on shaft walls, transport characteristics by F-factor predictions, and flow distribution within a fracture (Vidstrand et al. 2015). The task did not address effects of shaft wall Excavation Damage Zone (EDZ) and unsaturated conditions, nor effects due to grouting of investigation boreholes. Consequently, the fractures selected were chosen in the region least disturbed by grouting and construction.

Three fractures deemed important for performance assessment were identified through field investigations. These fractures, Fracture1, Fracture2 and Fracture3, whose transmissivities are approximately 1×10^{-9}, 1×10^{-10}, and 1×10^{-11} m^2/s, have undergone limited characterization using conventional hydrogeological test methods (Vidstrand et al. 2015). Although Fracture2 and Fracture3 were mapped and measured in shaft KU2, they were not considered in Task 7C (Vidstrand et al. 2015). Fracture1 was the only fracture crossing the three shafts considered for modeling. It was mainly characterized with Posiva Flow Log (PFL) measurements conducted in 2008 in the ONK-PP drillholes.

The task was subdivided into subtasks 7C1, 7C2, and optional subtask 7C3. The objective of Subtask 7C1 was to provide a microstructural model for fracture roughness and aperture distribution, while the objective of SubTask 7C2 was to simulate the single-hole and cross-hole interference tests conducted in the ONK-PP drillholes. The optional Subtask 7C3 concerned a nappy experiment conducted into the exhaust air shaft. The purpose of that experiment was to measure the leakage distribution in fractures using water absorptive nappies (disposable diapers). There was no protocol developed for the test and it was therefore purely experimental (Vidstrand et al. 2015).

4.1 Site description

A small rock volume at a depth of about 250 m in the Olkiluoto bedrock was the region of interest of Task 7C. This volume is centered at UTM coordinates Easting 1 525 915 meters and Northing 6 791 990 meters, around the three main shafts of the ONKALO underground research laboratory. Eleven drillholes were drilled inside the diameter of the future shafts and were identified by the acronym ONK-PP. They had a length of 100 m and were drilled vertically from rock caverns at level −180 m along the main tunnel of ONKALO (Figure 4-1). Boreholes KR24, KR38, and KR48 were also located inside the circumference of future shafts KU1, KU2, and KU3, respectively (Figure 4-2). The characteristics of the shafts and drillholes are listed in Table 4-1.

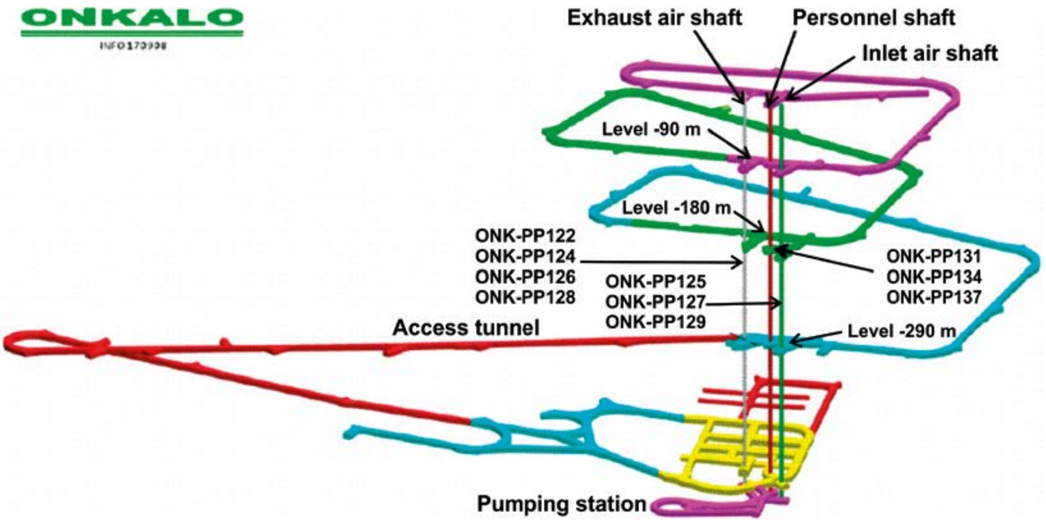

Figure 4-1. *ONKALO layout showing drillholes, shafts and tunnel (modified from Pekkanen 2009).*

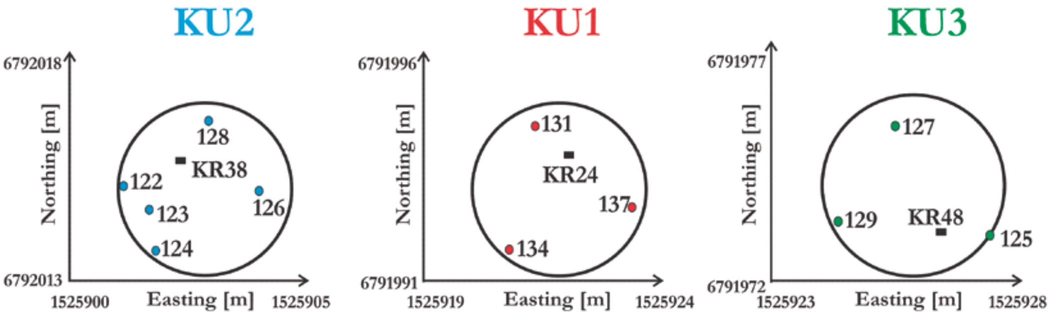

Figure 4-2. *Location of ONK-PP drillholes and KR boreholes inside shaft diameters.*

PFL single-hole and cross-hole measurements were conducted in ONK-PP drillholes during the Spring and Autumn 2008 (Table 4-1). After all PFL measurements were taken, the drillholes were injected with a concrete mix (Pekkanen 2009a). The inlet and exhaust air shafts and the personnel shaft were then successively raise-bored to a depth of −290 m (Figure 4-1).

PFL flow measurements, borehole TV-images, and drilled cores allowed the identification of a series of fractures intersecting the drillholes. Focus is here on the characterization of Fracture1 (FR1), which was assumed to cross the three shafts at the depth of about −250 m (Figure 4-3). This fracture was assumed to be horizontal, but its exact geometry and location did not have to be precisely known for the modelling objectives of task 7C. Since the magnitude of flow rates measured at drillhole-fracture intersections was highly variable, a variable fracture aperture was assumed in the model.

Table 4-1. Characteristics of shafts and drillholes.

Shaft name	KU1	KU2	KU3
Shaft function	Personnel	Exhaust air	Inlet air
Shaft diameter	4.5 m	3.5 m	3.5 m
Shaft center Northing coordinate	6 791 993 m	6 792 015 m	6 791 974 m
Shaft center Easting coordinate	1 525 922 m	1 525 903 m	1 525 925.5 m
Period of PFL measurements	March 2008	February 2008	September–October 2008
ONK-PP drillholes	131, 134, 137	122, 123, 124, 126, 128	125, 127, 129
KR borehole	KR24	KR38	KR48
Z coordinate, top of drillhole (m.a.s.l.)	−177.52	−181.09	−176.81

4.1.1 Posiva Difference Flow: measurements in drillholes

The Posiva Difference Flow method (PFL DIFF) uses a flowmeter that incorporates a flow guide for relatively quick determinations of hydraulic conductivity and hydraulic head in fractures/fractured zones in cored drillholes (Figure 4-4). Unlike conventional drillhole flowmeters, which measure the total cumulative flow rate along a drillhole, the PFL DIFF probe measures the flow rate into or out of defined drillhole sections (Pekkanen 2009a). The measured section is isolated with rubber disks pressed against the borehole wall and flow is measured by following a heat pulse emitted by a heating element and detected by side thermistors. The flow guide of the PFL DIFF probe encloses an electrode for single point resistance measurement (SPR). SPR is lower for a fracture where flow is detected, although many other resistance anomalies result from other fractures and geological features (Pekkanen 2009a). Flow rate and SPR measurements were used to locate flowing fractures along ONK-PP drillholes.

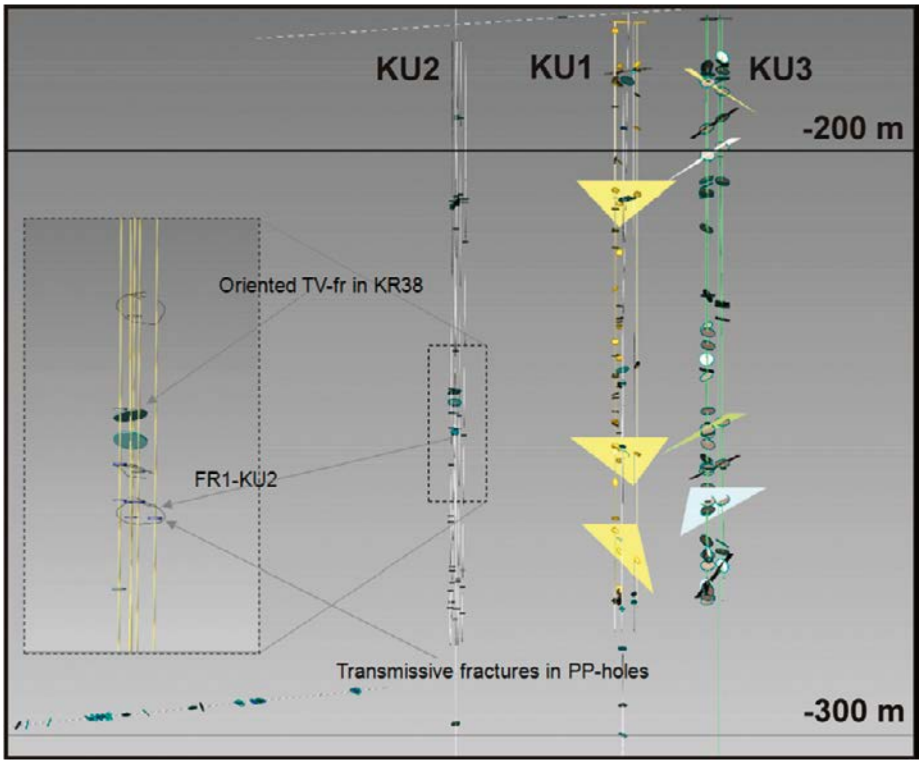

***Figure 4-3.** Example of fracture data available along the three shafts: Fracture1 is indicated as FR1 in shaft KU2 (from Task 7C data delivery).*

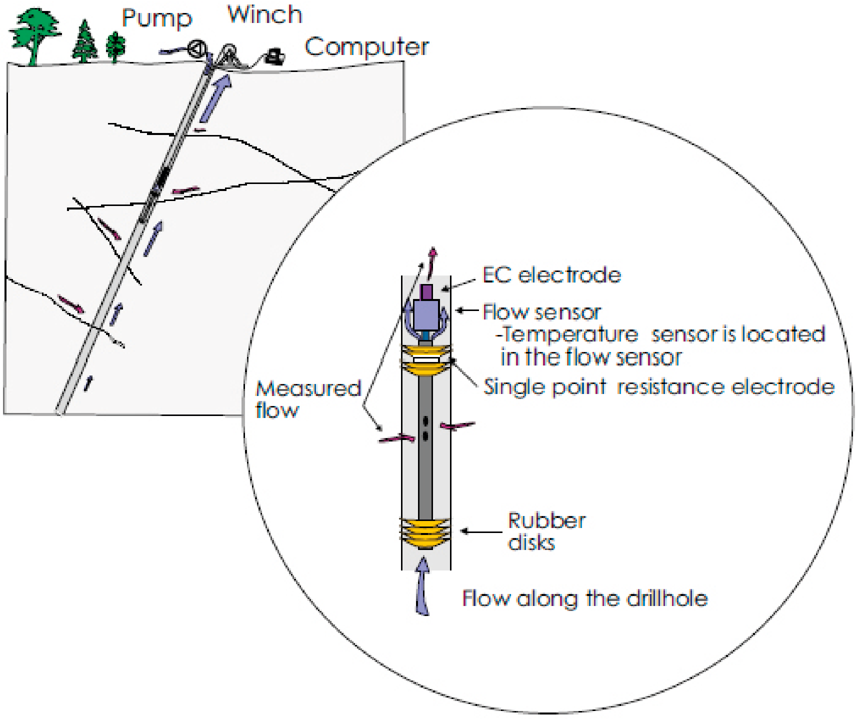

***Figure 4-4.** Schematic of the probe used in the PFL DIFF (Pekkanen 2009a).*

During the first series of PFL measurements, in February 2008, the monitored drillholes were ONK-PP122, ONK-PP123, ONK-PP124, ONK-PP126, and ONK-PP128, while in the second series period in March 2008, drillholes were ONK-PP131, ONK-PP134 and ONK-PP137 (Pekkanen 2009a). In September – October 2008, additional hydraulic tests were conducted in drillholes ONKPP-125, ONK-PP127, and ONK-PP129 (Pekkanen 2009b). The PFL measuring section was 0.5 m and a 0.1 m point interval or measurement increment was used, such that overlapping sections were measured. This type of measurement is called the detailed flow logging mode and uses overlapping test sections to allow for precise identification of the depth of hydraulically conductive fractures along a borehole.

The measured drillholes were open and there was natural outflow from the boreholes into the surrounding fractures during the measurements. The surrounding drillholes were closed with packers during single-hole measurements. In contrast, during cross-hole hydraulic interference tests, the measurements were conducted in ONK-PP125 and ONK-PP127 with the surrounding drillholes either open or closed, using different combinations. The test included monitoring of pressure and outflow in drillholes.

4.2 Subtask 7C1: Single fracture modeling

The aperture spatial distribution for Fracture1 was modelled with the random field generator FGEN (Robin et al. 1993), which generates compatible files for the HydroGeoSphere numerical code (Therrien et al. 2009) used here for groundwater flow and transport simulations. FGEN is based on an algorithm that produces random fields of real variables by the inverse Fourier transform and spectral analysis. The two main input data for FGEN are the mean and variance of the logarithmic distribution of the field, which is here represented by the fracture aperture. Another essential input parameter is the correlation length of the random field to be modeled, which can be anisotropic.

Fracture transmissivities were estimated from PFL measurements conducted in the ONK-PP drillholes considering Thiem's formula, as described by Pekkanen (2009a):

$$s = h - h_0 = \frac{Q}{2\pi T} \ln \frac{R_0}{r_w} \tag{4-1}$$

where s is drawdown, h the hydraulic head in the drillhole, Q the outflow at the drillhole, T the transmissivity of the medium, R_0 the radius of influence, and r_w the radius of the drillhole. If two flow rate measurements corresponding to two distinct hydraulic heads are available, then the undisturbed (natural) hydraulic head and the transmissivity of the drillhole sections tested can be calculated (Pekkanen 2009a).

A drawdown of about 190 m was assumed considering the undisturbed average hydraulic head at ground surface (6 m a.s.l.) and the level at the top of drillholes, located at about −180 m a.s.l. Since the radial distance R_0 to the undisturbed hydraulic head h_0 was not known, a value of 500 for the ratio R_0/r_w was selected (Pekkanen 2009a). Based on these assumptions and on the flow rate Q measured with the PFL probe, the transmissivity of drillhole sections could be estimated. Nevertheless, some fracture-specific results were classified as "uncertain". Some possible causes for this uncertainty were the roughness of the drillhole wall, solid particles such as clay or drilling mud in the water, gas bubbles entrained in the water, and high flow rates along the drillhole. Moreover, since the actual flow geometry and any skin effects were unknown, transmissivity values should only be considered as an indication of the prevailing orders of magnitude (Pekkanen 2009a).

Fracture apertures were calculated from transmissivities assuming the validity of the cubic law (Table 4-2). The computed average and variance of the logarithm of hydraulic aperture were −11.54 and 0.273, respectively.

Table 4-2. Fracture1 transmissivity values and calculated aperture.

Fracture1 observation	T [m²/s]	Flow [ml/h]	Aperture 2b [m]	ln(2b)
KU1_onkpp134	5.5E−10	367	9.18E−06	−11.60
KU2_onkpp124	4.2E−09	2870	1.81E−05	−10.92
KU2_onkpp123	1.4E−09	961	1.26E−05	−11.28
KU2_onkpp122	1.5E−09	996	1.27E−05	−11.27
KU2_onkpp126	4.3E−09	2930	1.82E−05	−10.91
KU2_onkpp128	1.1E−09	761	1.16E−05	−11.36
KU3_onkpp127	2.0E−10	135	6.55E−06	−11.94
KU3_onkpp129	9.5E−11	63	5.11E−06	−12.18
KU3_onkpp125	5.7E−11	38	4.31E−06	−12.35

The correlation length generally depends on the scale considered. It can be estimated by computing the variogram of the fracture aperture. However, in this case, there were not enough data points to obtain a meaningful variogram. In the absence of data to compute the correlation length, a literature review was conducted. Relevant information is reported in Table 2-3. The most relevant reference is the report written by Gelhar (1987) for the Swedish Nuclear Fuel and Waste Management Company (SKB). Gelhar (1987) described field tracer tests in crystalline rocks conducted in Sweden and Canada. For these tests, the correlation length for the logarithm of the aperture varied from 0.2 to 1.2 meters. This range of values was assumed to be appropriate to characterize Fracture1 at the scale of interest of Task 7C.

Table 4-3. Correlation length literature review.

Reference	Correlation length (λ) information
Neuman (2005)	Asperities and fracture apertures delineate random fractals, whose variance and spatial correlation scale increase with fracture size.
Brush (2003)	For a single natural fracture contained in a 1 m × 0.7 m × 0.7 m quarried block of granite, λ_x=43 mm and λ_y=21 mm.
Nicholl et al. (1999)	For 15×30 cm synthetic fractures, λ=0.08 cm.
Hakami and Larsson (1996)	For a core (Φ=190 mm, length 410 mm) from Aspo, λ= 1 cm.
Kueper and McWhorter (1992)	Correlation length expressed as fraction of the domain size, generally λ < 1 m.
Poon et al. (1992)	The correlation length is proportional to the cut-off length.
Tsang et al. (1988)	Ratio correlation length/channel length = 0.1, 0.2, 0.4.
Gelhar (1987)	Correlation scales for logaperture ranges from 0.2 to 1.2 m. Values from field tracer tests.
Brown et al. (1986)	Correlation lengths for two natural joints are on the order of a few millimetres.
Brown and Scholtz (1985)	Correlation lengths: 1 mm, 1 cm, 10 cm, 1 m, 10 m. For “mated” joints, commonly observed in the field, the correlation distance is typically less than 1 cm. For faults, however, the correlation distance may be large.

A few values for the correlation length were tested to provide preliminary indication of the influence of correlation length on simulated flow rates at drillhole-Fracture1 intersections. The correlation lengths considered were 0.2, 0.35, and 0.5 meters (Figure 4-5). The smallest value was established on the basis of mesh resolution constraints, since mesh nodal spacing had to be smaller than the correlation length to generate an accurate random field. In particular, a reasonable choice is to select a nodal spacing that produces several estimation points per correlation length (Robin et al. 1993). Moreover, drillholes were fairly close to each other, in particular in shaft KU2, such that the mesh had to be fine enough in the x and y directions to allow for the discretization of separate drillholes.

To preserve the random aperture generated with FGEN, the same mesh nodal spacing in the x and y directions was used with HydroGeoSphere (Table 4-4). The vertical nodal spacing was uniformly doubled from 0.125 m close to Fracture1 until a maximum nodal spacing of 2 m was reached. Since high mesh resolution is only required along the fracture plane, the vertical variable node distribution specified reduced model size and, thus, model run time.

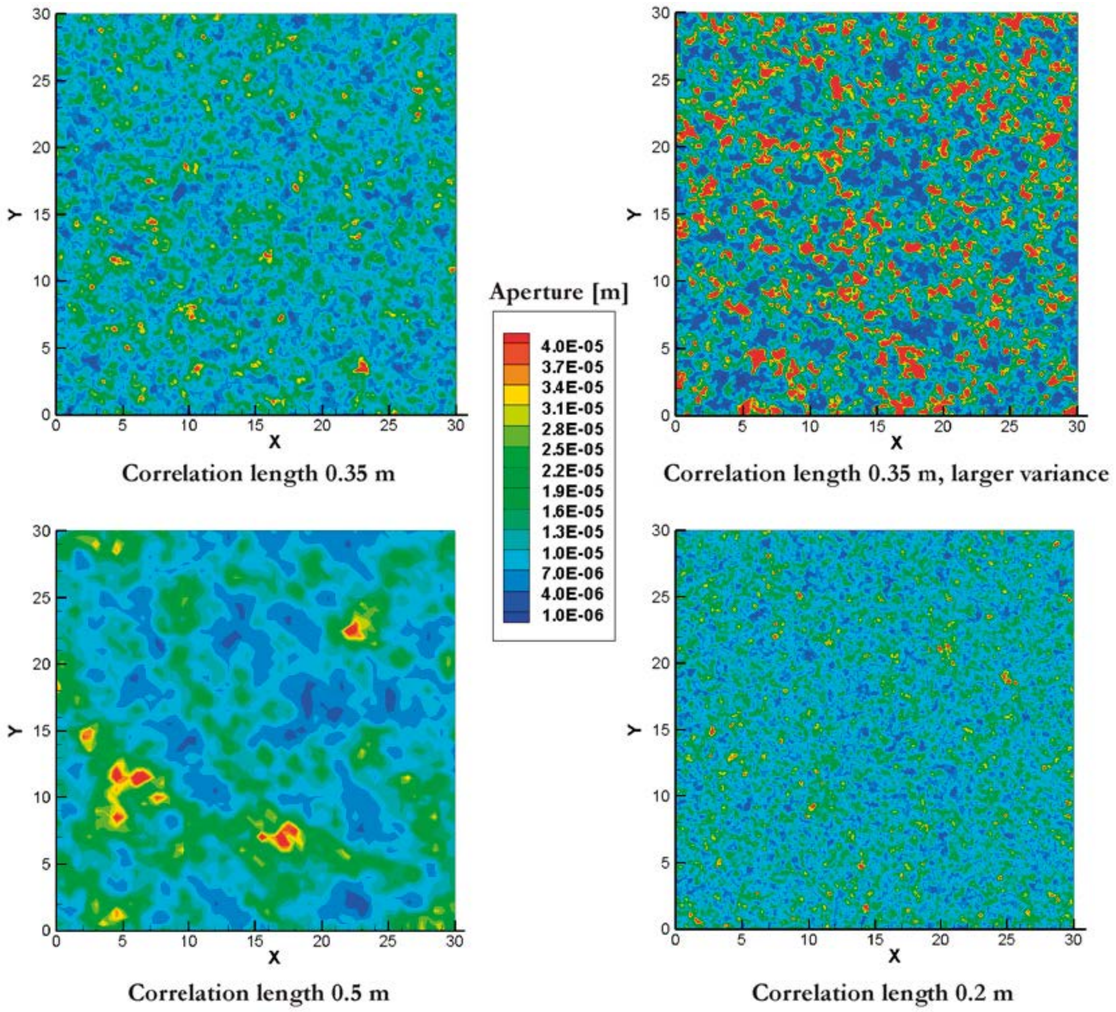

Correlation length 0.35 m

Correlation length 0.35 m, larger variance

Correlation length 0.5 m

Correlation length 0.2 m

***Figure 4-5.** Different random field generations for the aperture of fracture1.*

Table 4-4. Meshes tested for different aperture correlation length λ.

Horizontal nodal spacing [m]	Vertical nodal spacing [m]	λ [m]	Number of elements
0.1	From 0.125 to 1	0.2	2 160 000
0.15	From 0.125 to 1	0.35	1 840 000
0.2	From 0.5 to 2	0.5	1 035 000

An attempt to include the roughness in the conceptual model was made by considering the relation presented by Louis (1969):

$$K = \frac{g(2b)^2}{12\upsilon}\cdot\frac{1}{\left[1+8.8\left(\frac{r_a}{4b}\right)^{1.5}\right]} \tag{4-2}$$

where the ratio $r_a/4b$ is the relative roughness that can be estimated from the joint roughness coefficient JRC and the effective physical aperture E, such as given by Barton and de Quadros (1997):

$$\frac{r_a}{4b} = \frac{JRC^{3.5}\cdot L}{800\cdot E^2} \tag{4-3}$$

Since the effective physical aperture was not determined for Fracture1, the hydraulic aperture estimated from the cubic law was considered appropriate for flow modeling purposes of Task 7C. That assumption is valid for a ratio $r_a/4b < 0.033$ and for laminar flow conditions (Barton and de Quadros 1997).

4.3 SubTask 7C2: groundwater flow simulations

Performance measures for Task 7C2 include pressures and flow rates for each of the simulated PFL logs and F-factor calculations (Vidstrand et al. 2015). Performance measures related to retention properties defined by the F-factor are defined following the definitions of Task 6D (Hodgkinson 2007).

Standard PFL logs, or single-hole PFL, and special PFL logs, or cross-hole PFL (with adjacent open holes) are the simulation scenarios. Simulations are listed in Table 4-5, where the letter "s" stands for single-hole tests and letter "c" stands for cross-hole tests. Drillholes are either open or closed. Under open conditions, water from drillholes flows freely into the main tunnel located at the top of the drillholes. Closed drillholes have a packer sealing their top such that flow is inhibited towards the main tunnel. Closed drillholes does not, however, mean that different sections along the borehole are isolated.

Open boreholes, where the PFL probe was installed and flow measured, were represented in the numerical model by wells with a specific flow rate. In contrast, closed boreholes were represented by wells with a zero flow rate. Specific head may also be assigned to drillholes to represent flow towards open drillholes, but here it was preferred to set a flow rate. Flow rates were given by Pekkanen (2009a, b) and defined as pumping rates. Note that a difference exists between the total outflow from drillholes, which was measured approximately half an hour after the drillholes were measured with the PFL probe, and the sum of single PFL measurements. This difference may be caused by leakage across the rubber disks of the PFL probe or from the installation of the probe itself, since it was not physically possible to measure the last 2–3 meters of drillholes (Pekkanen 2009). This difference is defined as relative deviation and it is represented as a percentage later in this report.

Although drillholes were 100 m deep, the suggested vertical dimension for the simulation domain was 40 m (Vidstrand et al. 2015). The domain dimensions were thus 40 m and 30 m, in the vertical and lateral directions, respectively. Horizontal Fracture1 was located in the middle and crossed the whole domain. Three distinct setups were considered (Figure 4-6), one for each shaft. No-flow boundary conditions were set to the top and bottom of the simulation domain, while a constant hydraulic head of 270 m was set to the lateral boundary. Shafts were not explicitly discretized in the numerical model.

Table 4-5. Simulations of single-hole and cross-hole tests.

Name	Boreholes
s-PP122	Borehole PP122 open and PFL measured Boreholes PP123, PP124, PP126, PP128 closed
s-PP123	Borehole PP123 open and PFL measured Boreholes PP122, PP124, PP126, PP128 closed
s-PP124	Borehole PP124 open and PFL measured Boreholes PP122, PP123, PP126, PP128 closed
s-PP126	Borehole PP126 open and PFL measured Boreholes PP122, PP123, PP124, PP128 closed
s-PP128	Borehole PP128 open and PFL measured Boreholes PP122, PP123, PP124, PP126 closed
s-PP131	Borehole PP131 open and PFL measured Boreholes PP134, PP137 closed
s-PP134	Borehole PP134 open and PFL measured Boreholes PP131, PP137 closed
s-PP137	Borehole PP137 open and PFL measured Boreholes PP131, PP134 closed
s-PP125	Boreholes PP125 open and PFL measured Boreholes PP127, PP129 closed
s-PP127	Boreholes PP127 open and PFL measured Boreholes PP125, PP129 closed
c-PP125-1	Boreholes PP125 open and PFL measured Boreholes PP127, PP129 open
c-PP125-2	Boreholes PP125 open and PFL measured Boreholes PP127 open, Borehole PP129 closed
c-PP125-3	Boreholes PP125 open and PFL measured Boreholes PP127 closed, Borehole PP129 open
c-PP127-1	Boreholes PP127 open and PFL measured Boreholes PP125, PP129 open
c-PP127-2	Boreholes PP127 open and PFL measured Boreholes PP125 open, PP129 overpressure 2bar
c-PP129-1	Borehole PP129 open and PFL measured Boreholes PP125, PP127 open

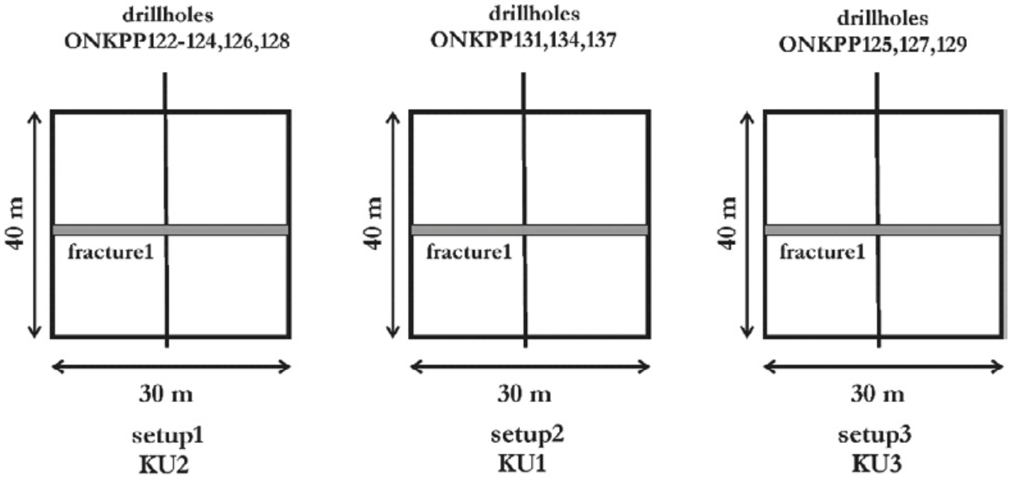

***Figure 4-6.** Simulation setup for single-hole and cross-hole interference tests.*

Besides Fracture1, which was assumed to cross all three shafts, a few minor discrete fractures were included in the conceptual model (Table 4-6, Table 4-7, and Table 4-8). Their depth and aperture were given by Pekkanen (2009a, b). The rock matrix was considered as a porous medium with low hydraulic conductivity. Different values, based on porous rock hydraulic conductivity values established in Task 7A and ranging between 1×10^{-9} m/s and 1×10^{-12} m/s were tested. By manual calibration, a value equal to 1×10^{-11} m/s was chosen as the most appropriate. The resulting conceptual model for simulation setup1 is shown in Figure 4-7.

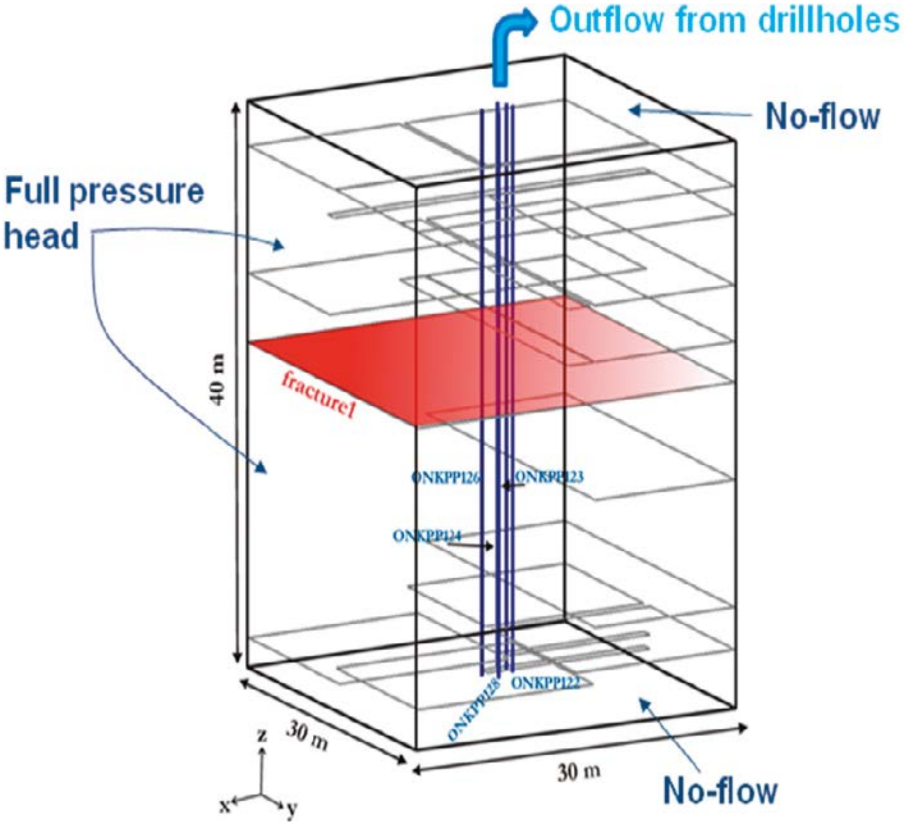

***Figure 4-7.** Simulation domain for setup1 showing drillholes, fractures and boundary conditions.*

Table 4-6. Fractures in setup1 (KU2).

	Drillholes					**Aperture [mm]**	**Depth [m]**
	122	**123**	**124**	**126**	**128**		
Fracture	**Fracture1**					**Variable**	−250
	f2					8×10^{-3}	−241
	f3					1.6×10^{-2}	−245
	f4					7×10^{-3}	−254
	f5					5×10^{-3}	−264
			f6		f6	6×10^{-3}	−241
		f7	f7		f7	7×10^{-3}*	−245
					f8	5×10^{-3}	−236
			f9			5×10^{-3}	−243

*Average aperture (from three drillhole values).

Table 4-7. Fractures in setup2 (KU1).

	Drillholes			**Aperture [mm]**	**Depth [m]**
	131	**134**	**137**		
Fracture	**Fracture1**			**Variable**	−250
	f2			8×10^{-3}	−238
		f3		7×10^{-3}	−240
			f4	4×10^{-3}	−233

Table 4-8. Fractures in setup3 (KU3).

	Drillholes			**Aperture [mm]**	**Depth [m]**
	125	**127**	**129**		
Fracture	**Fracture1**			**Variable**	−250
			f2	4×10^{-3}	−246
			f3	4×10^{-3}	−261
			f4	6×10^{-3}	−271
	f5			3×10^{-3}	−235
	f6			3×10^{-3}	−238
		f7		3×10^{-3}	−235
			f8	3×10^{-3}	−235

The approach used for Task 7B, based on a stochastic facies distribution, was also considered and tested. However, fracture density was too low in the rock volume considered in Task 7C to represent the rock mass with several facies. For example, if a drillhole interval equal to 1 m was chosen, almost all the intervals within the ONK-PP drillholes would have a fracture density equal to zero. However, the 1-m resolution is too coarse for the horizontal discretization along the plane of Fracture1 and too fine for the discretization orthogonally to it. A fine discretization orthogonal to Fracture1 will dramatically increase model size (Table 4-4), memory requirements, and thus model run time. Therefore, the disparity between the required fine mesh resolution for Fracture1 and for the rest of the domain, as well as the low fracture density in the region of interest, indicated that the stochastic facies conceptual model was not appropriate for the single-fracture modeling scale of Task 7C.

The KR boreholes located close to the shafts (KR38, KR24, KR48, KR24, KR23, KR25, KR28, and KR37) and pilot holes PH6 and PH7 were also considered to increase the number of available fracture data. Pilot holes are drillholes that were core drilled along the tunnel profile to confirm the quality of the rock mass for tunnel construction. Each of the KR boreholes mentioned above contained no more than two fractures in the region of interest of Task7C. Pilot hole PH6 was located above the region of interest, at depth of −135 m a.s.l. Pilot hole PH7 was closer to Fracture1, but only six fracture trasmissivities were measured along the hole. Thus, the quantity and quality of available data were still not enough to define a reasonable representation of fractured rock facies for the rock volume modeled in Task 7C.

4.3.1 7C2 – Drillholes ONK-PP122, 124, 126, 128 (shaft KU2)

Fracture1 was identified by observing a simultaneous hydraulic response in all drillholes located in shaft KU2, as shown by the black triangles at the depth of 67 meters in Figure 4-8. Flow rates of about 3000 ml/h were measured in ONK-PP124 and ONK-PP126, while flow rates inferior to 1000 ml/h were measured in the other drillholes (Table 4-9). However, as mentioned in the previous section, several minor fractures were identified along the ONK-PP drillholes in addition to Fracture1, as shown in Figure 4-8.

The outflow, the sum of PFL flow rates, the corresponding deviation, and the flow rate at Fracture1 for drillholes in shaft KU2 are listed in Table 4-9. A complete summary of data for shaft KU2 is found in Appendix D.

Different simulations were performed to find the most appropriate outflow to assign to open drillholes. The best option was to consider the sum of PFL flow rates increased by an amount equal to the observed relative deviation (Table 4-9). Figure 4-9 shows the difference between two different cases. Red circles show flow rates at Fracture1 when the total outflow from drillholes was considered, while blue squares are the results obtained using the sum of PFL flow rates increased by the deviation as outflow. The latter option provides better results, in particular for drillholes ONK-PP123 and ONK-PP126.

Table 4-9. Measurements at drillholes located in shaft KU2 (Pekkanen 2009a).

Drillhole	Outflow [ml/h]	Sum of PFL flows [ml/h]	Relative deviation [%]	Flow at fracture1 [ml/h]
ONK-PP128	3900	4440	+12%	761
ONK-PP122	6600	5640	−17%	996
ONK-PP123	9000	7620	−18%	961
ONK-PP124	8700	7140	−22%	2870
ONK-PP126	7800	6180	−26%	2930

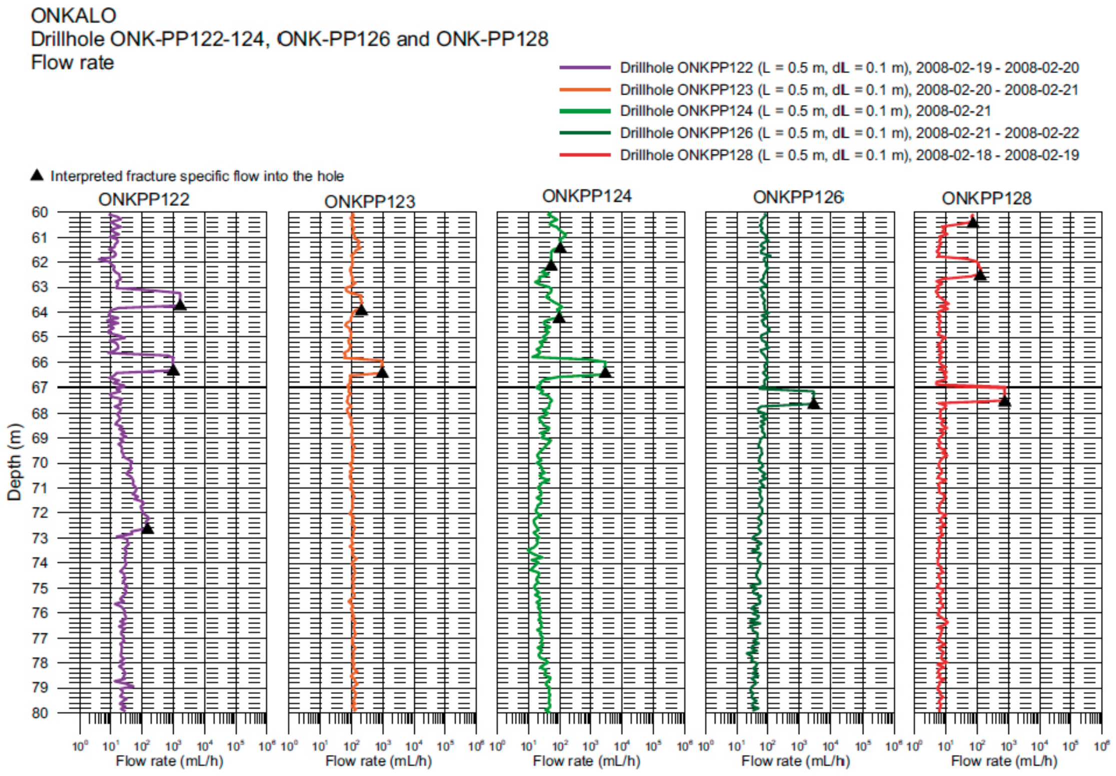

Figure 4-8. PFL measurements in shaft KU2: Fracture1 is identified at the depth of about 67 m.

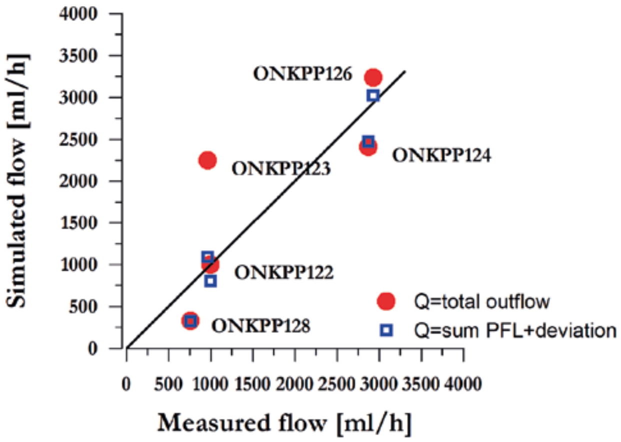

Figure 4-9. *Simulated and measured flow rates at fracture1in shaft KU2.*

The impact of correlation length and outflow *Q* for drillhole ONK-PP122 is shown in Figure 4-10. A correlation length equal to 0.35 m provides the best match between simulated and measured flow rates. Moreover, as already mentioned, the total outflow (Q=6600 ml/h, see Appendix D) for the 100-meter deep drillhole is larger than the measured flow rates in the 40-meter deep simulation domain. Simulation results for shaft KU2 are shown in Table 4-10.

4.3.2 7C2 – Drillholes ONK-PP131, ONK-PP134, ONK-PP137 (shaft KU1)

The number of fractures identified in the drillholes located in shaft KU1 was smaller compared to shaft KU2. Measured flow rates were also generally smaller than those measured in shaft KU2, as it can be seen by comparing values shown in Table 4-9 and Table 4-11. The difference between the total outflow from drillholes and the sum of measured PFL flow rates was relatively large, in particular for ONK-PP131 and ONK-PP137 (Table 4-11). Therefore, there is great uncertainty associated with these measurements and, as a result, matching the measured flow rates in shaft KU1 is more challenging than in shaft KU2.

Table 4-10. Summary of simulation results for shaft KU2.

Name	Drillhole	Flow rates at Fracture1		Flow rates at other identified fractures	
		Measured [ml/h]	Simulated [ml/h]	Measured [ml/h]	Simulated [ml/h]
s-PP122 Q=32.33 m^3/y=3690 ml/h	ONK-PP122	996	803	53 149 1660 243	71 171 1918 253
s-PP123 Q=12.1 m^3/y=1381 ml/h	ONK-PP123	961	1092	68	68
s-PP124 Q=33.3 m^3/y=3801 ml/h	ONK-PP124	2870	2473	96 53 104	355 153 191
s-PP126 Q=32.4 m^3/y=3700 ml/h	ONK-PP126	2930	3022		
s-PP128 Q=8.9 m^3/y=1016 ml/h	ONK-PP128	761	325	73 123 54	109 123 54

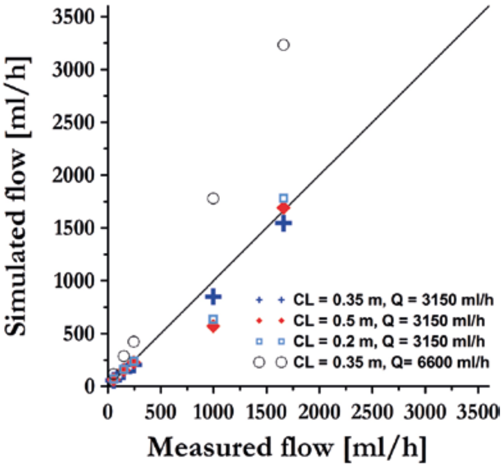

Figure 4-10. *Flow rates at drillhole ONK-PP122: PFL measurement equal to 996 ml/h is located at the intersection with Fracture1.*

Table 4-11. Measurements at drillholes located in shaft KU1 (Pekkanen 2009a).

Drillhole	Total outflow	Sum of PFL measurements [ml/h]	Relative deviation [%]
ONK-PP131	1800	480	−275
ONK-PP134	1800	1086	−66
ONK-PP137	3600	270	−1233

The interpretation of PFL and SPR measurements in KU1 allowed for the identification of Fracture1 only in ONK-PP134 (Figure 4-11). It was identified at a depth of about 74 meters and characterized by a flow rate of 367 ml/h. This value is much smaller than the flow rates measured in shaft KU2, which were between 700 and 3000 ml/h (Table 4-9), indicating a smaller fracture aperture in shaft KU1. A complete summary of data for shaft KU1 is found in Appendix D.

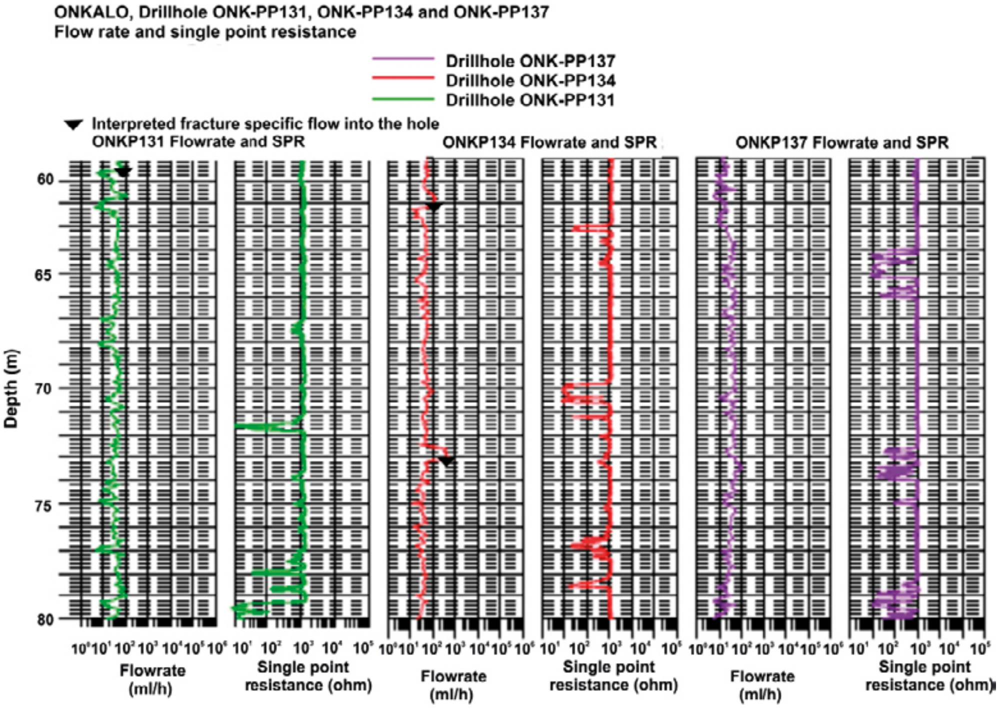

Figure 4-11. *PFL and SPR measurements in shaft KU1 between depth 60 and 80 m along the drillholes: Fracture1 is identified at the depth of about 73 m in ONK-PP134 (Pekkanen 2009b).*

Simulations s-PP131, s-PP134, and s-PP137 were executed and results are summarized in Table 4-12. Results from drillhole ONK-PP134 are also shown in Figure 4-12. Using the same aperture correlation length used for shaft KU2 (λ=0.35 m) and an outflow Q = 7.2 m^3/y, the simulated flow rate at Fracture1 was 210 ml/h. The outflow of 7.2 m^3/y is the sum of PFL measurements increased by the relative deviation observed in ONK-PP134, as done in shaft KU2. The outflow Q = 4 m^3/y is just the sum of PFL measurements. Figure 4-12 and Table 4-12 show that the match of flow rates is not very good, mainly because of the uncertainty associated with measurements in shaft KU1, as highlighted by the large relative deviation (Table 4-11).

For simulation s-PP134, the facies distribution generated in subtask 7B was used, but with different hydraulic conductivity values to reflect the lower fracture density in the region of interest of Task 7C. Although the facies distribution for Task7B was obtained using KR boreholes located generally outside of the region of interest of Task7C, this simulation was attempted mainly to verify if a heterogeneous porous rock could improve the match of flow rate at the intersection between Fracture1 and drillhole ONK-PP134. To obtain a satisfactory match between simulated and measured flow rate, the facies hydraulic conductivity were manually adjusted to the following values: 1×10^{-12} m/s, 3.2×10^{-11} m/s, 1.6×10^{-10} m/s, and 3.2×10^{-10} m/s. The flow rate simulated was slightly larger than the value obtained with a uniform K value equal to 1×10^{-11} m/s, such that no significant improvement in matching the measured flow rate was observed. Therefore, a homogenous porous rock hydraulic conductivity was considered as appropriate for simulation purposes at this scale of interest.

Table 4-12. Summary of simulation results for shaft KU1.

Name	Drillhole	Flow rates at Fracture1		Flow rates at other identified fractures	
		Measured [ml/h]	Simulated [ml/h]	Measured [ml/h]	Simulated [ml/h]
s-PP131* Q =2.3 m^3/y= ml/h	ONK-PP131		108	69	38
s-PP134 Q =7.2 m^3/y = ml/h	ONK-PP134	367	210	126	206
s-PP137* Q =2 m^3/y= ml/h	ONK-PP137		166	17	8

* For simulations s-PP131 and s-PP137, no flow rates were measured at fracture location.

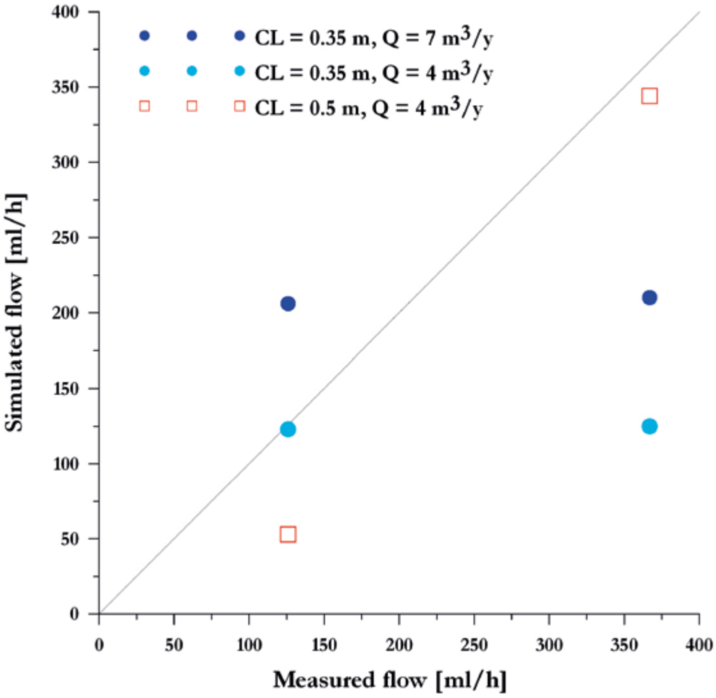

Figure 4-12. *Flow rates in drillhole ONK-PP134: the PFL measurement equal to 367 ml/h is located at the intersection with Fracture1.*

4.3.3 7C2 – Drillholes ONK-PP125, ONK-PP127, ONK-PP129 (shaft KU3)

Figure 4-13 illustrates flow rates that were measured at different locations along drillholes ONK-PP125, 127, and 129. Transmissive fractures are shown as lines crossing the holes and their approximate depth is shown on the left-hand side of the figure. ONK-PP125 was intersected by three fractures, ONK-PP127 by two fractures, and ONK-PP129 by five fractures. The hydraulic feature located at a depth of 77–78 m was identified as Fracture1, since a direct hydraulic connection was observed. All these features were included in the numerical model as discrete fractures. Only Fracture1 crosses all ONK-PP drillholes, while the others are local hydraulic features that cross only a specific drillhole. Fractures intersecting all three drillholes at depth of 10 m seemed hydraulically unconnected (Pekkanen 2009b).

For the single-hole tests (s-PP125 and s-PP127), natural outflow was not measured. Thus, comparison between total outflow from drillholes and the sum of measured PFL flow rates was not possible, contrary to the same single-hole simulations in shafts KU1 and KU2. The ouflow specified at measured drillholes was thus the sum of the measured PFL flow rates.

Results of simulations s-PP125 and s-PP127 are compared in Figure 4-14. Closed boreholes are those with a packer at their top, while an outflow is specified at ONKPP-125 and 127, respectively. The differences between simulated and measured flow rates are probably due to the outflow specified to the open drillholes, which is too small compared to the real unknown value that was not measured, as mentioned previously. The outflow can be manually increased to improve the match of flow rates, but it is not worthwhile considering the uncertainty associated to the PFL measurements themselves.

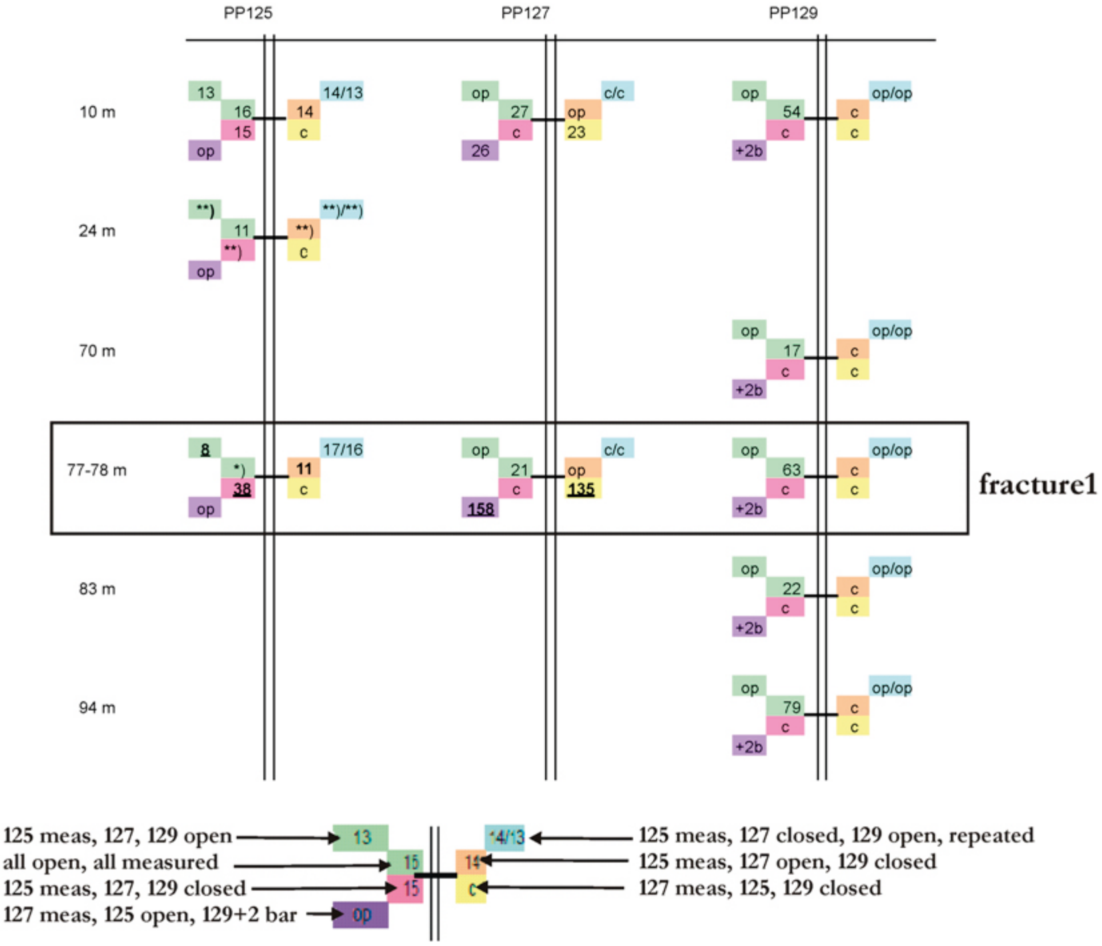

*) = high noise level, detection limit 10 ml/h
**) = probably some flow

Figure 4-13. Summary of PFL measurements in ml/h in shaft KU3 (Pekkanen 2009b).

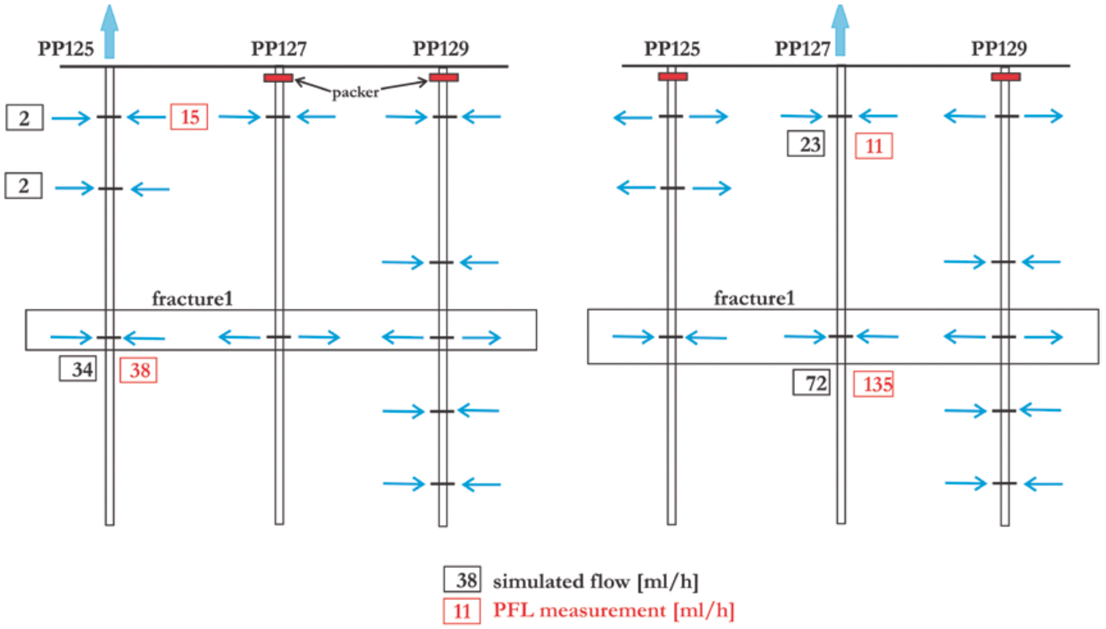

***Figure 4-14.** Flow directions for simulations s-PP125 (on the left) and s-PP127 (on the right).*

Besides flow rate magnitude, the other aspect analyzed in cross-hole tests was flow direction. In simulation s-PP125, the simulated directions agree with the expected directions. In contrast, in simulation s-PP127, an outflow from drillhole ONK-PP125 was expected, while an inflow was simulated (Figure 4-14). A deeper analysis was then conducted to better understand the reason of this unexpected flow direction. It was found that a different correlation length (0.5 m instead of 0.35 m) caused the inversion in the direction of flow (Figure 4-15). A close-up of the fracture aperture pattern for the two correlation lengths is shown in Figure 4-16. Since the aperture random field is not conditioned at drillhole locations, where the measurements were available, the aperture field can significantly vary if the correlation length is modified. These variations may have a noticeable influence on the simulated flow direction.

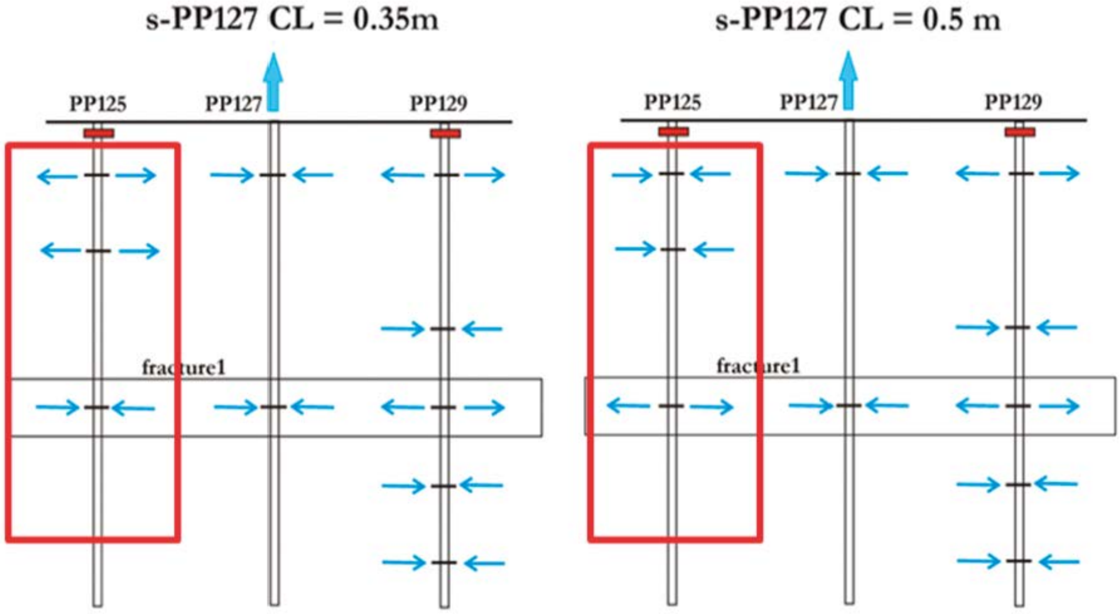

***Figure 4-15.** Variation of flow directions at drillhole-fracture intersections depending on fracture aperture correlation length.*

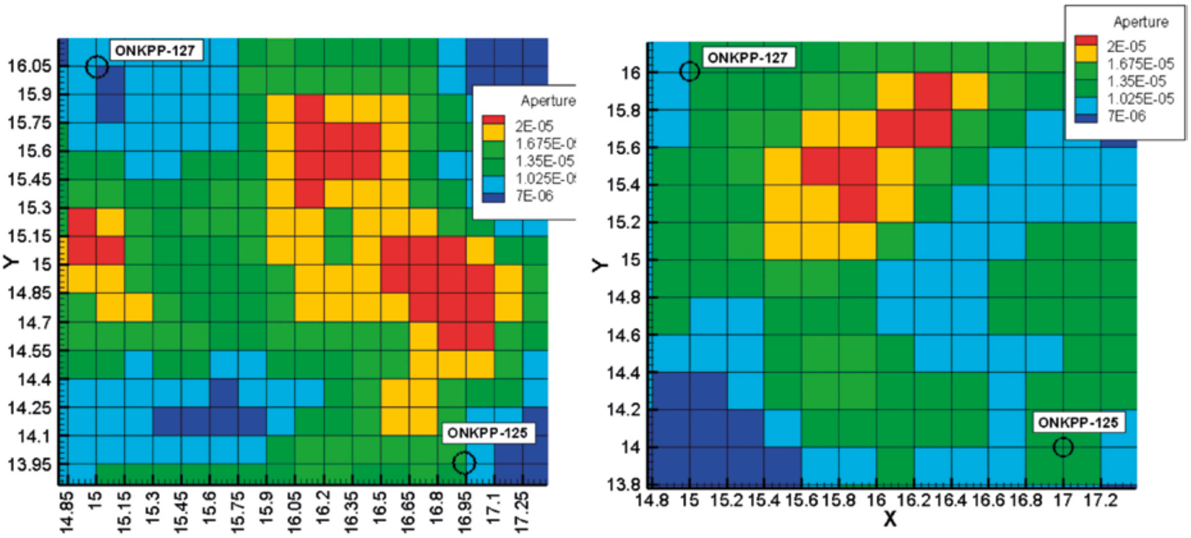

Correlation length 0.35 m

Correlation length 0.5 m

Figure 4-16. *Aperture pattern for different correlation lengths.*

Figure 4-17 shows simulation results for the scenarios with open drillholes. Although the total outflow from drillholes was measured, it was still difficult to match the measured flow rates, especially for the fractures located at a depth of 10 m. However, the flow rates simulated at Fracture1 at drillholes ONK-PP125 and ONK-PP127 provided better matches to observed flow rates.

Other cross-hole interference test results are shown in Figure 4-18. Again, the simulated flow rates for fractures located at a depth 10 m are smaller than those measured, while the flow rates at Fracture1 are generally better reproduced.

The results of the last simulation scenario are shown in Figure 4-19, where water was injected into ONK-PP129 to generate an overpressure. Outflow measurements were conducted in drillholes ONK-PP125 and ONK-PP127. Since the outflow measured in ONK-PP127 was not an exact value, it was varied in the simulation and the resulting flow rates at Fracture1 varied from 93 to 115 ml/h, which are not too far from the measured value of 158 ml/h.

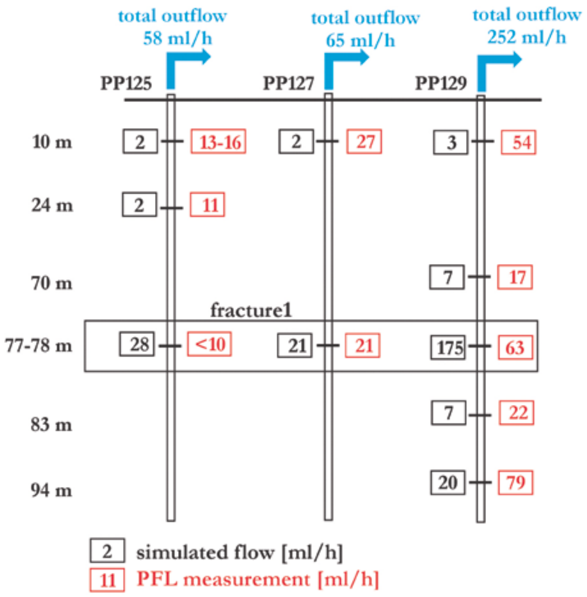

Figure 4-17. *Results for scenarios c-PP125-1, c-PP127-1, c-PP129-1.*

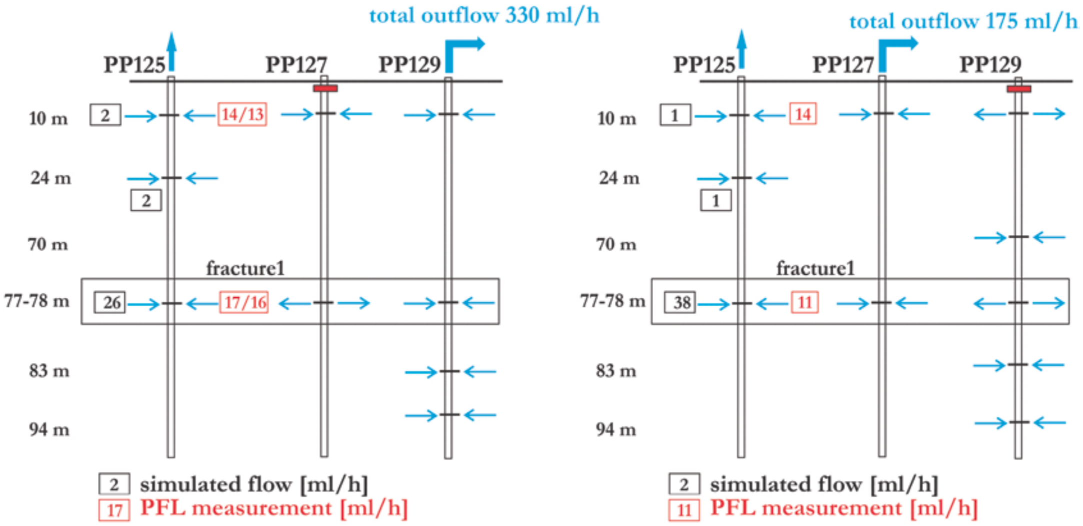

Figure 4-18. *Results for scenarios c-125-2 (on the left) and c-125-3 (on the right).*

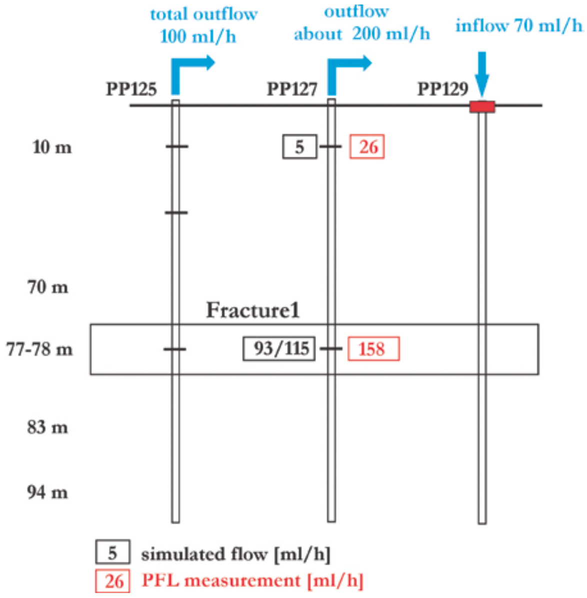

Figure 4-19. *Results for scenario c-127-2.*

4.3.4 7C2 – β-factor simulations

The first attempt to theoretically account for hydrodynamic effects on retention in single fractures was by Cvetkovic et al. (1999). The Lagrangian quantity β [T/L] was derived and identified as the controlling parameter for tracer retention, which incorporates the effect of structure and hydrodynamics (Cheng et al. 2003). The β-factor, or F-factor (Vidstrand et al. 2015), represents the ratio of flow wetted surface to water flux and it gives a measure of the surface available to matrix interaction and the time constant for the matrix interaction to occur. Simulations listed in Table 4-13 aimed at evaluating the β-factor in Subtask 7C2.

Table 4-13. List of β-factor simulations.

Simulation	Flow direction	Shaft
OL-KR38 NS	North-South	KU2
OL-KR38 EW	East-West	KU2
OL-KR24 NS	North- South	KU1
OL-KR24 EW	East-West	KU1
OL-KR48 NS	North- South	KU3
OL-KR48 EW	East-West	KU3

The β-factor was estimated with the procedure described by Hodgkinson (2007) for numerical models that do not have a specific capability to calculate this factor, such as HydroGeoSphere. For a fracture, the retardation surface sorption coefficient R_a is a function of the β-factor. The travel time of a tracer only affected by surface sorption is given by:

$$t_{tracer} = t_{water} R_a = t_{water}\left(1 + \frac{K_a}{b}\right) \tag{4-4}$$

where K_a is the surface sorption coefficient [m] and b is the half aperture of the fracture [m]. If $K_a/b >> 1$, Equation (4-4) can be simplified to:

$$t_{tracer} = t_{water}\frac{K_a}{b} \tag{4-5}$$

Since it is possible to express $\beta = \frac{t_{water}}{b}$, the following relation for the β-factor is obtained:

$$\beta = \frac{1}{K_a} \tag{4-6}$$

Thus, calculating the breakthrough curve for a tracer characterized by a large value of K_a ($K_a/b >> 1$) and assuming no matrix diffusion, the β-factor can be obtained from the breakthrough curve by scaling it by a factor equal to $1/K_a$. The advective time of a specific tracer is taken as reference and then divided by the corresponding K_a.

Dispersivity was set to a very low value to reduce the spreading effect of dispersion. The surface sorption coefficient was determined as (Dershowitz et al. 2003b):

$$K_a = (K_d\rho + \varepsilon)d \tag{4-7}$$

where *d* is the thickness of the fracture coating (5×10^{-4} m), ε is the porosity (0.05) and ρ is the density of the fracture coating (~2600 kg/m^3). Since no information on these parameters was available, the values specified were those used by Dershowitz et al. (2003b) for groundwater and transport modeling at the Äspö Hard Rock Laboratory.

4.3.5 Simulation setup and results

The domain dimensions were 30 m × 50 m in the x (Easting) and y (Northing) directions, respectively (Figure 4-20). The domain was 40 m thick along the vertical z direction, with Fracture1 oriented horizontally and located in the middle of the domain along the vertical. Since matrix diffusion should be neglected for calculation of the β-factor, the porous rock was considered impermeable. Therefore, only 2D flow and transport along the fracture were simulated and the domain thickness is thus irrelevant.

The domain was discretized with a prismatic mesh of 1.3×10^6 elements and about 7×10^5 nodes generated with GridBuilder (McLaren 2008). About 3.3×10^4 triangles were used to discretize Fracture1. The aperture was generated with the same variance, mean aperture, and correlation length considered for the previous simulations (Figure 4-21).

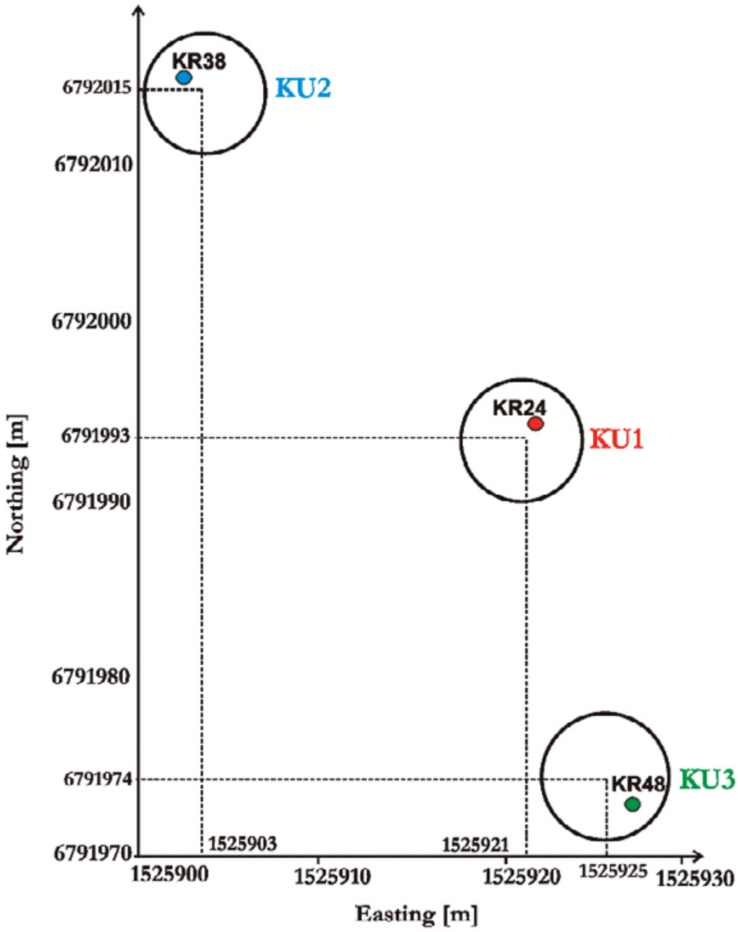

Figure 4-20. *Shaft locations and location of the simulation domain.*

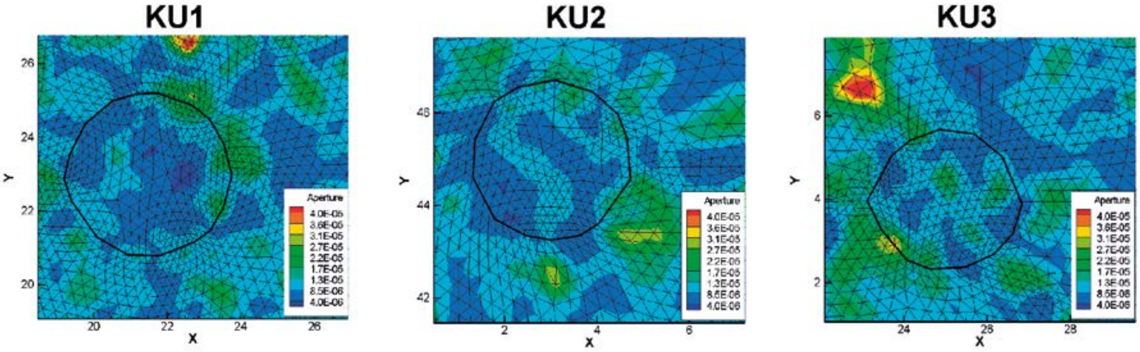

Figure 4-21. *Fracture1 aperture at the shaft locations.*

A hydraulic gradient of 0.1 was imposed along the North-South and East-West directions, respectively, as indicated by Vidstrand et al. (2015). Circular shafts were represented by internal boundaries, which were used to set the transport boundary conditions (Figure 4-20 and Figure 4-22).

A first-type transport boundary condition was specified at the shaft walls by selecting about 30 nodes along the half-circumference of each shaft. Observation points were placed on the opposite shaft wall (Figure 4-22). The initial concentration was zero everywhere in the domain.

To reduce the effect of dispersion along the fracture, very small longitudinal and transversal dispersivities were chosen (Table 4-14). Implicit transport time weighting and upstream weighting of velocities were used. Adaptive timesteps with a maximum change in concentration per timestep of 0.1 were chosen for the HydroGeoSphere simulations.

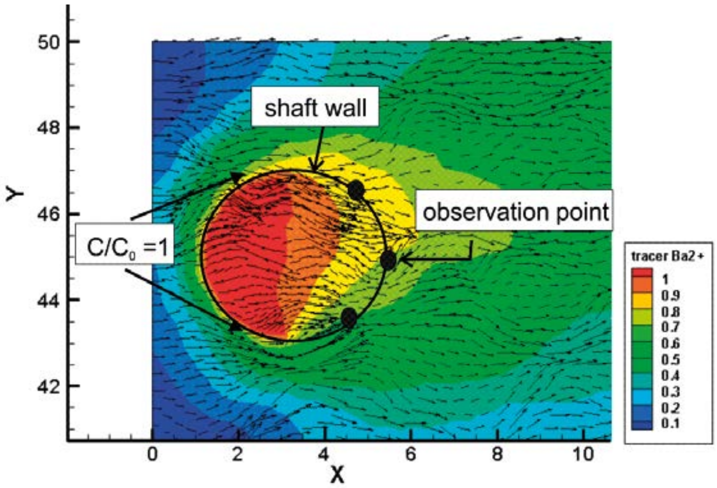

Figure 4-22. *Simulation setup, concentration contours, and velocity vectors in shaft KU2.*

Table 4-14. Fracture and solute simulation parameters.

Parameter	Value
Retardation factor Ba^{2+} [–]	1508
Retardation factor Ca^{2+} [–]	82
Longitudinal dispersivity [m]	1×10^{-4}
Transversal dispersivities [m]	1×10^{-5}

Barium and Calcium were considered as sorbed solutes (Table 4-14). The advective time was read from the solute breakthrough curves computed at the three observation points to calculate the β-factor. Finally, a comparison of the values obtained at the three different locations was conducted, to obtain the range of variation for the β-factor.

The computed Barium breakthrough curves for simulations OL-KR24 NS and OL-KR24 EW are shown in Figure 4-23. For simulation OL-KR24 EW, Calcium (Ca^{2+}) was also considered to verify the impact of the solute on the calculated β-factor. As expected, similar values were obtained using either Barium or Calcium (Table 4-15).

Some variation in the computed β-factor is observed, although the order of magnitude is the same for almost all simulations (Table 4-15). In shaft KU3, the values are smaller than in the other two shafts, in particular for simulation OL-KR48 NS, where an order of magnitude difference was obtained. This difference may be explained by the different aperture patterns, as shown in Figure 4-21. At shaft KU3, the fracture aperture is larger than in the other two shafts. As a consequence, the advective time is much smaller, as well as the β-factor. As already mentioned, the variable aperture random field was generated from the mean and variance of only nine transmissivities and from an assumed correlation length. Moreover, the aperture field was not conditioned at drillhole locations. Therefore, the calculated β-factor values should be only considered as qualitative indicators of the general impact of the variable aperture on retention properties.

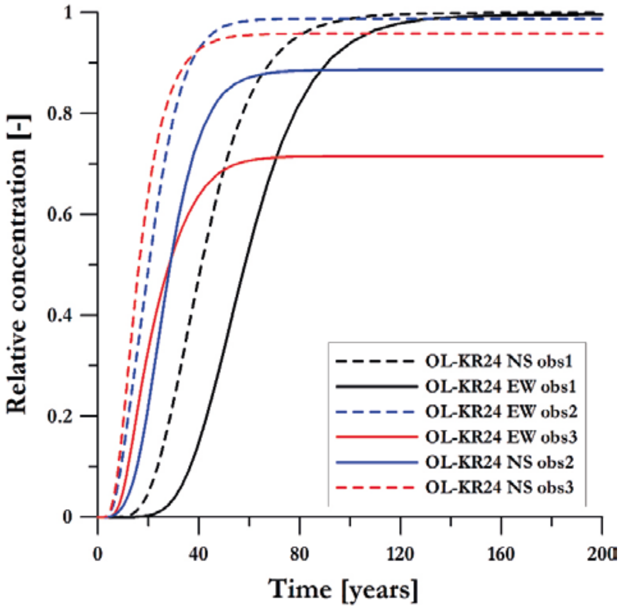

Figure 4-23. *Barium breaktrough curves in shaft KU1 along the two directions NS and EW.*

Table 4-15. Calculated values for the β-factor.

Simulation	β-factor (y/m)	Solute
OL-KR24 NS (KU1)	2750–6800	Barium
OL-KR24 EW(KU1)	3400–9900	Calcium
OL-KR24 EW (KU1)	3300–9700	Barium
OL-KR38 NS (KU2)	3300–4200	Barium
OL-KR38 EW (KU2)	3700–6150	Barium
OL-KR48 NS (KU3)	150–250	Barium
OL-KR48 EW (KU3)	1500–2500	Barium

4.4 Subtask 7C3: nappy experiment

The "nappy experiment" consisted in measuring the inflow into shaft KU2 by placing nappies (disposable diapers) where Fracture1 intersected the shaft wall. The experiment was conducted in the summer 2009, when the exhaust air shaft was used temporarily as an inlet air shaft. As a result of using the air shaft as an inlet air draft, the air draft was quite strong. The air draft, which has been identified as the biggest source of error, dried the fractures, such that detecting very small leakages was very difficult (Vidstrand et al. 2015). Only one fracture, between levels −250 and −230, fully crossed the shaft (Vidstrand et al. 2015).

For modeling purposes, only the leakage from Fracture1 was considered. A cylindrical simulation domain was created to better represent the shaft wall. A 2D triangular mesh was generated with GridBuilder (McLaren 2008). The two-dimensional mesh was superimposed in the third vertical dimension to generate 40 equally spaced sublayers of elements. The three-dimensional mesh had about 1.3 million elements and 690 000 nodes. The simulation domain and 2D triangular mesh are shown in Figure 4-24.

The shaft was assumed to be at atmospheric pressure. In contrast, hydraulic heads corresponding to a full pressure head at the considered depth were assigned to the lateral boundary. For the first simulation, the hydraulic conductivity of the porous rock matrix used for the previous simulations was considered (1.0×10^{-11} m/s), but it was then varied to improve the match between measured and simulated inflow. The same spatially-variable aperture for Subtask 7C2 was specified for Fracture1.

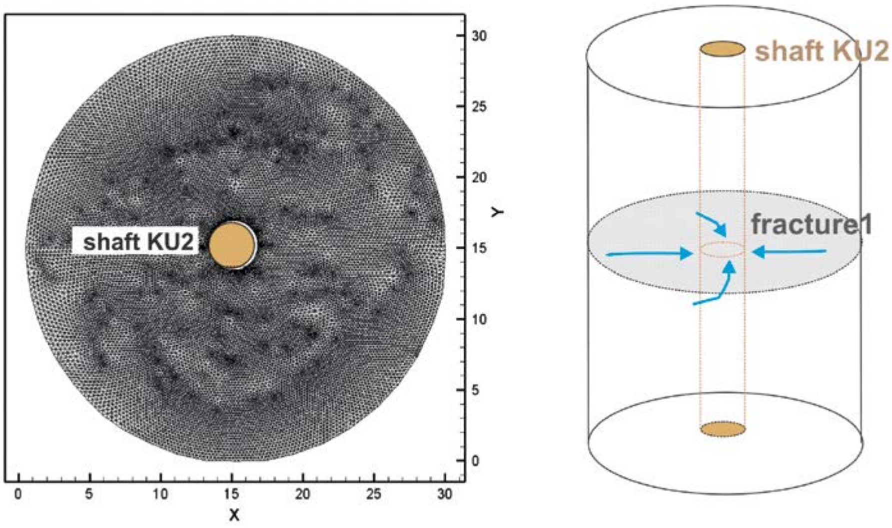

Figure 4-24. Triangular mesh and 3D domain for the simulation of the nappy experiment.

During the nappy experiment, the East and South-West side of the shaft wall was covered with grouting cement debris and dust, and was completely fracture leakage free (Isola 2009). Two scenarios were compared: in the first one, the inflow from the whole shaft circumference was considered, while in the second one, the inflow was only computed for the portion of shaft wall where leakage could be measured by nappies. Where inflow was not measured because of grouting and dust, a no-flow boundary condition was set. Moreover, to analyze the sensitivity of the computed inflow with respect to porous rock hydraulic conductivity and boundary conditions, several simulations were conducted. Their results are summarized in Table 4-16.

Figure 4-25 is a close-up of the shaft showing the velocity vector directions and magnitudes. Figure 4-26 shows the distribution of flow rates along the shaft wall, for the two scenarios described above. When a no-flow boundary condition is assigned to some portions of the shaft wall, the total inflow decreases to 1680 ml/h (Table 4-16), which is lower than the measured leakage.

Table 4-17 shows a comparison between the inflow measured at the shaft wall and the flow rates measured at drillhole locations. Flow rates at drillholes ONK-PP124 and ONK-PP126 were slightly larger than the total inflow into the shaft. A potential explanation for this difference remains to be identified, since the opposite flow rates might be expected given the smaller diameter of drillholes compared to the shaft. Grouting and dust on the shaft wall may have influenced the measurements. Moreover, the method to measure leakage was experimental and several sources of error were identified, such as the air current, surface moisture, too short absorbing time and lack of repeated measurements (Vidstrand et al. 2015). These reasons may have affected the measured leakage.

Table 4-16. Nappy experiment simulations (measured inflow 2712 ml/h).

	Porous rock matrix K [m/s]	Heads at lateral boundary [m]	Simulated inflow into the shaft [ml/h]
Scenario 1: inflow from the whole shaft wall circumference	1.0×10^{-11} *	350	2400
	1.205×10^{-10}	270	2700
	1.0×10^{-10}	270	2520
	1.0×10^{-9}	270	8460
Scenario 2: inflow only from the portion of the shaft wall circumference where leakage was measured	1.0×10^{-11} *	350	1680
	1.0×10^{-11} *	350	1500 (λ = 0.5 m)

*Same value used for simulations in subtask 7C2.

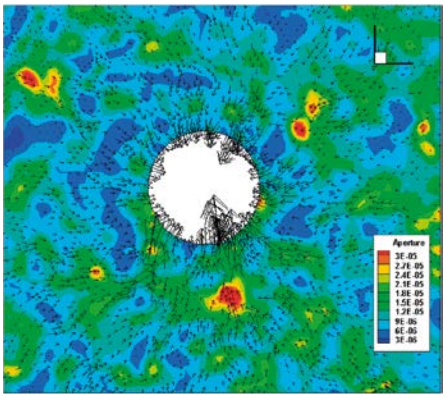

Figure 4-25. *Inflow to shaft indicated by velocity vectors.*

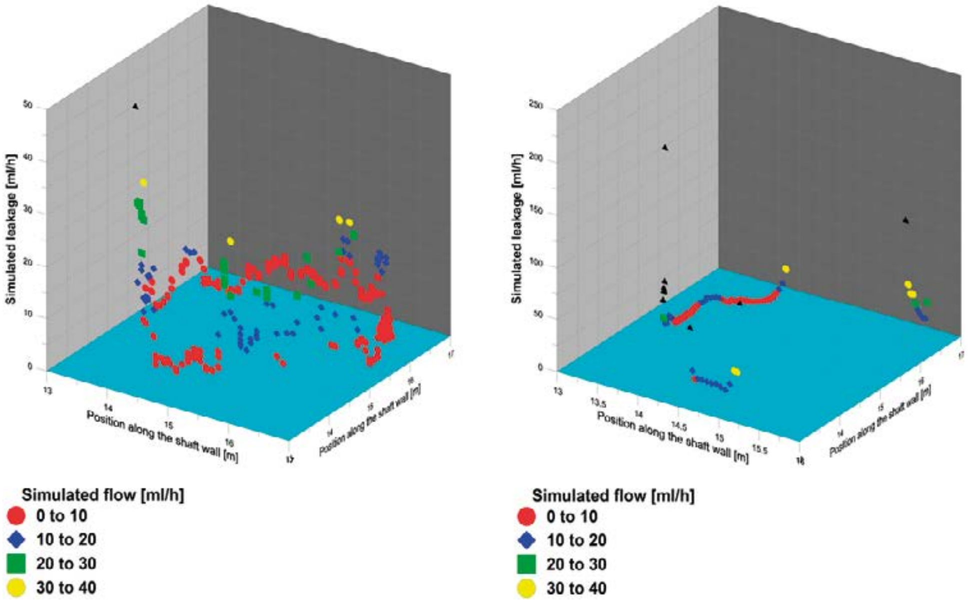

Figure 4-26. *Inflow into the shaft wall. On the left: leakage is simulated through the whole shaft circumference; on the right: leakage is simulated only from the portions of the shaft wall where leakage was measured with nappies.*

Table 4-17. Comparison between measured inflow into the shaft and flow rates measured at drillhole-fracture1 intersections.

Shaft KU2 nappy experiment		
Measured leakage from fracture1 into the shaft (diameter 3.5 m) [ml/h]	**Drillholes (average diameter 0.6 m)**	**PFL flow at fracture1 [ml/h]**
2712	ONK-PP122	996
	ONK-PP123	961
	ONK-PP124	2870
	ONK-PP126	2930
	ONK-PP128	761

4.5 Discussion and conclusion

4.5.1 Available data and micro-structural model for Fracture1

The available data to characterize Fracture1 was not sufficient to develop a detailed micro-structural model. Only nine transmissivity measurements were available and they were all located inside the diameter of the future shafts (about 4 m), while it was suggested to consider a simulation domain having an extension of 30 m, with Fracture1 reaching its lateral boundary. Therefore, given the spatial distribution of data, it was difficult to generate a realistic variable aperture for Fracture1 covering the whole simulation domain. Moreover, since FGEN did not allow conditioning the generated aperture field to the observations, it was not possible to reproduce the calculated aperture at drillhole locations. Finally, roughness was neglected since there were no measurements of the physical aperture required to account for roughness.

The main issue related to defining the micro-structural model for Fracture1 was the determination of the aperture correlation length. Too little data was available to build a variogram, such that the correlation length was arbitrarily defined on the basis of a literature review and model size constraints.

4.5.2 Simulation of single-hole and cross-hole hydraulic tests

The main issue associated with Subtask 7C2 simulations was to define proper flow boundary conditions, since drillholes were 100 m deep, while the suggested numerical model was only 40 m thick. Open drillholes were represented as pumping wells, while closed boreholes were wells with a zero flow rate. The pumping rate set to open drillholes was obtained from the sum of PFL measurements increased by the relative deviation observed between the total natural outflow from a drillhole and the sum of PFL measurements. The hydraulic conductivity of the porous rock matrix was set by manual calibration. A few tests were conducted to verify the possibility to consider conditioned stochastic facies realizations, as done in Task 7B. However, at the scale of interest of Task 7C and with few fracture data available, the facies conceptual model was shown to be inappropriate.

Pressure measurements were neglected, since they were lower than those expected because of probable connections between the closed drillholes and the main tunnel at the depth of −180 m.a.s.l. Although packers were installed, pressures measured in closed boreholes were smaller than those expected at that depth.

Matching of PFL measurements was satisfactory in shaft KU2, but not as successful in shaft KU1, where the large deviation between the sum of PFL measurements and total outflow from drillholes suggests a large uncertainty associated to measurements. In shaft KU3, the analysis was more focused on the analysis of flow directions in or out of boreholes. Matching of flow rates magnitude was satisfactory for Fracture1 but less for the other local fractures considered in the model, in particular for the fractures located at the depth of 10 m along the drillholes. This may be due to the different dimensions between the real drillholes (100 m) and the numerical model (40 m), to the uncertainty associated to the PFL measurements, or to the fact that no hydraulic connection was considered between these three fractures, as suggested by Pekkanen (2009b). The porous rock matrix hydraulic conductivity also influences the simulated flow rates. In fact, all nodes along the drillhole axes were characterized along by a small flow rate from (or into) the matrix. Since the sum of all these small flow rates was comparable to flow rates through some small fractures, the hydraulic properties of the porous rock also affected model calibration and matching of flow rates at discrete fractures.

Simulations of cross-hole hydraulic tests have shown that local apertures, which are a function of the aperture correlation length, have a significant influence on simulated flow directions. Thus, the aperture correlation length, which controls the local aperture distribution, is an important parameter for defining a micro-structural model and field data collection should be planned to ensure the definition of a proper aperture distribution. Further modeling work could investigate these aspects.

4.5.3 Calculation of β-factor

The β-factor was calculated here with the approach suggested by Hodgkinson (2007), since HydroGeoSphere does not have specific capability to determine this factor. The estimation of the β-factor was based on the analysis of solute breakthrough curves and advective time. The order of magnitude of the β-factor is the same in shafts KU1 and KU2, while it is smaller in shaft KU3, where the aperture of Fracture1 is larger. The variation of β-factor reflects the variation in the aperture of Fracture1. Since the aperture was not conditioned at shaft locations, where aperture was estimated, the calculated β-factor should be considered only qualitatively.

4.5.4 Simulation of the nappy experiment

The simulation of the nappy experiment opened up the discussion about measurement and simulation of inflow to drillholes. The simulated inflow along the whole circumference of the shaft matched the measured inflow quite well. The sensitivity of inflow with respect to porous rock hydraulic conductivity and to flow boundary conditions at the lateral boundary was also investigated (Table 4-16). However, when a portion of the shaft wall was defined as a no-flow boundary condition (where no leakage was measured because of dust and grouting), the simulated inflow became half of the measured inflow. Finally, a comparison of the inflow into the shaft diameter (3.5 m) and the PFL flow rates measured at drillhole locations showed differences that remain unexplained. The flow rates in drillholes ONK-PP124 and ONK-PP126 (diameter of 0.6 m) were even larger than the inflow into the whole shaft. This difference should be further investigated, since the evaluation of the inflow into boreholes is an important issue for evaluating the saturation of bentonite in deposition holes.

5 Conclusions

5.1 Summary of main findings

Task 7A

- Representing open boreholes in numerical models that simulate fluid flow and solute transport has been done with one-dimensional line elements.
- Discretization issues may arise when building grids and meshes that aim at representing irregular geometries of boreholes and fracture zones.
- Long open boreholes located in a low-permeability rock mass intersected by a few high-permeability fracture zones increase the bulk hydraulic conductivity of the system and decrease the bulk hydraulic gradient.
- Long open boreholes create connections between fracture zones that can be otherwise isolated and thus contribute to mixing of water, which may influence the geochemical signature.
- The site model used for Task 7A was too simplified to reproduce the PFL responses measured during the KR24 pumping test. The PFL measurements indicate a large variation in flow rates (both magnitude and direction) that cannot be reproduced satisfactorily with a simplified model.
- PFL responses are likely influenced by hydraulic properties of the fracture and rock mass in the vicinity of the borehole and fracture intersection. The site scale model could have likely been modified locally, for example by specifying a fracture skin, to better match the PFL measurements. The local transmissivities measured with the PFL provide a basis for defining the value of the fracture skin. Although those modifications would have improved the model with respect to observations, they would have likely not improved the model in areas where no observations are available. In other words, such a model conditioned locally may not have better predictive capabilities than a model not conditioned for locations where no observation is available. The conditioned model could, however, be used as a tool to reproduce observed flow in the fracture and rock mass.
- In contrast to measured PFL flow rates, the hydraulic head response during the KR24 test shows much less variation and could be reproduced with the simplified site model.

Task 7B

- Demonstration that a rock facies approach is an alternative to DFN models to represent flow at the block scale for the KR14–KR18 hydraulic tests.
- The advantage of the rock facies approach is that a regular grid can be used and discretization is not an issue, compared to a DFN model with a porous 3D matrix for which a new mesh must be generated for each realization of the DFN.
- In comparison to the rock facies approach, a DFN approach requires fracture generation away from zones where fractures have been observed and issues related to the definition of fracture size, distribution arise. The generation of DFN that are overly connected can be an issue.
- Defining rock facies also has challenges. Because fracture data is along vertical boreholes, there is little data to define the horizontal connectivity of facies. Also, the method assumes the hydraulic conductivity of a given facies is related to fracture density. That assumption may not always be valid because the transmissivity of single fractures has a log-normal distribution, with large aperture fractures dominating bulk hydraulic conductivity.
- Inverse modelling has demonstrated that using PFL data in addition to drawdown reduces the uncertainty associated with the hydraulic properties of rock facies.
- The transmissivities determined from field testing have been extremely useful, and probably essential, in defining the various rock facies.

Task 7C

- The level of detail of observations (PFL, nappy experiment) suggested that a microstructural model be developed for a single fracture (which wasn't done for 7A and 7B)
- There is large uncertainty associated with defining an aperture distribution because of the lack of small-scale data.
- From a numerical point of view, the grid size must be selected according to the correlation length assumed for the distribution, with the grid size smaller than the correlation length to correctly capture the spatial structure of the aperture field. It creates limitations in the correlation length that can be used.
- The model reproduced observations (PFL and flow measured during nappy experiment) reasonably well.

5.2 Main assumptions and simplifications

- Different conceptual models were used for the task, depending on scale.
- Assumptions common to all tasks
    - Neglect the effect of fluid composition (salinity) on its properties (density, viscosity).
    - Isothermal system.
    - Non-deformable fracture and matrix.
- Task 7A
    - Used DFN, with 2D discrete fractures representing the main hydraulic zones.
    - Each hydraulic zone was assigned a uniform aperture (transmissivity). It is not a limitation of the numerical model but rather a choice made to use a simplified model as opposed as a site-specific model.
    - The rock matrix was discretized in 3D as an equivalent porous medium.
- Task 7B
    - Rock facies approach to represent the bulk rock mass, lumping rock matrix and fractures.
    - A single fracture, with higher K than surrounding, was represented as a discrete feature.
    - Assumed that facies K is proportional to fracture density.
- Task 7C
    - Single fracture discretized with variable aperture. The rock matrix was discretized in 3D but its hydraulic conductivity was so low that it didn't have any influence on simulated results (therefore similar to a purely DFN approach).
    - The β-factor was estimated with the procedure described by Hodgkinson (2007) for numerical models that do not have a specific capability to calculate this factor, such as HydroGeoSphere. Satisfactory results were obtained with this procedure.

5.3 Lessons learned and implications for Task 7 objectives

- Three different conceptual models were used for Tasks 7A, 7B and 7C.
    - The decision to use different conceptual models was not based on the limitations of the HydroGeoSphere model, but rather on the scale of investigation, which is not a new issue in hydrogeology. As a related comment, upscaling of flow and transport parameters is still a topic of research in the hydrogeological community but upscaling has not been addressed during Task 7 to link 7A, 7B and 7C.
    - The rock facies model used for 7B could not be used at the scale of 7C, because available data only allows definition of rock facies at larger scales (i.e. not at the scale of a single fracture).

- Hydraulic testing at the ONKALO, with the PFL and HTU-tool, has provided a unique data set that has proven to be extremely valuable for defining the hydraulic conductivity of fracture zones, single fractures and the rock mass. That data can be used, for example, to calculate fracture skins (task 7A) and improve calibration of the site-scale model.
- Flow measurements with the PFL have also been very useful in reducing uncertainty associated with the definition of the hydraulic conductivity of the rock facies in Task 7B (as opposed as using only drawdown values). The PFL measurements have also been useful in understanding observations and constraining the model for Task 7C.
- There was no significant computational limitation in performing tasks 7A, 7B and 7C. However
  - Computational limitations still exist to represent aperture variations in a single fracture at the scale of either 7A or 7B. The number of unknowns would be too large for a site-scale 3D model with aperture variations at the scale observed for Task 7C.
  - The HydroGeoSphere model doesn't have particle tracking capabilities. A full advective-dispersive solute transport simulation must be used to investigate the release of solute from a potential repository.

References

SKB's (Svensk Kärnbränslehantering AB) publications can be found at www.skb.se/publications.

Barton N, de Quadros E F, 1997. Joint aperture and roughness in the prediction of flow and groutability of rock masses. International Journal of Rock Mechanics and Mining Sciences 34, 252.e1–252.e14.

Bonnet E, Bour O, Odling N E, Davy P, Main I, Cowie P, B Berkowitz, 2001. Scaling of fracture systems in geological media. Reviews of Geophysics 39, 347–383.

Brown S R, Scholz C H, 1985. Broad bandwidth study of the topography of natural rock surfaces. Journal of Geophysical Research 90, 12575–12582.

Brown S R, Kranz R L, Bonner B P, 1986. Correlation between the surfaces of natural rock joints. Geophysical Research Letters 13, 1430–1433.

Brush D J, 2003. Quarried block experiment: numerical simulations of flow and transport experiments in a natural fracture. Prepared by University of Waterloo for Ontario Power Generation. Report 06819-REP-01300-10075-R00, Ontario Power Generation, Nuclear Waste Management Division, Canada.

Carle S F, 1996. A transition probability-based approach to geostatistical characterization of hydrostratigraphic architecture. PhD thesis. University of California.

Carle S F, 1997a. Implementation schemes for avoiding artifact discontinuities in simulated annealing. Mathematical Geology 29, 231–244.

Carle S F, 1997b. Integration of geologic interpretation into geostatistical simulation. In Pawlowsky-Glahn V (ed). Proceedings of IAMG'97: the third annual conference of the International Association for Mathematical Geology. Barcelona, CIMNE, 711–716.

Carle S F, 1999. T-PROGS: Transition Probability Geostatistical Software. Version 2.1. Davis, CA: University of California, Hydrologic Sciences Graduate Group.

Carle S F, Fogg G E, 1997. Modelling spatial variability with one and multidimensional continuous-lag Markov chains. Mathematical Geology 29, 891–918.

Cheng H, Cvetkovic V, Selroos J-O, 2003. Hydrodynamic control of tracer retention in heterogeneous rock fractures. Water Resources Research 39, 1130. doi:10.1029/2002WR001354

Christensen S, Cooley R L, 1999. Evaluation of confidence intervals for a steady-state leaky aquifer model. Advances in Water Resources 22, 807–817.

Cornaton F J, Perrochet P, 2006. Groundwater age, life expectancy and transit time distributions in advective-dispersive systems: 1. Generalized reservoir theory. Advances in Water Resources 29, 1267–1291.

Cornaton F J, Park Y-J, Normani S D, Sudicky E A, Sykes J F, 2008. Use of groundwater lifetime expectancy for the performance assessment of a deep geologic waste repository: 1. Theory, illustrations, and implications. Water Resources Research 44, WO4406. doi:10.1029/2007WR006208

Cvetkovic V, Selroos J-O, Cheng H, 1999. Transport of reactive tracers in rock fractures. Journal of Fluid Mechanics 378, 335–356.

Dershowitz W S, Doe T W, Uchida M, Hermanson J, 2003a. Correlations between fracture size, transmissivity, and aperture. In Culligan P, Einstein H, Whittle A (eds). Soil and Rock America: proceedings of the 39th US Rock Mechanics Symposium. Boston, MA, 887–891.

Dershowitz W, Winberg A, Hermanson J, Bygård J, Tullborg E-L, Andersson P, Mazurek M, 2003b. Äspö Hard Rock Laboratory. Äspö Task Force on modelling of groundwater flow and transport of solutes. Task 6c. A semi-synthetic model of block scale conductive structures at the Äspö HRL. SKB IPR-03-13, Svensk Kärnbränslehantering AB.

Doherty J, 2004. PEST: Model-Independent Parameter Estimation, user manual. 5th ed. Brisbane: Watermark Numerical Computing.

Gelhar L W, 1987. Applications of stochastic models to solute transport in fractured rocks. SKB TR 87-05, Svensk Kärnbränslehantering AB.

Goovaerts P, 1996. Stochastic simulation of categorical variables using a classification algorithm and simulated annealing. Mathematical Geology 28, 909–921.

Graf T, Therrien R, 2005. Variable-density groundwater flow and solute transport in porous media containing nonuniform discrete fractures. Advances in Water Resources 28, 1351–1367.

Graf T, Therrien R, 2008. A method to discretize non-planar fractures for 3D subsurface flow and transport simulations. International Journal for Numerical Methods in Fluids 56, 2069–2090.

Hakami E, Larsson E, 1996. Aperture measurements and flow experiments on a single natural fracture. International Journal of Rock Mechanics and Mining Sciences & Geomechanics Abstracts 33, 395–404.

Hill M C, 2004. Methods and guidelines for effective model calibration. Proceedings of Joint Conference on Water Resource Engineering and Water Resources Planning and Management 2000, American Society of Civil Engineering publications.

Hill M C, Tiedeman C R, 2007. Effective groundwater model calibration: with analysis of data, sensitivities, predictions, and uncertainty. Hoboken, NJ: Wiley-Interscience.

Hodgkinson D, 2007. Äspö Task Force on modelling of groundwater flow and transport of solutes. Review of Tasks 6D, 6E, 6F and 6F2. SKB TR-07-03, Svensk Kärnbränslehantering AB.

Ingebritsen S E, Manning C E, 1999. Geological implications of a permeability-depth curve for the continental crust, Geology 27, 1107–1110.

Klockars J, Vaittinen T, Ahokas H, 2006. Hydraulic crosshole interference tests at Olkiluoto, Eurajoki in 2004, boreholes KR14–KR18 and KR15B–KR18B. Posiva Working Report 2006-01, Posiva Oy, Olkiluoto, Finland.

Kueper B H, McWhorter D B, 1991. The behaviour of dense, nonaqueous phase liquids in fractured clay and rock. Groundwater 29, 716–728.

Louis C, 1969. A study of groundwater flow in rock and its influence on the stability of rock masses. London: Imperial College of Science and Technology. (Rock mechanics research report 10.)

McLaren R, 2008. GridBuilder: a pre-processor for 2D, triangular element, finte-element programs. Waterloo: Groundwater Simulations Group.

Moore C, Doherty J, 2005. The cost of uniqueness in groundwater model calibration. Advances in Water Resources 29, 605–623.

Neuman S P, 2005. Trends, prospects and challenges in quantifying flow and transport through fractured rocks. Hydrogeology Journal 13, 124–147.

Nicholl M J, Rajaram H, Glass R J, Detwiler R, 1999. Saturated flow in a single fracture: evaluation of the Reynolds equation in measured aperture fields. Water Resource Research 35, 3361–3373.

Park Y-J, Sudicky E A, McLaren R G, Sykes J F, 2004. Analysis of hydraulic tracer response tests within moderately fractured rock based on a transition probability approach. Water Resources Research, 48, W12404. doi:10.1029/2004WR003188

Paulamäki S, 2007. Geological mapping of the region surrounding the Olkiluoto site. Posiva Working Report 2007-30, Posiva Oy, Finland.

Pekkanen J, 2009a. Difference flow measurements in ONKALO at Olkiluoto, drillholes ONK-PP122–ONK-PP124, ONK-PP126, ONK-PP128, ONK-PP131, ONK-PP134 and ONK-PP137. Posiva Working Report 2009-04, Posiva Oy, Finland.

Pekkanen J, 2009b. Difference flow measurements and hydraulic interference test in ONKALO at Olkiluoto, drillholes ONK-PP125, ONK-PP127 and ONK-PP129. Posiva Working Report 2009-40, Posiva Oy, Finland.

Poon C Y, Saylest R S, Jones T A, 1992. Surface measurement and fractal characterization of naturally fractured rocks. Journal of Physics D: Applied Physics 25, 1269–1275.

Robin M J L, Gutjahr A L, Sudicky E A, Wilson J L, 1993. Cross-correlated random field generation with the direct Fourier transform method. Water Resources Research 29, 2385–2397.

Rouhiainen P, Pöllänen J, 2003. Hydraulic crosshole interference test at the Olkiluoto site in Eurajoki, boreholes KR14–KR18 and KR15B–KR18B. Posiva Working Report 2003-30, Posiva Oy, Finland.

Tammisto E, Palmén J, Ahokas H, 2009. Database for hydraulically conductive fractures. Posiva Working Report 2009-30, Posiva Oy, Finland.

Therrien R, Sudicky E A, 1996. Three-dimensional analysis of variably-saturated flow and solute transport in discretely-fractured porous media. Journal of Contaminant Hydrology 23, 1–44.

Therrien R, Sudicky E A, McLaren R G, 2003. User's Guide for FRAC3DVS: an efficient simulator for three-dimensional, saturated-unsaturated groundwater flow and density-dependent, chain-decay solute transport in porous, discretely-fractured porous or dual-porosity formations, Université Laval and University of Waterloo.

Therrien R, Sudicky E A, McLaren R G, Panday S M, Guvanasen V, 2007. FRAC3DVS_OPG: A three-dimensional numerical model describing subsurface flow and solute transport, user's guide. Waterloo, Canada: Groundwater Simulations Group.

Therrien R, Sudicky E A, McLaren R G, Panday S M, 2009. HydroGeoSphere: a three-dimensional numerical model describing fully-integrated subsurface and surface flow and solute transport, user's guide. Waterloo, Canada: Groundwater Simulations Group.

Tsang Y W, Tsang C F, Neretnieks I, Moreno L, 1988. Flow and tracer transport in fractured media: a variable aperture channel model and its properties. Water Resources Research 24, 2049–2060.

USGS, 1998. Improving ground-water flow model calibration with the advective-transport observation (ADV) package to MODFLOW-2000. USGS Fact Sheet FS-059-98, U.S. Geological Survey.

Vaittinen T, Ahokas H, 2005. Long-term pumping test in borehole KR24 and pressure observations at Olkiluoto, Eurajoki in 2004. Posiva Working Report 2005-40, Posiva Oy, Finland.

Vecchia A V, Cooley R L, 1987. Simultaneous confidence and prediction intervals for nonlinear regression models with application to a groundwater flow model. Water Resources Research 23, 1237–1250.

Vidstrand P (ed), Ahokas H, Bockgård N, Dershowitz B, Holton D, Lanyon B, Poteri A, Koskinen L, 2015. SKB Task Force GWFTS – Task 7 Descriptions for hydrogeological modelling of Olkiluoto, Finland. Compilation of all task descriptions assessed within the Task 7 of the SKB Task Force on modelling of groundwater flow and transport of solutes. SKB P-12-21, Svensk Kärnbränslehantering AB, Sweden

Väisäsvaara J, 2009. Transverse flow measurements at the Olkiluoto site in Eurajoki, drillholes OL-KR15, -KR15B, -KR16B, -KR17B, and -KR18. Posiva Working Report 2009-23, Posiva Oy, Finland.

Väisäsvaara J, Kristiansson S, Pöllänen J, Sokolnicki M, 2008. Monitoring measurements by the difference flow method during the year 2007, drillholes OL-KR2, -KR7, -KR8, -KR14, -KR22, -KR22B, -KR27 and -KR28. Posiva Working Report 2008-40, Posiva Oy, Finland.

Weissmann G S, Carle S F, Fogg G E, 1999. Three-dimensional hydrofacies modeling based on soil surveys and transition probability geostatistics. Water Resources Research 35, 1761–1770.

Appendix A

Task 7B – Borehole Data

Table A-1. List of boreholes and relative attributes used in this study.

Borehole	Diameter (mm)	X (m) (east)	Y (m) (north)	Z (m.a.s.l.)	Azimuth (degrees)	Inclination (degrees)	Length (m)
KR1	56	1 525 540.54	6792 362.42	9.91	340.7	75.0	1001.05
KR2	56	1 525 883.01	6 792 582.79	8.62	359.3	76.2	1051.89
KR7	56	1 525 558.90	6 792 118.14	8.67	43.1	69.5	811.05
KR10	76	1 525 887.21	6 792 283.65	9.32	0.0	89.76	614.40
KR12	56	1 525 949.76	6 792 571.68	8.80	90.0	69.7	795.34
KR13	76	1 525 980.42	6 792 687.52	5.80	285.0	55.6	500.21
KR14	76	1 525 865.31	6 792 376.73	8.27	0.0	69.9	514.10
KR15	76	1 525 840.14	6 792 439.91	8.42	321.0	89.4	518.85
KR15B	76	1 525 838.44	6 792 442.21	8.35	0.0	90.0	45.14
KR16	76	1 525 797.15	6 792 423.01	8.73	0.0	90.0	170.20
KR16B	76	1 525 794.36	6 792 422.44	8.85	0.0	90.0	45.20
KR17	76	1 525 810.01	6 792 453.11	8.43	0.0	90.0	157.13
KR17B	76	1 525 809.21	6 792 456.03	8.44	0.0	90.0	45.30
KR18	76	1 525 826.70	6 792 432.83	8.63	0.0	90.0	125.49
KR18B	76	1 525 824.33	6 792 422.07	9.03	0.0	90.0	45.53
KR20	76	1 525 655.39	6 792 623.56	7.43	290.0	50.4	494.72
KR20B	76	1 525 654.04	6 792 619.86	7.25	290.0	49.5	45.10
KR30	75.7	1 525 870.00	6 792 224.91	8.71	359.5	75.0	98.28
KR32	75.7	1 525 836.04	6 792 605.91	6.82	352.0	54.8	191.81

Table A-2. Horizontal surface distance between boreholes KR14–KR18.

Borehole pair	Distance (m)
KR14–KR15	68.00
KR14–KR15B	70.77
KR14–KR16	82.38
KR14–KR16B	84.39
KR14–KR17	94.29
KR14–KR17B	97.13
KR14–KR18	68.10
KR14–KR18B	61.11
KR15–KR16	46.19
KR15–KR16B	49.00
KR15–KR17	32.89
KR15–KR17B	34.87
KR15–KR18	15.19
KR15–KR18B	23.83
KR15B–KR16	45.53
KR15B–KR16B	48.31
KR15B–KR17	30.44
KR15B–KR17B	32.33
KR15B–KR18	15.02
KR15B–KR18B	24.59
KR16–KR17	32.73
KR16–KR17B	35.15
KR16–KR18	31.13
KR16–KR18B	27.19
KR16B–KR17	34.43
KR16B–KR17B	36.72
KR16B–KR18	33.96
KR16B–KR18B	29.97
KR17–KR18	26.26
KR17–KR18B	34.18
KR17B–KR18	29.05
KR17B–KR18B	37.17
Average	**44.13**

Appendix B

Task 7B – Packed-off boreholes

Table B-1 List of packed-off boreholes used in simulations SS22, SS25, and SS26

Borehole	Section	Top (mah)	Bottom (mah)
KR14	KR14:L1	53.5	514.1
KR14	KR14:L2	47.5	52.5
KR14	KR14:L3	9.5	46.0
KR15*	KR15:L1	446.0	460.0
KR15*	KR15:L2	241.0	245.0
KR15	KR15:L3	116.0	145.0
KR15	KR15:L4	66.0	75.0
KR15	KR15:L5	51.0	65.0
KR15	KR15:L6	40.0	50.0
KR15B	KR15B:L1	29.7	45.0
KR15B	KR15B:L2	4.5	28.7
KR16	KR16:L1	143.0	170.2
KR16	KR16:L2	113.0	142.0
KR16	KR16:L3	83.0	112.0
KR16	KR16:L4	63.0	82.0
KR16	KR16:L5	53.0	62.0
KR16	KR16:L6	40.0	52.0
KR16B	KR16B:L1	36.0	45.0
KR16B	KR16B:L2	26.0	35.0
KR16B**	KR16B:L3	4.5	25.0
KR17	KR17:L1	122.0	157.1
KR17	KR17:L2	97.0	111.0
KR17	KR17:L3	82.0	96.0
KR17	KR17:L4	67.0	71.0
KR17	KR17:L5	52.0	66.0
KR17	KR17:L6	40.0	51.0
KR17B*	KR17B:L1	31.3	45.0
KR17B*	KR17B:L2	4.1	30.3
KR18	KR18:HTU3P1	48.0	53.0
KR18	KR18:HTU3P1p3	40.0	47.0
KR18	KR18:HTU3P1p8	54.0	125.5

*Not considered because outside of the simulation domain.
**Not considered because no head measurement available at that location.

Appendix C

Task 7C outflow and pressure in drillholes

(from Pekkanen 2009a, 2009b)

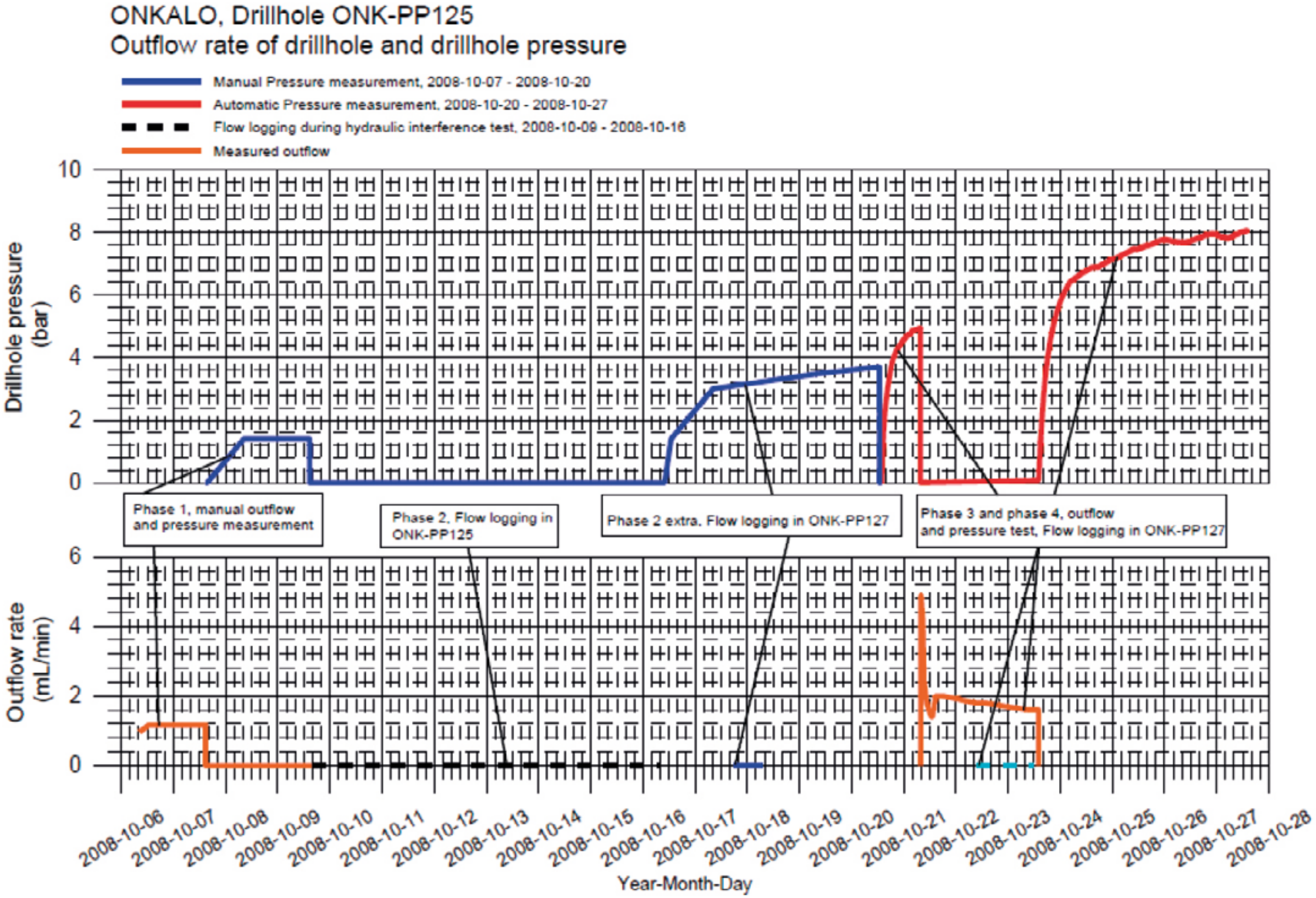

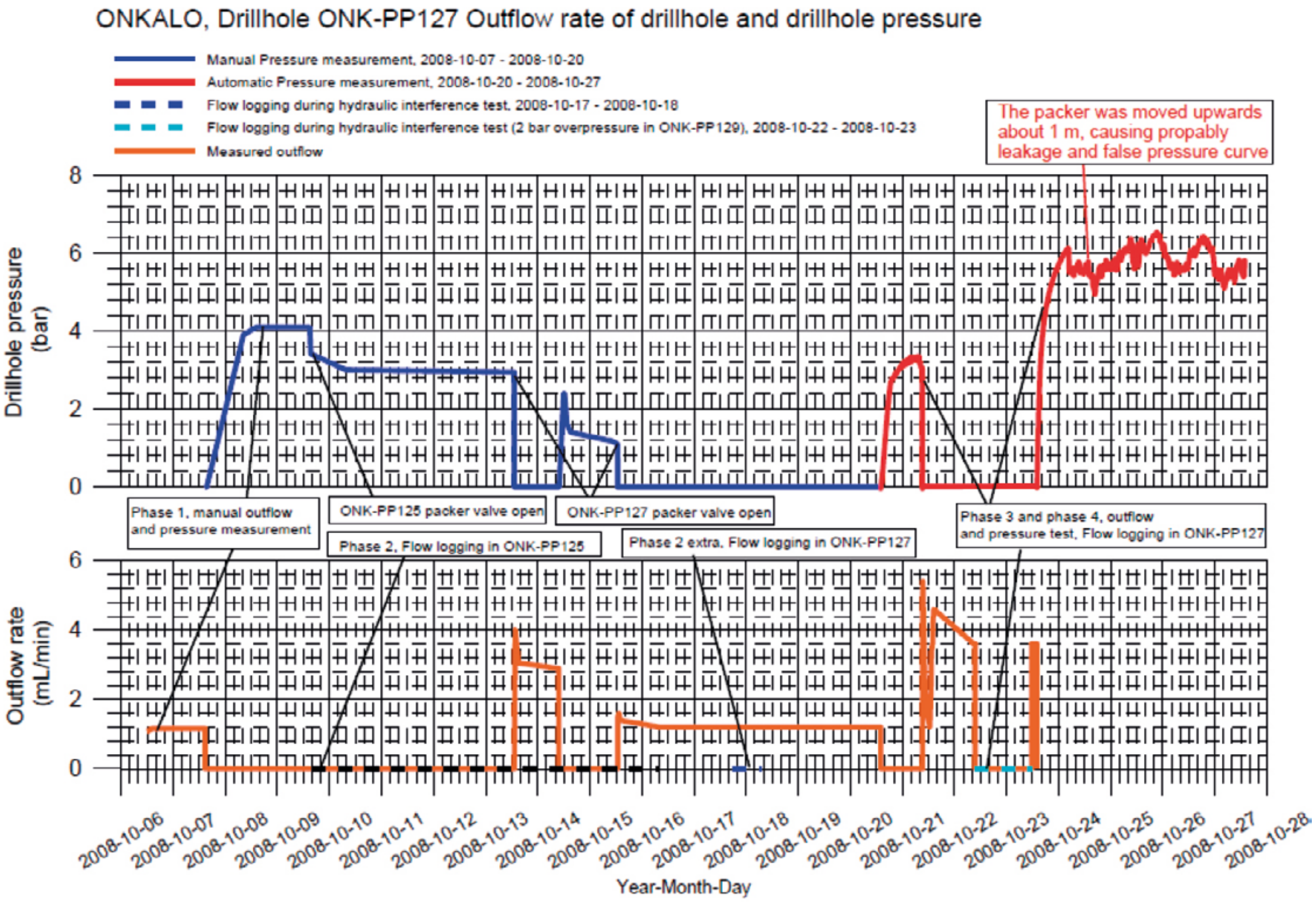

ONKALO, Drillhole ONK-PP127 Outflow rate of drillhole and drillhole pressure

The packer was moved upwards about 1 m, causing propably leakage and false pressure curve

Phase 1, manual outflow and pressure measurement

ONK-PP125 packer valve open

ONK-PP127 packer valve open

Phase 2, Flow logging in ONK-PP125

Phase 2 extra, Flow logging in ONK-PP127

Phase 3 and phase 4, outflow and pressure test, Flow logging in ONK-PP127

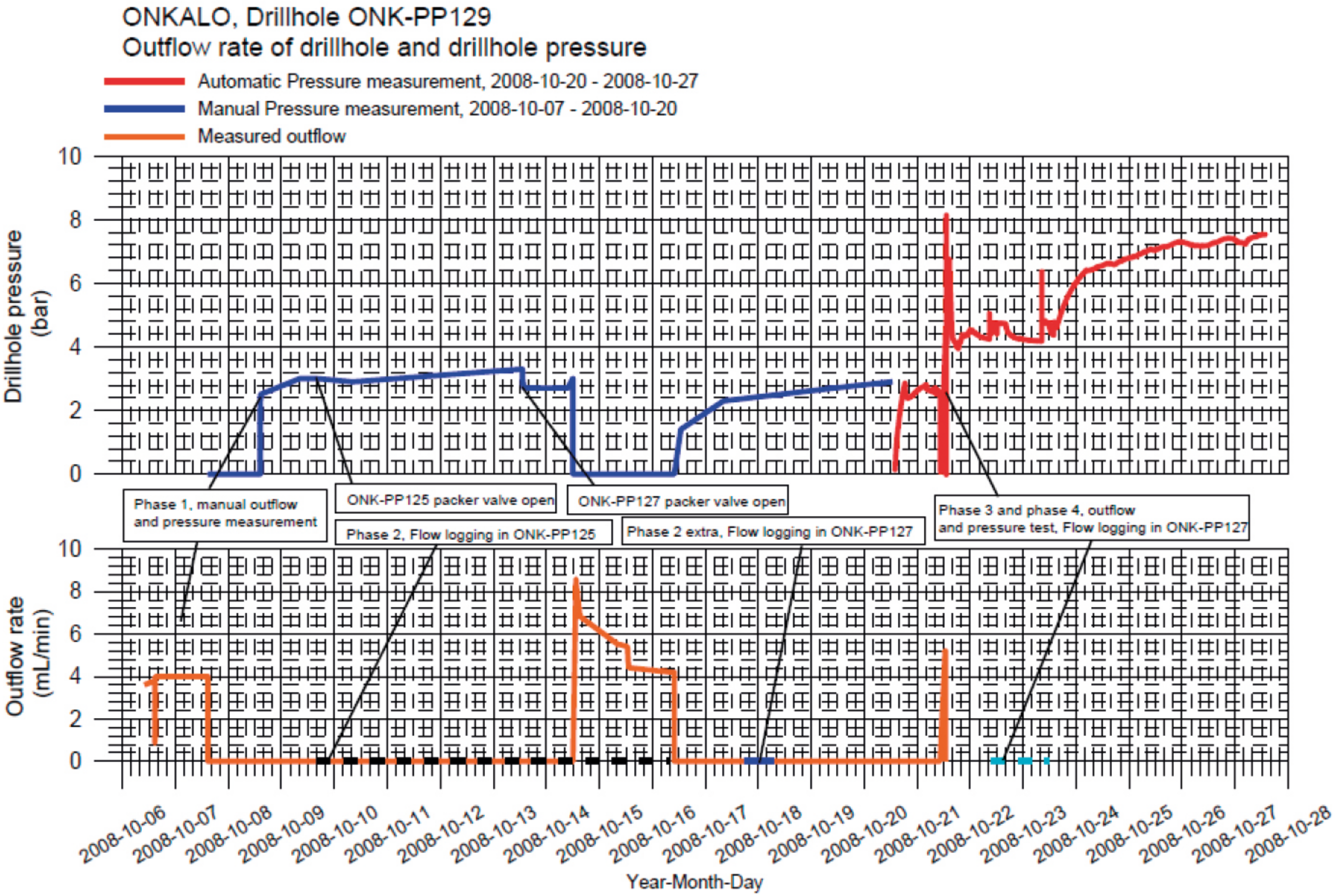
ONKALO, Drillhole ONK-PP129
Outflow rate of drillhole and drillhole pressure
Automatic Pressure measurement, 2008-10-20 - 2008-10-27
Manual Pressure measurement, 2008-10-07 - 2008-10-20
Measured outflow
Drillhole pressure (bar)
0
2
4
6
8
10
Phase 1, manual outflow and pressure measurement
ONK-PP125 packer valve open
Phase 2, Flow logging in ONK-PP125
ONK-PP127 packer valve open
Phase 2 extra, Flow logging in ONK-PP127
Phase 3 and phase 4, outflow and pressure test, Flow logging in ONK-PP127
Outflow rate (mL/min)
0
2
4
6
8
10
2008-10-06
2008-10-07
2008-10-08
2008-10-09
2008-10-10
2008-10-11
2008-10-12
2008-10-13
2008-10-14
2008-10-15
2008-10-16
2008-10-17
2008-10-18
2008-10-19
2008-10-20
2008-10-21
2008-10-22
2008-10-23
2008-10-24
2008-10-25
2008-10-26
2008-10-27
2008-10-28
Year-Month-Day

Appendix D

Task 7C fractures and PFL data

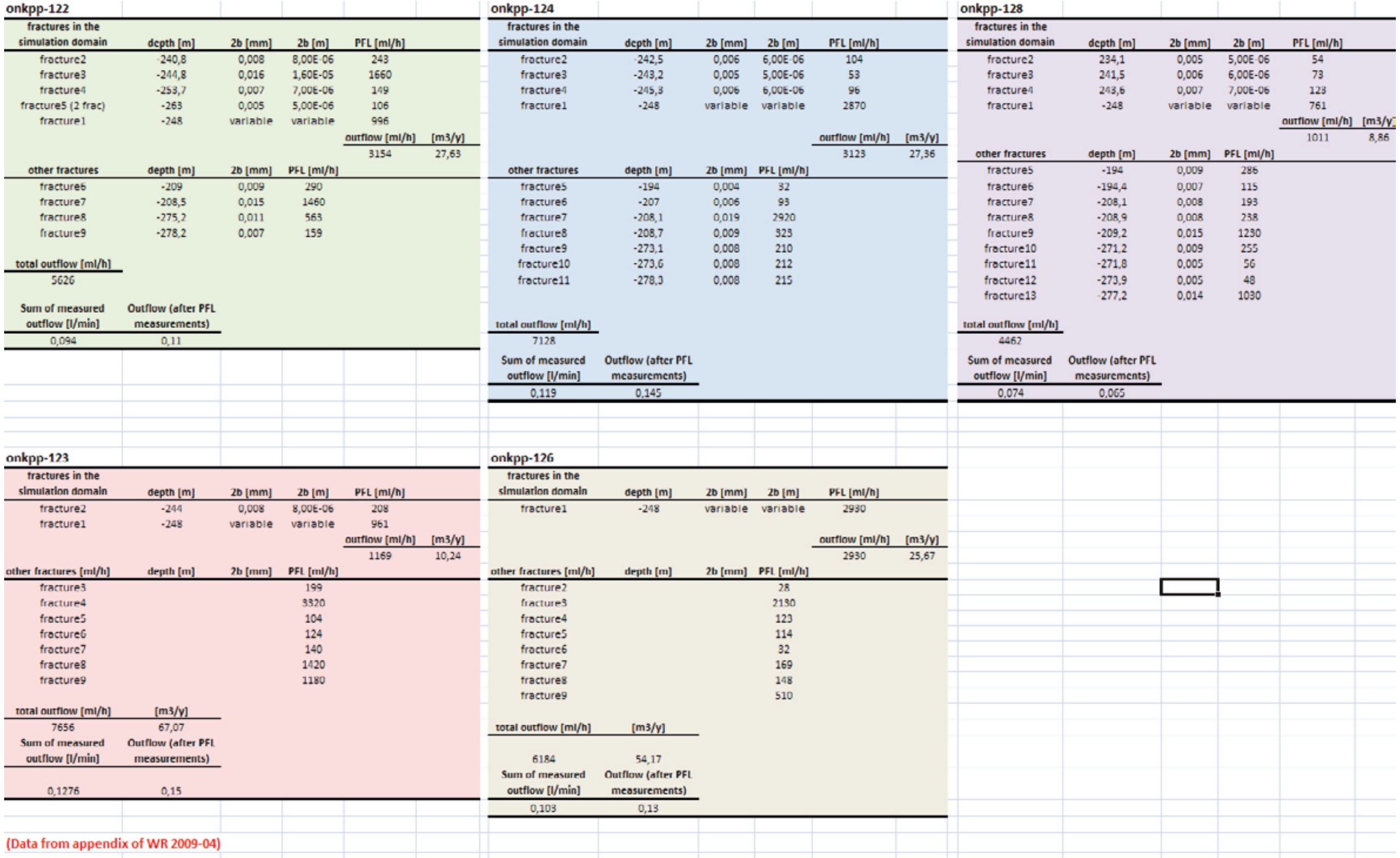

onkpp-122

fractures in the simulation domain	depth [m]	2b [mm]	2b [m]	PFL [ml/h]	
fracture2	-240,8	0,008	8,00E-06	243	
fracture3	-244,8	0,016	1,60E-05	1660	
fracture4	-253,7	0,007	7,00E-06	149	
fracture5 (2 frac)	-263	0,005	5,00E-06	106	
fracture1	-248	variable	variable	996	
				outflow [ml/h]	[m3/y]
				3154	27,63

other fractures	depth [m]	2b [mm]	PFL [ml/h]
fracture6	-209	0,009	290
fracture7	-208,5	0,015	1460
fracture8	-275,2	0,011	563
fracture9	-278,2	0,007	159

total outflow [ml/h]
5626

Sum of measured outflow [l/min]	Outflow (after PFL measurements)
0,094	0,11

onkpp-124

fractures in the simulation domain	depth [m]	2b [mm]	2b [m]	PFL [ml/h]	
fracture2	-242,5	0,006	6,00E-06	104	
fracture3	-243,2	0,005	5,00E-06	53	
fracture4	-245,3	0,006	6,00E-06	96	
fracture1	-248	variable	variable	2870	
				outflow [ml/h]	[m3/y]
				3123	27,36

other fractures	depth [m]	2b [mm]	PFL [ml/h]
fracture5	-194	0,004	32
fracture6	-207	0,006	93
fracture7	-208,1	0,019	2920
fracture8	-208,7	0,009	323
fracture9	-273,1	0,008	210
fracture10	-273,6	0,008	212
fracture11	-278,3	0,008	215

total outflow [ml/h]
7128

Sum of measured outflow [l/min]	Outflow (after PFL measurements)
0,119	0,145

onkpp-128

fractures in the simulation domain	depth [m]	2b [mm]	2b [m]	PFL [ml/h]	
fracture2	234,1	0,005	5,00E-06	54	
fracture3	241,5	0,006	6,00E-06	73	
fracture4	243,6	0,007	7,00E-06	123	
fracture1	-248	variable	variable	761	
				outflow [ml/h]	[m3/y
				1011	8,86

other fractures	depth [m]	2b [mm]	PFL [ml/h]
fracture5	-194	0,009	286
fracture6	-194,4	0,007	115
fracture7	-208,1	0,008	193
fracture8	-208,9	0,008	238
fracture9	-209,2	0,015	1230
fracture10	-271,2	0,009	255
fracture11	-271,8	0,005	56
fracture12	-273,9	0,005	48
fracture13	-277,2	0,014	1030

total outflow [ml/h]
4462

Sum of measured outflow [l/min]	Outflow (after PFL measurements)
0,074	0,065

onkpp-123

fractures in the simulation domain	depth [m]	2b [mm]	2b [m]	PFL [ml/h]	
fracture2	-244	0,008	8,00E-06	208	
fracture1	-248	variable	variable	961	
				outflow [ml/h]	[m3/y]
				1169	10,24

other fractures [ml/h]	depth [m]	2b [mm]	PFL [ml/h]
fracture3			199
fracture4			3320
fracture5			104
fracture6			124
fracture7			140
fracture8			1420
fracture9			1180

total outflow [ml/h]	[m3/y]
7656	67,07

Sum of measured outflow [l/min]	Outflow (after PFL measurements)
0,1276	0,15

onkpp-126

fractures in the simulation domain	depth [m]	2b [mm]	2b [m]	PFL [ml/h]	
fracture1	-248	variable	variable	2930	
				outflow [ml/h]	[m3/y]
				2930	25,67

other fractures [ml/h]	depth [m]	2b [mm]	PFL [ml/h]
fracture2			28
fracture3			2130
fracture4			123
fracture5			114
fracture6			32
fracture7			169
fracture8			148
fracture9			510

total outflow [ml/h]	[m3/y]
6184	54,17

Sum of measured outflow [l/min]	Outflow (after PFL measurements)
0,103	0,13

(Data from appendix of WR 2009-04)

onkpp-131

fractures in the simulation domain	depth [m]	2b [mm]	2b [m]	PFL [ml/h]
fracture2	-238,1	0,008	6,00E-03	69
fracture1 ??	-250	variable	variable	??

outflow [ml/h]	[m3/y]
69	0,60

other fractures	depth [m]	2b [mm]	PFL [ml/h]
fracture3	-186,1	0,004	32
fracture4	-188,1	0,005	53
fracture5	-207,7	0,008	189
fracture6	-276,9	0,007	137

total outflow [ml/h]
480

Sum of measured outflow [l/min]	Outflow (after PFL measurements)
0,008	0,03

onkpp-134

fractures in the simulation domain	depth [m]	2b [mm]	2b [m]	PFL [ml/h]
fracture2	-239,6	0,007	7,00E-06	126
fracture1	-250,6	variable	variable	367

outflow [ml/h]	[m3/y]
493	4,32

other fractures	depth [m]	2b [mm]	PFL [ml/h]
fracture3	-196	0,005	45
fracture4	-278,3	0,011	549

total outflow [ml/h]
1087

Sum of measured outflow [l/min]	Outflow (after PFL measurements)
0,018	0,03

onkpp-137

fractures in the simulation domain	depth [m]	2b [mm]	2b [m]	PFL [ml/h]
fracture2	-233,5	0,004	4,00E-06	17
fracture1 ??	-250	variable	variable	???

outflow [ml/h]	[m3/y]
17	0,15

other fractures [ml/h]	depth [m]	2b [mm]	PFL [ml/h]
fracture3	-186,2		61
fracture4	-207,9		60
fracture5	-275,8		60
fracture6	-277,2		71

total outflow [ml/h]	[m3/y]
269	2,36

Sum of measured outflow [l/min]	Outflow (after PFL measurements)
0,0045	0,06

(Data from appendix of WR 2009-04)